Tracking continental emergence and weathering on the early earth : seawater Hf-Nd isotope constraints from precambrian iron formations

Ian Foster

UNIVERSITE SCIENCES BRETAGNE DE LA MER LOIRE ET DU LITTORAL

Université de Bretagne Occidentale

IMT Atlantique
Bretagne-Pays de la Loire
École Mines-Télécom

THESE DE DOCTORAT DE

L'UNIVERSITE DE BRETAGNE OCCIDENTALE
COMUE UNIVERSITE BRETAGNE LOIRE

ECOLE DOCTORALE N° 598
Sciences de la Mer et du littoral
Spécialité : *Géosciences marines*

Par

Ian FOSTER

Émergence et altération des continents sur la terre primitive : Contraintes à partir des isotopes Hf-Nd dans les formations de fer Précambriennes

Thèse présentée et soutenue à Brest, le 17 Décembre, 2019
Unité de recherche : UMR6538 - Laboratoire Géosciences Océan

Rapporteurs avant soutenance :

VERVOORT	Jeffrey WSU Pullman / Professeur
BAU Michael	Jacobs Université Bremen / Professeur

Composition du Jury :

Président du Jury

HEMOND Christophe	UBO / Professeur

BAYON Germain	IFREMER / Chercheur
VERVOORT Jeffrey	WSU Pullman / Professeur
BAU Michael	Jacobs Université Bremen / Professeur
KONHAUSER Kurt	Université of Alberta / Professeur

Directeur de thèse

LALONDE Stefan	UBO / Chercheur

Invité(s)

AGRANIER Arnaud	UBO / Maître de Conférence
TRIPATI Aradhna	UCLA / Professeur
Le HÉRISSÉ Alain	UBO / Professeur

ABSTRACT

Tracking Continental Emergence and Weathering on the Early Earth: Seawater Hf-Nd Isotope Constraints from Precambrian Iron Formations

Abstract : The emergence of continental crust above sea level in the early Precambrian would have created the first terrestrial habitats, and initiated atmosphere-driven weathering of the continents, yet the history of continental emergence is largely unknown. Precambrian chemical sediments, specifically Banded Iron Formation (BIF) previously studied, appear to have sampled the Hf-Nd isotope composition of ancient seawater, and may preserve a historical record of the emergence of continental landmasses via Lu/Hf fractionation induced by subaerial differential weathering. However, paired Hf-Nd isotope data are available for only a few localities to date, but indicate appreciable emerged continental landmass ca. 2.7 Ga. Our work seeks to confirm and extend this record from the Neoproterozoic into the Paleo- and Eo-Archean using samples of 750 Ma BIF from the Braemar formation in central Australia, 3.2 Ga BIF from the Moodies Group, S. Africa, and 3.8 Ga BIF from Isua, Greenland, as well as several samples from Nuvvuagittuq Quebec, and Nulliak Labrador, Canada. Eoarchean samples appear to have been altered by amphibolite-grade metamorphism, however Moodies Group samples appear primary, having experienced significantly lower metamorphic grades. Moodies appear to retain their primary seawater signatures with !Hf values comparable to those observed in modern oceanic detrital and chemical deposits. Results from the Braemar formation are also interpreted as retaining primary !Hf values signatures and are found to have strikingly similar values to those recently reported for glacial and non-glacial river waters in Greenland.

Together our studies suggest that emerged land masses have been a feature of the Earth since at least the Paleoarchean, despite theoretical models that suggest emergence occurred sometime after 3 Ga ago, and that the interpretation of !Hf and !Nd data from BIF is not as straightforward as previously suggested. A large range of !Hf values can be recorded in BIF that may represent not only a record of ocean water Hf and Lu compositions at the time of deposition, but also BIF can record the presence of detrital contaminants, and/or the existence of post-depositional alteration.

Keywords : Continental Emergence, Hafnium, Lutetium, Isotopes, Banded Iron Formations

RESUME

Émergence et Altération des Continents sur la Terre primitive : Contraintes à partir des isotopes Hf-Nd dans les Formations de Fer Précambriennes

Résumé **:** L'émergence de la croûte continentale au-dessus du niveau de la mer au début du Précambrien aurait créé les premiers habitats terrestres et amorcé l'altération des continents par l'atmosphère. Cependant, l'histoire de l'émergence continentale demeure largement inconnue. Les sédiments chimiques Précambriens, en particulier les Formations de Fer Rubanés (BIF), semblent avoir échantillonné la composition isotopique en Hf-Nd de l'eau de mer ancienne et pourraient ainsi préserver un enregistrement historique de l'émergence de masses continentales par fractionnement Lu/Hf, induit par une altération différentielle subaérienne. Toutefois, les données appariées sur les isotopes Hf-Nd ne sont disponibles que pour quelques localités à ce jour, et indiquent une masse continentale émergée appréciable d'environ 2,7 Ga. Notre travail vise à confirmer et à étendre ce record du Néoprotérozoïque au Paléo- et Eo-Archeén en utilisant des échantillons de BIF âgés de 750 Ma de la formation Bramer en Australie centrale, de 3,2 Ga du Moodies Group, Afrique du Sud, et de 3,8 Ga de Isua, Groenland, ainsi que plusieurs échantillons du Nuvvuagittuq, Québec, et Nulliak, Labrador, Canada. Les échantillons Eoarchéen semblent avoir été significativement affectés par le métamorphisme de type amphibolite, mais les échantillons du Moodies Group conservent des signaux environnementaux primaires, ayant connu des types métamorphiques significativement inférieurs. Les échantillons du Moodies Group montrent que les valeurs d'!Hf sont comparables à celles observées dans les dépôts sédimentaires marins détritiques et chimiques modernes, correspondant à une masse terrestre émergée à cette époque. Les résultats de la formation de Braemar sont également interprétés comme conservant les signatures primaires d'!Hf, et ont des valeurs remarquablement similaires à celles récemment rapportées pour les eaux fluviales glaciaires et non glaciaires au Groenland, témoignant d'une altération subaérienne concomitante avec les dépôts Sturtian de BIF durant les premiers stades de la déglaciation. Ensemble, mes résultats suggèrent que les masses émergées ont été une caractéristique de la Terre depuis au moins le Paléoarchéen, malgré les modèles théoriques qui suggèrent que l'émergence s'est produite quelque temps après 3 Ga, et que l'interprétation des données !Hf et !Nd des BIF n'est pas aussi simple que suggérée précédemment. Une large gamme de valeurs d'!Hf peut être enregistrée dans les BIF, qui peut représenter non seulement un enregistrement des compositions de Hf et Lu de l'eau de mer au moment du dépôt, mais peut aussi enregistrer laprésence de contaminants détritiques et/ou l'historique des altérations post-dépôt.

Mots clés : Émergence continentale, Hafnium, Lutétium, isotopes, formations de fer en bandes

Table of Contents

List of Figures

Chapter 1
Introduction

Chapter 2
Materials and Methods

Chapter 3
Hafnium isotope evidence for emergence of the continents prior to 3.22 billion years ago

Chapter 4

Lutetium-Hafnium evidence for non-glacial weathering during the Sturtian Glaciation: Neoproterozoic BIF records riverine input during periods of a Slushball-Earth

Chapter 5

Results from the Isua, Nuvvuagittuq and Nulliak Iron Formations

List of Tables

Acknowledgements

It is said that the greatest challenges in life are those we set for ourselves. They often require commitment, sacrifice, and are difficult to achieve under even the most favorable circumstances, for if they weren't they wouldn't be worth doing, their value is not just measured by a grade, by a page count, or by prestige and publication number, they are primarily a statement about who we are, what we aspire to be, and what we can do. While the work contained within this thesis does address some of those measures of success, it is, for me, primarily the physical representation of an ambition, a goal, a challenge and a dream I set out for myself long ago, and like all achievements in life it stands as a testament not only to the commitment to overcome the challenges such a project inevitably presents, but also as a testament to the patience, encouragement and constant support of family, friends and coworkers over the past 5 years, without which, the completion of this thesis would not have been possible.

First, and foremost, my heartfelt thanks and everlasting gratitude go out to my parents Anna-May and Craig. Your love, support and encouragement were every bit as vital to the completion of this work as any chemical in the lab, and the sacrifices you have made over the years for me and my siblings are truly inspirational. You have always been there for me when I needed it, not only during my post-secondary work, but throughout my life. I owe you a debt that I will never fully be able to repay, you are an inspiration to me, if I am ever a parent I can only hope to be as successful as you have been, and it is to you both that I dedicate this work.

Second, to my advisors Aradhna and Stefan, I extend my deepest thanks and gratitude to you both. Your brilliance, patience, support and understanding have been essential to the completion of this work, but perhaps more importantly, your willingness to give me the opportunity to work with you on this project, and to support me through the successes and setbacks sets you both apart as people who are not just inwardly focused on themselves, but as those rare people who can see the best in others and are willing to provide the help and opportunity for people to prove it to themselves. I will always be grateful for all that you have done for me and know that world is a better place for having people like you in it.

To Arnaud, Philippe, Sidonie, and the rest of the IUEM and LabexMER staff. I would like to thank you all for your guidance, understanding, patience and willingness to help me

over the years. Arnaud, thank you for ‘showing me the ropes’ of Hf column chemistry, your instruction in the lab and your assistance in preparing and running samples on the mass-spectrometer, as well as your aid in processing the data and interpreting it was essential to this project. Philippe and Sidonie, as the people who I most often encountered in the lab, all my little questions and daily problems often seemed to fall to you for an answer. Thank you both for your patience and help while I learned my way around. And to all the other Staff and Technicians, I thank you all, you were each instrumental to the completion of this work whether it was analyzing samples or sorting out the necessary paperwork for my enrollment. Your skill, patience and willingness to help was always greatly appreciated, and is the foundation for which all of us are enabled to succeed.

To Vicki, Whitney, Katie and Martin, I extent my deepest gratitude and thanks to you all, I can’t imagine my time spent in France without you, and I am forever grateful that we had the opportunity to meet and explore a new country together, no matter how briefly. You have all made a deep impression on me, and I couldn’t have completed this work without the fun and support you all provided over the years. I wish you all the best and I miss you already.

Finally, to my family and friends. After so many years travelling, to so many different places, there are now far too many of you that deserve my thanks then can be written out individually. In one way or another you have all helped to shape and support me, not just during my Ph.D., but long before, and I hope for a long time after. Many of you were fundamental to the completion of this work and as always you provided me with much needed distraction when times were stressful, support when times were tough, provided laughter when times seemed dark, and were there to share and celebrate in the good times even from afar. Though some of us have grown closer or further apart over the years, I am who I am because of you all, and I thank you all now for your support and friendship and sincerely hope that we may we continue to share in each other’s trials and triumphs for many years to come.

With that, I will conclude these acknowledgements with a quote by Douglas Adams that I feel accurately summarizes my entire Ph.D. experience nicely.

I may not have gone where I intended to go,
but I think I have ended up where I intended to be.
– Douglas Adams –

Chapter 1: Introduction

1.0 Introduction

The development of continental landmasses above sea level would have created the first environments for terrestrial organisms to inhabit, and the initiation of continental weathering would have dramatically changed the chemistry of seawater and the atmosphere. Yet the history of continental emergence and its impacts are largely unknown. Numerical modeling suggests continental crust may have been effectively flooded prior to 3.5 Ga (Flament et al. 2013), and only emerged gradually to areas approximately 5-8% of the modern landmass by 2.5-2.0 Ga but this, to date, has not been thoroughly tested using geological data. To address the timing of continental emergence on the early Earth, our study builds on the approach proposed by Viehmann et al. (2014; 2015; 2018) and examines the isotopic composition of Neodymium (Nd) and Hafnium (Hf) in Precambrian Banded Iron Formations (BIF's) as a geochemical proxy for the presence and importance of subaerial weathering. In principle, paired measurements of Hf and Nd isotope values (Hf-Nd) may help constrain the timing of the transition from a "water-world" with only submarine crust, as thought to characterize the earliest history of the Earth, to a planet with conditions more like the present, with continents standing above sea level.

1.0.1 Lutetium-Hafnium and Samarium-Neodymium Systematics

Nd and Hf are two high field strength elements with multiple stable isotopes amenable to isotope ratio measurement (^{143}Nd, ^{144}Nd, and ^{176}Hf, ^{177}Hf, respectively). These isotope systems also host several powerful geochronometers that can be used for very precise dating of rocks that are several hundred million to several billion years old. The most widely applied of these geochronometers come from the decay of Lutetium (Lu),

Periodic Table of Elements

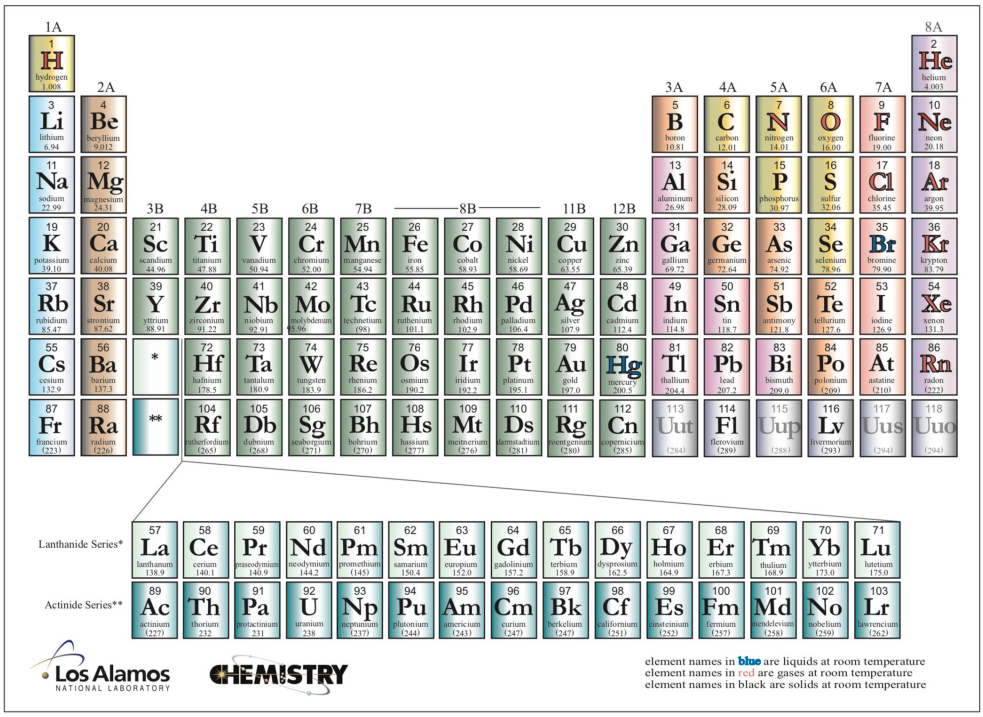

Modified from Los Alamos National Laboratory Chemistry Division; available at http://periodic.lanl.gov/images/periodictable.pdf.

Figure 1.1: The periodic table of elements, the rare earth elements prominently displayed at the bottom, note Nd is element number 60, Sm element 62, Lu element 71, and back in the main chart Hf is element 72.

---

specifically ^{176}Lu to the daughter product ^{176}Hf, which has a half-life of 37.8 Ga, and from the decay of Samarium (Sm), specifically ^{147}Sm to ^{143}Nd, which has a half-life of 106 Ga.

Crucially, the Sm-Nd and Lu-Hf (Figure 1.1) isotope systems are coupled in the mantle and in other magmatic environments. During the magma cooling process each of these elements (Hf, Nd, Sm, Lu) has preferred minerals it will partition into, and it is the geochemical behavior of these minerals that makes the **ε**Hf-**ε**Nd system useful for investigating non-mantle and magmatic environments. Due to their larger atomic size

(closer to that of the typical lithophile elements, for example Ca, Na, K, Mg) Nd and Sm both substitute easily into mica, and other minerals of the phyllosilicate family, as well as phosphates. Functionally this means Nd and Sm tend to end up in the same mineral phases, thus when weathering occurs, they are released congruently into the environment. Crucially the same cannot be said for Lu and Hf. During magmatic crystallization Lu is taken up into mineral phases such as apatite, garnet, and fluorides, all minerals that weather easily at the Earth's surface, but do not include any initial Hf. Due to its small ionic radii, and very high electrostatic field strength, specifically Hf^{+4}, Hf behaves in a very refractory manner and does not substitute for major elements, but instead forms accessory phases with other similar elements, ultimately leading to its predominance in felsic crustal compositions, in fact, Hf and Zirconium (Zr) are so close in size in charge virtually all Hf ends up in the highly weathering resistant mineral Zircon ($ZrSiO_4$). The ratio of Zr to Hf in Zircons is typically 33.6:1 (similar to the crustal abundance of each element), however the ratio can be higher, and in rare cases do to the solid solution behavior of these elements can form a 50:50 ratio mineral known as Hafnon ($(Hf,Zr)SiO_4$), and under rare conditions where magmas are especially rich in sodium and potassium both Zr and Hf can be found in the rare mineral Eudialyte ($Na_{15}Ca_6Fe_3Zr_3Si_{26}O_{73}(OH)_4Cl_2$) (Taylor and McLennan, 1995; Jones III, J.V. et al. 2006).

The difference in the geochemical behavior of these elements, i.e., the separation of Lu, Sm and Nd into easily weathered rocks, while Hf is sequestered into extremely weathering resistant phases, thus allows us an opportunity to track the source and intensity

of subaerial weathering in modern environments and may allow us to trace the emergence of the continents in the Earth's past, as will be discussed below.

1.0.2 Early Crustal Differentiation

Our world is ancient, far older than many of the most respected scientists in the first half of the 20th century were initially willing to believe; that finally changed when the discovery of meteorites, specifically a class of meteorites called chondrites, that had the same overall chemical composition as the Earth were first dated. The results were stunning, not only was our planet old, it was old on a cosmic scale, and if these fragments of rock fallen to earth, discovered and salvaged by scientists were to be believed, then our planet was in fact approximately 4.45 billion years old (Patterson, 1956). This remarkable discovery changed the entire concept of how we thought our planet came to be, from that of guided creation, to one of extremely gradual and complicated chemical, physical and biological change.

It is generally agreed upon that the physical state of our planet following its amalgamation, and the moon-forming event that followed was one of physical and chemical extremes. Globally, a magma ocean must have existed at the Earth's surface, and it was only after some, still unknown, millions of years that the surface environment began to cool enough for solid crust to form, and eventually for the atmosphere to cool sufficiently that water vapor could condense to form the first primordial oceans (Figure 1.2).

Figure 1.2: Possible views of the early Earth as a global magma ocean immediately after its formation (left panel), to a water world as surface temperatures dropped below the condensation point of water, and water vapor condensed out of the atmosphere to cover the primitive surface (right panel).

Due to the unique (so far as we know of) processes that occur at our planet's surface, specifically the subduction of surficial material and the eruption and formation of new landmasses, much of the geologic history of our planets formative years has been lost, leading to a wealth of speculation based almost entirely on geochemical signals, ancient greenstone belts and the chemical properties of a particularly resistant mineral known as Zircon.

There are, to date, no known large igneous, metamorphic or sedimentary rock units that can be dated to be older than 3.8 billion years old and only fragments that can be dated to 4.03 Ga (Tang et al. 2019). There are however within these oldest rocks the sedimentary remnants of even old rocks, specifically zircons. As will become evident, zircons have

played both an important role in the magmatic and crustal developmental history of our planet, as well as the latter sedimentary and subaerial evolution of our world as well.

Most of what we know of the early Earth's surface is from individual fragmentary pieces of the Earth's crust, the most resilient felsic minerals, zircons. The general agreement is that that Earth had formed by 4.55 Ga ago, and the moon forming event had taken place by that time as well, either way, it is assumed a magma ocean was present on the earth's surface at this time, and the oldest zircons known to date provide dates of 4.38 Ga ago, indicating that the vast majority of accretionary activity, including the moon forming event must have concluded by this time (Harrison et al. 2009).

The transition from a magma ocean to what we would consider a modern continent involves a problematic series of geochemical and geophysical transitions, all of which have been overprinted by a minimum of 4 supercontinent amalgamation events that occurred at 2.7, 1.9, 1.2 and < 0.4 Ga. The formation of a supercontinent represents a major geological event were crust is formed and preserved, despite the fact that ancient mantle temperatures would have been higher, and subduction rates greater in the past (Harrison et al. 2009).

There is a great diversity of opinion as to when, and how much, continental crust was produced, and at what point in Earth's history. Multiple theories have been produced based on a variety of geochemical proxies that suggest crustal production of 70% continental crust by 3.1 Ga, while alternate research groups suggest that less then 20% of continental crust had been extracted by 3.2 Ga (Harrison et al. 2009). In fact, records of

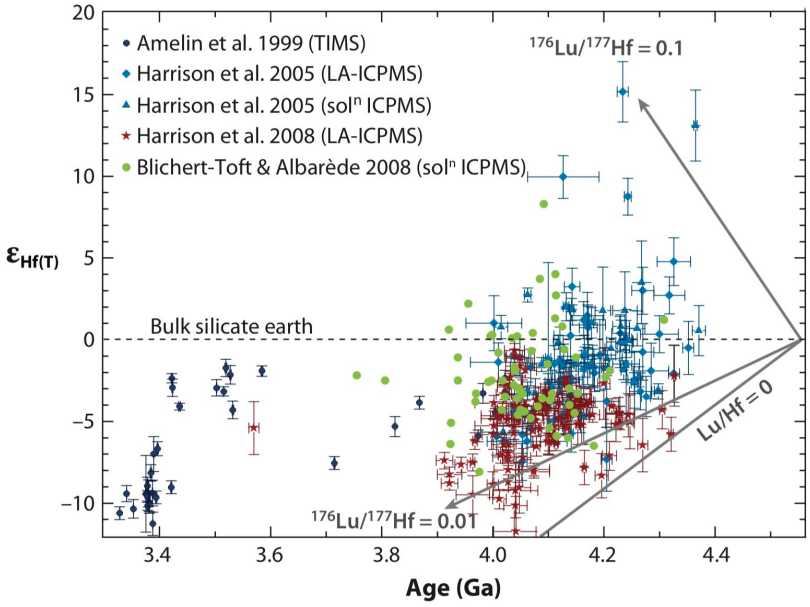

Figure 1.3: Plot of **ε**$Hf_{(T)}$ verses Age for more than 300 Lu-Hf measurements on zircons with $^{207}Pb/^{206}Pb$ ages up to 4.36 Ga. Data from Blichert-Toft & Albarède (2008) (*green circles)* are bulk $^{207}Pb/^{206}Pb$ ages corrected from common pb, assuming Th/U=1 and concordancy between the U/Pb and Th/Pb systems with **ε**Hf corrected to 4.1 Ga. Grey lines emerging at 4.56 are trajectories show in Hf isotope evolution for $^{176}Lu/^{177}Hf$ values of 0, 0.01 and 0.1. *Figure and caption from Harrison (2009).*

---

crustal evolution from the Jack Hills, region of Australia, contain numerous zircons that represent some of the oldest evidence for crust, and also confirm some of the most ancient water-rock interactions known on to date (Harrison et al. 2009, Bell et al. 2011). This evidence suggests that felsic crust formation begun to form almost immediately after the Earth's formation, aka, 4.55 Ga ago based on positive (as high at +**ε**Hf 15) values in detrital zircons, which suggests that that a significant portion of mantle had been depleted in Lu-rich minerals almost immediately after the Earth's formation (Figure 1.3)**.**

The initiation of plate tectonics, and the development of the modern super continental cycle, are extremely hard to constrain, as one needs to know both the rates of crust generation and the rates of destruction, as well as the cooling rate of the mantle. Given that that the erosional lifetime of ophiolites (abducted pieces of ocean crust propped up and preserved on top of felsic continental crust) is usually only ~ 500 Ma, then much of the early abducted oceanic crust would have been lost in the first billion year of Earth's history (Harrison, 2009). The existence of Hadean Zircons greater than an age of 4.3 Ga however, suggests that crustal differentiation and evolution (mafic vs. felsic) began soon after the Earth's formation, though the arguments for and against the speed, degree and extent of crustal differentiation, would become a greatly debated topic in the following years.

Additionally, the remaining crustal record of zircons cannot be entirely trusted as a direct and accurate record of continental growth. In fact, Zircons are sufficiently resilient that that can resist total re-melting during magmatic recycling and are prone to adding new growth rings during magmatic events complicating their history, but simultaneously preserving a record of their magmatic history. Presuming the initial core of a zircon survives, only that portion records its ignition formation age and $\boldsymbol{\varepsilon}$Hf, and any outer rings thus represent subsequent reprocessing events. For this reason, zircons must be studied carefully as they often represent an entire growth history, rather than their particular formational magmatic event.

Belousova et al (2010), took the cumulative results of multiple zircons (16445 in total) dating from the Archean to modern in an attempt to determine if there was a

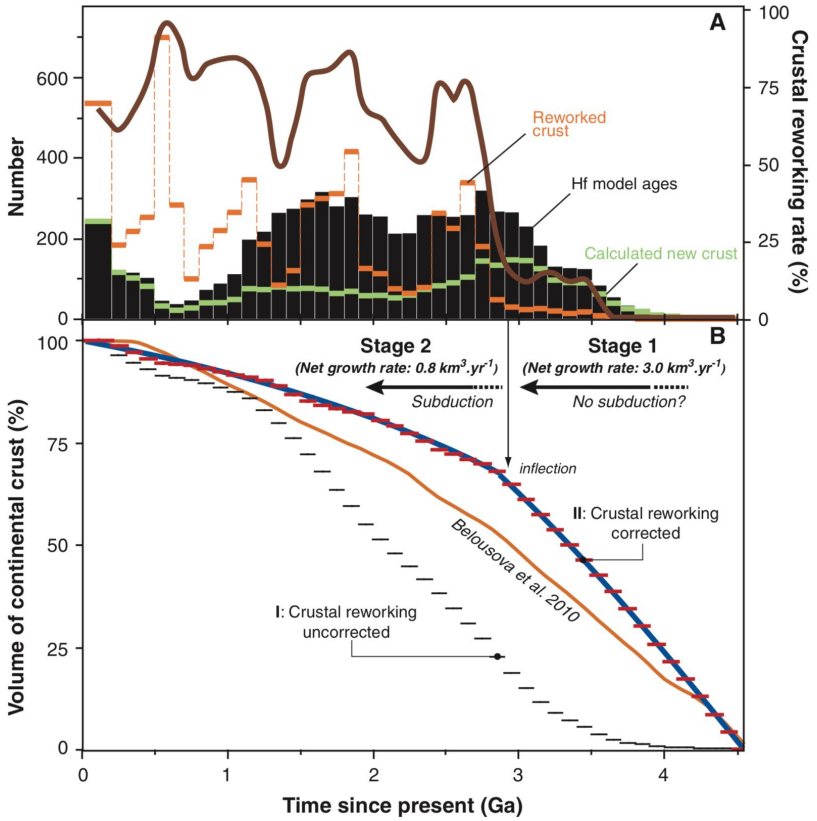

Figure 1.4: (A) Distribution of the Hf model ages, calculated new crust ages, and reworked crust ages through time, from a worldwide database of 6972 U-Pb and Hf analyses of zircons from young sediments, with deposition ages ranging from the late Paleozoic to the present day. All calculations are presented for every 100-million-year time interval starting from 200 million years ago (Ma). The youngest bin is for 200 Ma because of uncertainty over the range of deposition ages of the sediments. The brown curve represents the variation in the rates of reworking of the continental crust through time, calculated from the distributions of the proportions of reworked crust (orange histogram) and new crust (green histogram). (B) Continental growth curves calculated from the same database as (A). The cumulative volume of crust is calculated for 100-million-year time intervals. Curve I (black) is calculated from the cumulative proportions of the Hf model ages through time [black histogram in (A)]. Curve II (red) integrates the variations of the reworking rates [brown curve in (A)] in the calculations of the cumulative proportions of the newly formed crust through time. The blue curve highlights the main variations observed in curve II. The overall shape of this curve is not substantially affected by the selection of the Lu/Hf ratios in the crust and the Hf isotope ratios of new continental crust in the calculation of individual model ages. The curve obtained by Belousova et al. (4) from a U-Pb-Hf database of 13,844 zircons of various ages and origin is reported for comparison. *Figure and caption from Dhuime et al. (2012).*

overarching pattern that could be determined from the results. These authors also provided 5 different criteria for which to remove a zircon from their analysis if it did not meet analytical standards, and ultimately 2601 zircons were removed from the study based on these criteria, and the remaining 13844 were used for further modeling (Belousova et al. 2010). Multiple model calculations made by these authors matched well with the GLAM (Global Lithospheric Architecture Mapping) model proposed by Begg et al. (2009) without model forcing. Essentially, these two methods agreed that at least 70% of the sub-continental lithospheric mantle had formed in the Archean, with an average age of 2.8 Ga, though this may be an underestimate due to the bias towards preserving younger zircons and the subduction of older ones back into the mantle (Belousova et al. 2010).

Dhuime et al. (2012), later reinvestigated the ages and frequency of ancient zircon formation and found that the frequency of zircon ages didn't exactly match the presumed crustal growth reworking rate, nor the presumed crustal creation rate a previously proposed (GLAM or Belousova et al. 2010). This lead the authors to propose a refined model (Figure 1.4) that included crustal reworking rates, and suggest that from ~4.0 Ga to 3.0 Ga there was a relatively high rate of continental, i.e. felsic crustal formation (~3 km^2) with little crustal reworking, then an apparent inflection point at approximately 3.0 Ga, where crustal reworking increased sharply and preservation tapered off to the modern day rate of felsic crust formation of ~0.8 km^2) by 3.0 Ga, most likely due to the way felsic crust was generated and onset of modern day subduction at that time (Dhuime et al. 2012).

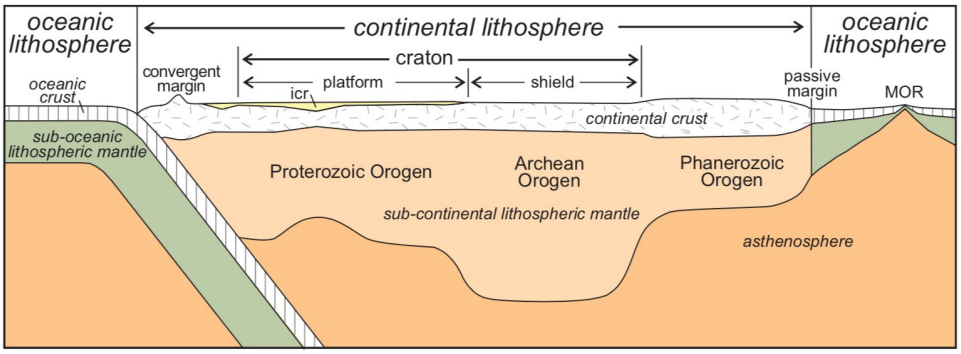

Figure 1.5: Schematic cross section of types of continental lithosphere emphasizing the thick stable nature of Precambrian cratons. Thickness of lithosphere bbeneath Archean regions is on the order of 200-250 km and oceanic lithosphere is up to 100 km. Abbreviation: irc = intragratonic rift; MOR = mid-ocean ridge. *Figure and caption from Cawood et al. 2013.*

As depicted by Cawood (Figure 1.5) the structure of the modern crust can largely be broken down into two distinct types, thick continental crust and underlying lithosphere, and comparatively thinner and more dense oceanic crust and underlying lithosphere that is eventually subducted back into the mantle. In the idealized version of continental growth we observe today subduction of the ocean crust under continental crust can both scrape off submarine sediments as well as any extant islands onto the sides of a continental craton (this is known as an active margin). Here dehydration of old oceanic crust produces magmatism on the continent above, welding the growing continent together (the South American Andes Mountains have formed in this manner). Alternately new crust can be generated by the collision of continents, and the uplift of any oceanic or continental crust between them to form mountain belts (the Himalayas of the Alps are examples, ultimately the generation of continental crust requires the collision, remelting of denser mafic crust to form less dense felsic crust that is not subducted back into the mantle (Cawood et al. 2013).

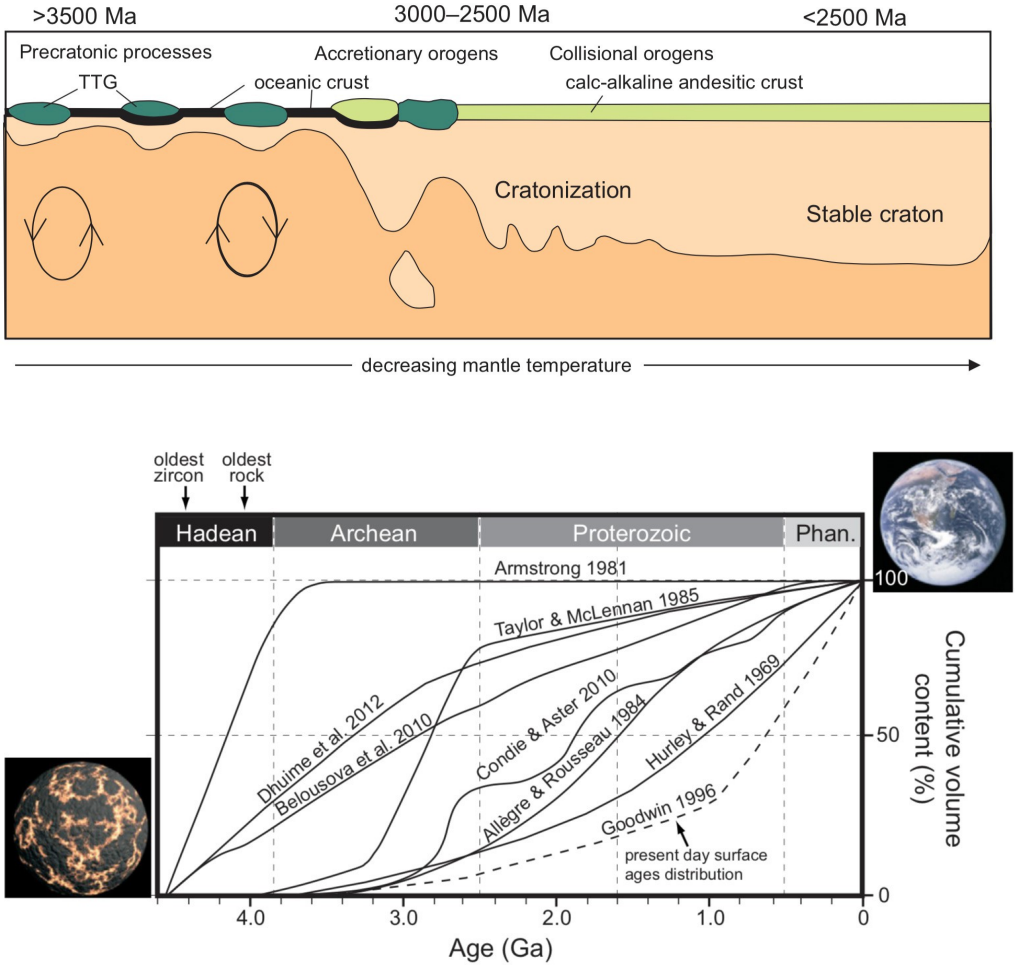

Figure 1.6: (Top panel) Temporal evolution of the lithosphere associated with the thermal evolution of the mantle from early Earth (adapted from S. Foley, 2012, personal commun.) involving a bimodal association of TTG (tonalites, trondhjemites, and granodiorites) and greenstone evolving through development of accretionary and collisional orogenic processes into a regime producing continental crust of andesitic composition by at least 3.0 Ga. (Bottom panel) Crustal growth models of Hurley and Rand (1969), Armstrong (1981), Allère and Rousseau (1984), Taylor and McLennan (1985), Condie and Aster (2010), and Dhuime et al. (2012) compared to age distributions of presently preserved crust Goodwin (1996). *Figure and caption from Cawood et al. 2013.*

Exactly when, and how this process began remains enigmatic due to a lack of remnants of continental crust older then 3.8 Ga, presumably because they were subducted back into the mantle, or are as yet to be discovered. Despite the difficulties in determining the rates of continental growth over time, many authors have numerous authors have attempted to use the data we have on hand as discussed above, and there is a growing consensus that the generation of continental crust began early in Earth history and has slowed over time to modern rates (Figure 1.6).

1.0.3 Formation of Continental crust vs. Crustal Emergence

Despite the above discussion concerning the generation of continental-type crust during the Hadean and Archean eons, a crucial component of these studies has not been addressed, specifically whether or not any of the crust, continental, oceanic or otherwise was emerged, that is to say, exposed above water during this period. Few studies to date have addressed this matter due to the limited extent of geologic terrain to examine that dates back to the Paleoarchean (and none that is known from the Hadean >4.0 Ga), despite the fundamental importance of this question, as exposed continents especially with a felsic composition, would provide both unique nutrients and habitats for early life.

The problem is complicated further by the fact that emergence of continental crust is not related to any one factor, but rather a combinations of factors, specifically (i) loss of radiogenic elements from the mantle to continental crust, reducing mantle heat production; (ii) that oceans are more efficient then continents at evacuating heat from the mantle, thus as continents grow less heat is lost over time, and (iii) the timing or extent of crustal

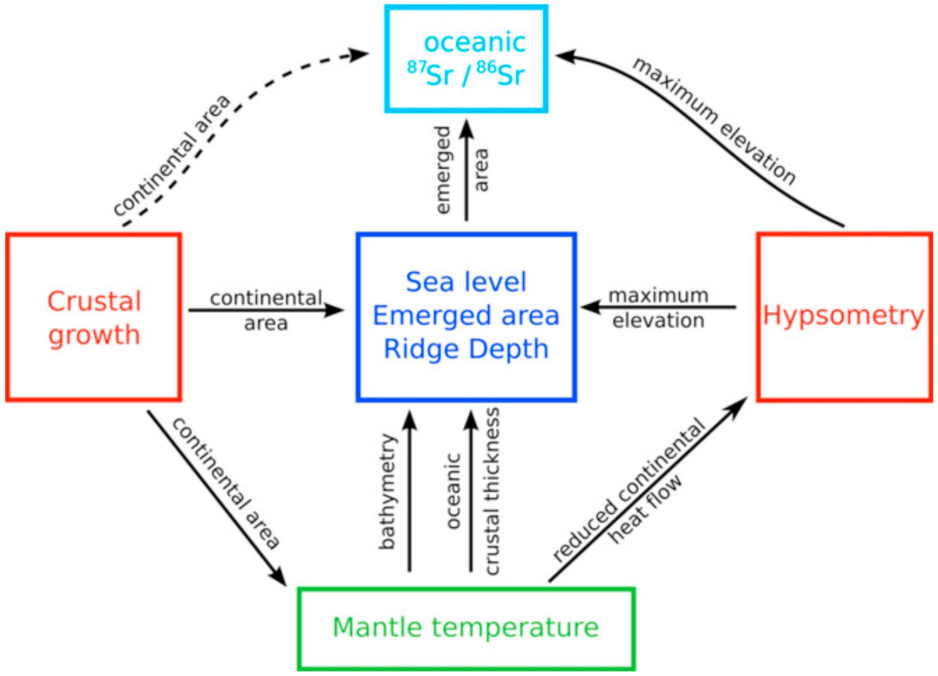

Figure 1.7: Flow chart of the model used in this study. Arrows indicate model inputs and boxes indicate the variables and parameters of the model. The temperature of the mantle is calculated as in Labrosse and Jaupart (2007), the continental hypsometry is calculated from the results of Rey and Coltice (2008) and sea level, ridge depth and emerged land area are calculated as in Flament et al. (2008). *Figure and caption from Flament et al. 2013*

---

recycling into the mantle is unknown making it hard to predict the effects of cold crust reentering and cooling the mantle. (Flament et al. 2013). Ultimately what these factors all center around is the ideal that a hotter early mantle would have been unable to support the increase in mass generated by the addition of new and thickening continental crust, and that this thicker crust would then sag downwards until it is in equilibrium with the mantle below in a balance known as hypsometry (Figure 1.7).

Model results by Flament et al. (2013) considered 4 different scenarios (with the caveats that it assumes a constant ocean volume and constant crustal thickness), (i) a constant continental growth scenario (CGM); (ii) a model where most growth occurred in the Neoarchean (NGM); (iii) an early continental growth model (EGM) and (iv) a continental recycling model where crustal recycling dominated (RM). Given the model inputs and constrains 4 different scenarios can occur (i) the continents are partially flooded; (ii) the continents are entirely flooded; (iii) the continents are entirely emerged or (iv) the mid-ocean rides emerge. Situations (ii), (iii), (iv), are the limits of model, thus calculations stop if any of them occur, which is why some models do not progress in time all the way back to 4.5 Ga, but are rather extrapolated back passed the model data based on the model trend. Despite these caveats the overall conclusions of each model type resulted in a strikingly similar outcome, that prior to 3.0 Ga less then 4% of the worlds currently emerged landmasses were predicted to be emerged above water (Figure 1.8). This is because the area of emerged land depends on mantle temperature, the amount of continental crust produced at the time, and hypsometry, and would imply that that Earth was a waterword, for nearly half of its history and a complete waterworld prior to 3.5 Ga (Flament et al. 2013).

Despite these conclusions, sedimentological evidence such as alluvial sandstones and conglomerates are known from periods prior to 3.0 Ga (e.g., Homann et al., 2018). Although these basic observations confirm that emerged continental crust existed in the Archean, much work still needs to be done. As explained below this study seeks to greatly expand our knowledge of continental emergence throughout the Archean and Proterozoic.

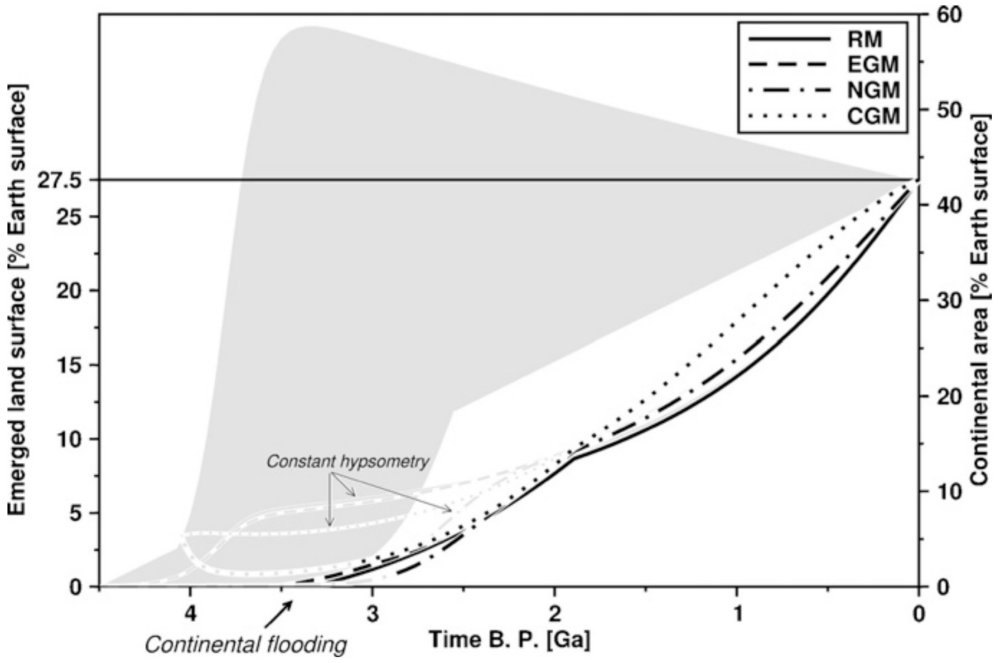

Figure 1.8: Shows the percentage of emerged land does not differ significantly depend on the continental growth model used (black lines), not the amount of crust generated (grey shaded area). The models all converge on less then 4% of Archean continental land mass being emerged prior to 3.0 Ga, and complete continental flooding prior to 3.5 Ga. *Figure from Flament et al. 2013.*

1.0.4 Hf-Nd Isotopes in Seawater

The concentration and distribution of Rare Earth Elements (REE) in seawater provides a wealth of information on both biological and geochemical processes occurring in both the terrestrial and marine realms. Despite the impact of such knowledge, actual values, concentrations and importance of local inputs have for Hf only recently been resolved due to technological advances in analyzing aqueous trace element geochemistry.

While the dissolved component of Nd has been investigated since the start of the 1980's (Piepgras and Wasserburg, 1980), initial results clearly showed that Nd values were not globally uniform, that global seawater concentrations were in the pg/g range, and that local differences in Nd values may reflect the input of Nd from nearby terrestrial Nd sources, a result later confirmed by Van der Flierdt, et al. (2004). The residence time of Nd in the oceans is relatively low, on the order of the global ocean turnover time of 1500 yrs, which does not provide adequate time for global Nd equilibrium. Thus, Neodymium is now considered to be an element that can be used as a tracer for source regions of Nd, but not an indicator of global Nd values.

Due to the aforementioned technical limitations with directly measuring Hf in seawater, the first evidence for there being dissolved Hf in seawater came from early studies of manganese nodules, crusts, and ferromanganese crusts (all of which are a type of chemical sediment that typically form in deep ocean settings). Early results found **ε**Hf values that were positive in these nodules, in comparison to related sediments, and the authors surmised that a major component of the influx of Hf into the ocean is likely mantle-based hydrothermal systems, alteration of oceanic crust, or erosion of young mafic volcanoes, with input from terrestrial sources thought to be minor due to the weathering-resistant nature of zircons (White et al. 1986). Additional studies with a much wider data set of ferromanganese nodules and crusts was undertaken in the late 1990's; Godfrey et al. (1997) found systematic differences between crusts in different ocean basins, and that the speed at which a nodule grew could be correlated positively with its **ε**Hf value. This study was followed closely by a pivotal study by Albarède et al. (1998) that analyzed additional

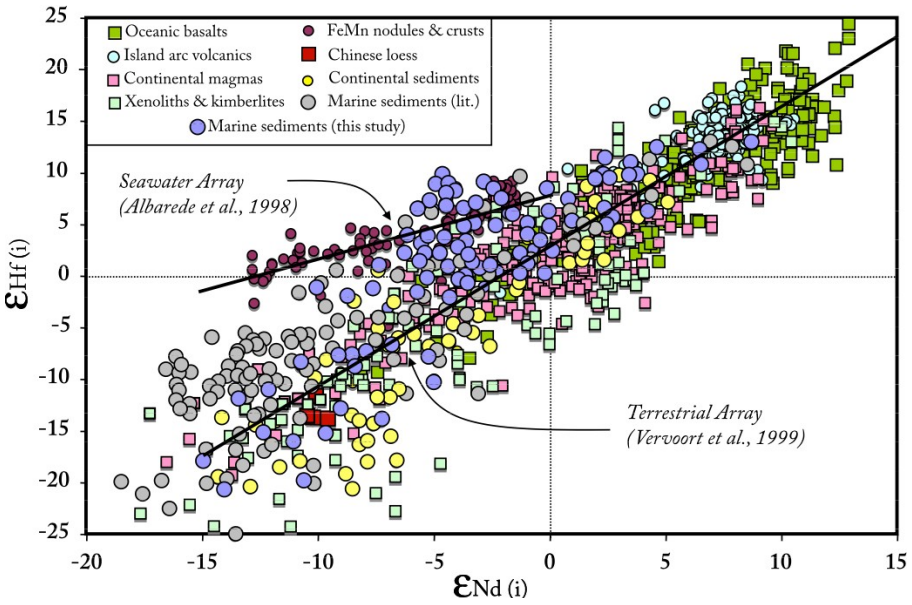

Figure 1.9: Initial ε_{Nd} vs. ε_{Hf} for representative crust and mantle compositions. To a first order, all compositions form a strong positive correlation called the Terrestrial Array. The most obvious deviations from this are Fe-Mn crusts/nodules, which define a seawater array. Reference Terrestrial Array ($\varepsilon_{Hf} = 1.36 \times \varepsilon_{Nd} + 2.95$) and seawater array ($\varepsilon_{Hf} = 0.55 \times \varepsilon_{Nd} + 7.1$) after Vervoort et al. (1999) and Albarède et al. (1998), respectively. *Figure and caption from Vervoort et al. 2011.*

---

samples and compared their **ε**Hf value to their **ε**Nd value and convincingly demonstrated that the **ε**Hf value for ferromanganese nodules was systematically more positive than its **ε**Nd value, and that the **ε**Hf and **ε**Nd isotopic systems were decoupled in these samples and formed a correlated trend they called the "seawater array". Vervoort et al. (1999) then examined hundreds of oceanic sediments, as well as samples of oceanic and continental crust, and found that there was a notable correlation between their isotopic compositions, and that their **ε**Hf and **ε**Nd values varied in the same manner, with more negative values

of **ε**Hf correlated with more negative values of **ε**Nd, and specifically that the Hf-Nd systems were coupled in the crust and mantle. These authors described this trend as the "terrestrial array". This coupling effect was best expressed in passive margin settings were the zircon effect and sedimentary sorting was strongest but was notably muted on active margins where degrees of sorting and weathering timescales were less important (Vervoort et al. 1999).

At this time both analytical and sampling difficulties still prevented the direct measurement of Hf in seawater, however the collection of data continued (Vervoort et al., 2011, and Figure 1.9). It began to emerge that a significant spread off of the original "seawater and terrestrial arrays" existed. Additional factors for the decoupling observed in seawater were proposed to include the incorporation of very fine dust, specifically clay sized particles, falling directly into the ocean, as weathering and retention of Hf in zircons alone could not explain the trends observed (Pettke et al. 2002, Chen et al. 2011, Chen et al. 2013). In addition to source/sink balance problems, Bau et al. (2006) also demonstrated that the way Hf and Nd bonded to ferromanganese nodules and crusts differed fundamentally. While Nd could adsorb and desorb from the crust surface, thus keeping it in equilibrium with surrounding waters as the crust grew, Hf (occurring almost exclusively as the pentahydroxide $Hf(OH)_5^-$) was tightly bound and did not continue to exchange with surrounding waters. Thus, the **ε**Hf measured in each sample was the cumulative and average value of all Hf the sample adsorbed, and the measured value would necessarily be affected by its growth rate and local inputs (Bau and Koschinsky, 2006), confirming observations previously made by other authors. This effect is again amplified by the

location of the ferromanganese crusts with regard to their proximity to continental inputs (aeolian dust or rivers), due to the low residence time of Hf in seawater, estimated to be between 600 and 1500 years (Godfrey et al. 2009), but is likely closer to that of Nd (1500 yrs.), makes the **ε**Hf value recorded susceptible to local inputs, as it is not completely homogenized in the ocean before deposition (Van de Flierdt et al. 2007).

It has only been in the last decade that sampling and analytical techniques have sufficiently advanced that the Hf concentration and compositions of seawater could be measured directly. This was first achieved for deep (~4000 m depth) waters in the Atlantic, where Rickli et al. (2009) were able to measure Hf concentrations that were generally less than a pmol/kg and ranged from slightly negative to slightly positive in their **ε**Hf isotope composition. A complimentary study was carried out on Atlantic seawaters by Godfrey et al. (2009) on Northeast Atlantic seawater, who found that Hf concentrations and compositions not only varied with location but also with depth, where increasing depth was found to correlate with both increasing concentrations of Hf as well as an increase in the **ε**Hf values, ranging from -5.71 to +3.3 at 50 m depth to a maximum of 1.86 at 946 m and 1.37 at 5500 meters, suggesting that Hf is more uniform and better mixed at depth. Similarly, Zimmermann et al. (2009) sampled multiple sites and depths in the Pacific Ocean but found that while some variation existed, all samples analyzed produced positive **ε**Hf compositions at all sites sampled, and that they did not systematically very with depth, with some samples being more positive then, or less positive then, the surface composition at that site.

As discussed previously, to a great degree the "seawater array" is defined by the **ε**Hf compositions of ferromanganese nodules and manganese crusts, both of which are direct chemical precipitates from modern ocean water. At various periods in Earth's past similar chemical sediments were deposited in global ocean basins, namely banded iron formations (BIFs), a term given to iron rich (typically 15-40% iron, and 40-60% silica) sediments, deposited predominantly in the NeoArchean and Proterozoic (~2800 to 600 Ma), but are also known from as far back as 3800 Ma ago. The use of banded iron formations has been suggested for decades as a repository that may record the chemical compositions of ancient seawater (Derry and Jacobbsen, 1990); the appropriate assessment of which can be tested as discussed later. Ultimately, the fidelity of this suggestions has been born-out, and it is now acknowledged that banded iron formations do indeed record seawater composition, and can also shed light onto important environmental changes that occurred in the Earth's oceans and atmospheres over some of the most important geological periods in our planets history (Konhauser et al. 2017).

1.0.5 Modern Weathering and Hf-Nd and Riverine Values

As discussed above, the ability to isotopically analyze the Hf input from terrestrial, riverine sources into the global oceans has only recently been made possible by the ability to consistently separate and analyze this element with a new generation of geochemical techniques and sensitive plasma-based mass spectrometers. Though much work remains to decipher the local, regional and global inputs of Hf into the oceans the following is a summary of the major findings to date. In a 2006 publication in the journal Geology, Bayon

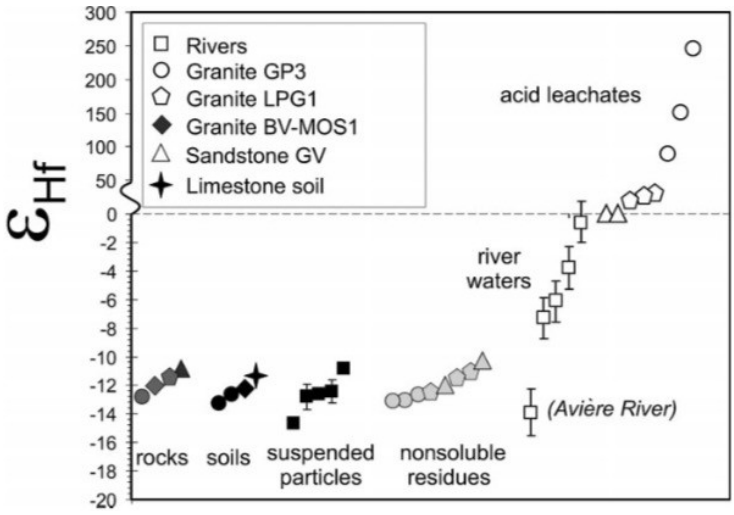

Figure 1.10: Hf isotope compositions for Moselle basin rivers (dissolved loads and suspended particles), bedrocks, soils, and acid leachates and non-soluble residues. Errors reported for river waters are 2 σ (external re- producibility; 1.56 **ε** units). Errors for rocks, soils, suspended particles, non-soluble residues, and acid leachates are within the size of symbols. Open symbols refer to rivers (square) and acid leachates (triangle, pentagon, circle); dark gray-colored symbols refer to whole rocks (circle, diamond, pentagon, triangle); light gray-colored symbols refer to non-soluble residues; black symbols refer to river suspended particles (square) and soils (circle, diamond, star). *Figure and caption from Bayon et al. 2006.*

---

et al. were conclusively able to demonstrate that acid weathering of granites produced distinctly different **ε**Hf values depending on the type of mineral exposed, to acid weathering, the concentration of the acid, and the duration of exposure to leaching experiments. Their results were extremely informative into which rock types, and minerals were responsible for producing specific **ε**Hf values. Ultimately, these authors found that the majority of sediments had relatively low **ε**Hf values (~-15 to -10), river waters contained significantly more radiogenic **ε**Hf values (~-15 to 0), and acid leachates of

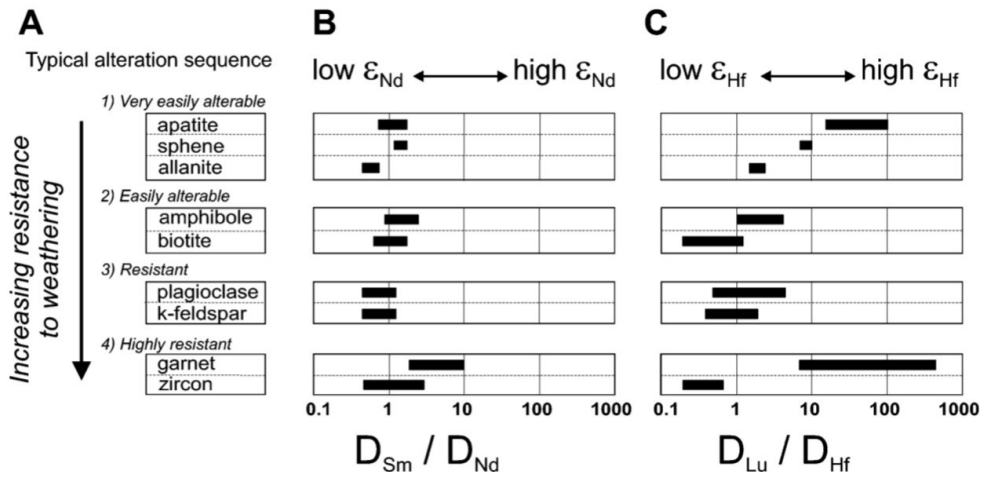

Figure 1.11: The link between Hf isotopes and silicate weathering intensity. (A) Typical sequence of alteration during weathering of granitic rocks. This sequence is based on early studies (Goldich, 1938; Ollier, 1984) and more recent experimental work (Harlavan and Erel, 2002; Erel et al., 2004). (B) and (C) Lu-Hf and Sm-Nd mineral-liquid partition coefficient ratios for most common granite-forming minerals (compiled from http://earthref.org/GERM). Alteration of biotite occurs typically at early stages of granitoid dissolution, but biotite is often loaded with inclusions of accessory minerals (e.g., apatite, sphene, allanite, zircons). *Figure and caption from Bayon et al. 2006.*

---

granites produced **ε**Hf values from ~ +50 to over +300. The authors also investigated specific mineral phases and concluded that apatite, sphene, allanite and garnets were (from most susceptible to least susceptible) the sources of the extremely positive **ε**Hf values (Bayon et al. 2006), figures 1.10 and 1.11.

These studies were furthered by Bayon et al. (2009) where sediment-size fractions from the Congo river deep see fan (part of the Angola basin) were separated and individually analyzed for their **ε**Hf values. This study conclusively demonstrated that the **ε**Hf value were directly related to the sediment fraction-size/composition that was

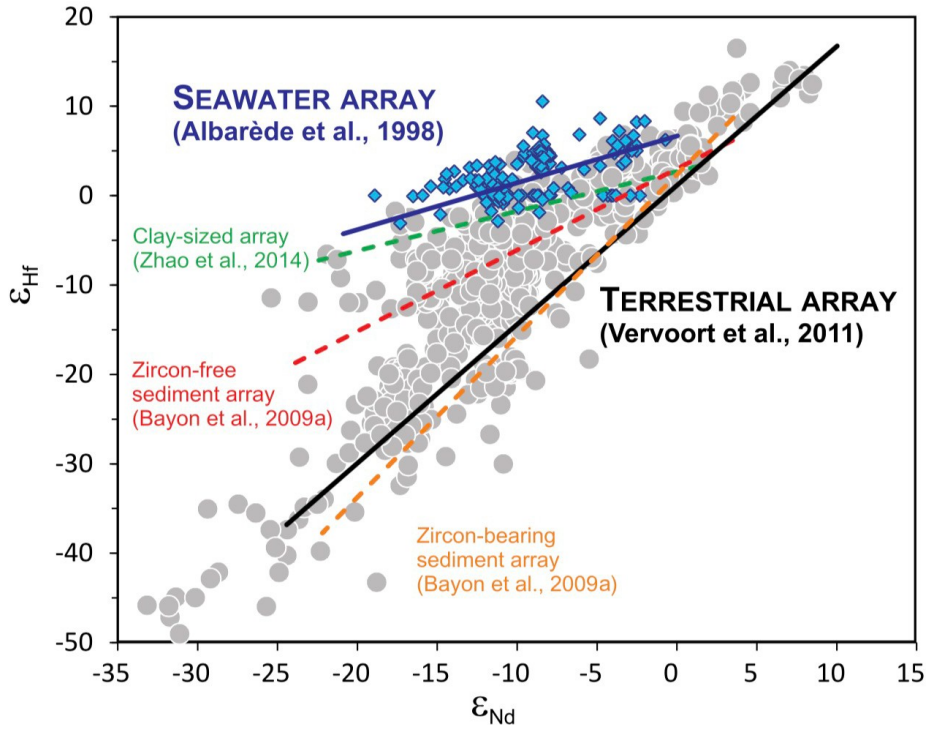

Figure 1.12: A compilation of published Hf and Nd isotopic compositions for fine-grained sediments and other sedimentary rocks. The sediment data (grey circles) include present-day εHf and εNd values for: marine sediments (Vervoort et al., 1999, 2011; Pettke et al., 2002; Vlastelic et al., 2005; Prytulak et al., 2006; van de Flierdt et al., 2007; Bayon et al., 2009a; Carpentier et al., 2009, 2014), river particulates and bedloads (Bayon et al., 2006; Rickli et al., 2013; Garçon et al., 2013, 2014; Garçon and Chauvel, 2014), loess deposits (Chen et al., 2013; Chauvel et al., 2014) and aeolian dust (Lupker et al., 2010; Rickli et al., 2010; Aarons et al., 2013; Pourmand et al., 2014; Zhao et al., 2014). The Seawater Array ($\varepsilon Hf = 0.55 \times \varepsilon Nd + 7.1$; Albarède et al., 1998) and the present-day Terrestrial Array ($\varepsilon Hf = 1.55 \times \varepsilon Nd + 1.21$; Vervoort et al., 2011) are shown for comparison, together with 3 other correlations identified in previous studies for fine-grained sediments (the 'zircon-free sediment array'; $\varepsilon Hf = 0.91 \times \varepsilon Nd + 3.10$; Bayon et al., 2009a), coarse-grained sediments (the 'zircon-bearing sediment array'; $\varepsilon Hf = 1.80 \times \varepsilon Nd + 2.35$; Bayon et al., 2009a), and Mongolian and Chinese dust clays (the 'clay-sized array'; $\varepsilon Hf = 0.45 \times \varepsilon Nd + 2.85$; Zhao et al., 2014). *Figure and caption from Bayon et al. 2016.*

examined. Fractions of turbiditic sands possessed the lowest **ε**Hf values (-27.2 to -31.6), while average siliciclastic sediments possessed values ranging from (-7.1 to -12), both of which were in stark contrast to the finest grained, clay-sized iron-oxide sediments that possessed **ε**Hf from -1.1 to + 1.3. Taken together, and given the fact that all sediments had virtually the same **ε**Nd values (-16) provided strong proof that the **ε**Hf value of a sediment was dependent on the fraction of sediment investigated, further suggesting that zircon-bearing sediments (in this case turbiditic fractions) dominate the **ε**Hf signal, and it is only the finest-grained particles, the clays in this case, that carry the radiogenic **ε**Hf values associated with continental weathering (Bayon et al. 2009).

The most recent studies of **ε**Hf derived from rivers provides an excellent overview of the state of our current understanding. The continued and combined work of Zhao et al. (2014), and Bayon et al. (2016) on different size fractions of sediments have now helped to resolve the "terrestrial array" and "seawater array", which had unknown sources of scatter around both trends into a series of trends, namely by subdividing the terrestrial array (Vervoort et al. 2011) into; (1) The zircon bearing sediment array, (2) the zircon-free sediment array, and the seawater array (Albarède et al. 1998) in to the (3) the clay-sized array, and finally, (4) the true seawater array (Bayon et al. 2009, and Zhao et al. 2014) see Figure 1.12.

Following these studies, a series of riverine-specific studies were initiated to determine if the trends observed in marine sediments could be traced back to a specific source or process. The following three examples exemplify how the processes that govern

εHf values in seawater are uniform and are initiated during terrestrial weathering. The first of these studies we will examine is one by Rickli et al. (2013) that examined the **ε**Hf values of several rivers within the mountainous regions of the Swiss Alps. Guided by the findings in marine deposits these authors collected water samples from four different rivers, which were filtered at a pore size of 0.45 μm, thus the results represent the colloidal and truly dissolved fraction of **ε**Hf values in these rivers. The authors discovered that while Nd values approximated those observed in all rivers, the Hf concentrations were an order of magnitude lower than expected in rivers, especially those that drained Gneissic catchments, presumably due to the formation of new zircon crystals. Comparatively, Hf concentrations were much higher in rivers draining sedimentary materials, presumably due to the interaction with previously weathered and damaged detrital zircons found within the sediments (Rickli et al. 2013). Finally, samples of riverine water taken from the zircon-free regions of the catchments were found to be weathering congruently (i.e. Nd and Hf values follow a 1:1 ratio) as predicted by the "terrestrial array" however, when leaching experiments were performed on sediments from the carbonate portion of the catchment, they produced **ε**Hf as high as +208, however, stoichiometrically these components were far to small to dominate the overwhelming signal of the zircon-dominated weathering profile. Ultimately the study concluded that zircons and their negative **ε**Hf values dominate in regions where low discharge of waters and underlying mineralogies favor negative **ε**Hf values, compared to regions that may experience different weathering regimes and lithologies (Rickli et al., 2013).

Transitioning from low volume catchments to one of the highest volume catchments in the world, Merschel et al. (2017) performed a critical study that examined the entire efflux of the Amazon river, specifically designed to separate all run-off by particle size. Their results are not only striking, but critical in reinforcing much of the previous work performed by previous authors. These authors separated two sample sets collected in November (2013), and June (2014), each sample of water filtered immediately after collection with a 0.2 μm filter, which allowed the authors to subdivide the samples into; (1) samples containing a suspended load of sedimentary particles, (2) samples containing a dissolved load of organic and inorganic components, and (3) the truly dissolved component of the riverine runoff. While all samples taken during this study demonstrated and **ε**Nd values that were not dissimilar to their catchment lithologies, the **ε**Hf values varied directly with the size of particles examined in each sample. Specifically, the larger the particle size, i.e. the suspended load of sedimentary material (containing zircons) exhibited the most negative **ε**Hf values (average ~ -6), while the dissolved particles exhibited a moderately radiogenic signal (average ~ +10), and the truly dissolved fraction exhibited an average **ε**Hf value of ~ +18. These observations correlate well with previous observations made by Rickli et al. (2013), and have greatly advanced the state of understanding to convincingly conclude that the incongruent Hf-Nd signal observed in seawater is derived from incongruent weathering in terrestrial weathering environments, and is masked in the marine environment by sedimentary particles, and can only be observed in regions where all sedimentary influence has fallen away (Merschel et al., 2017).

Finally, the investigation of a third case, in a glacial environment, where weathering is distinctly different then in temperate or tropical zones performed by Rickli et al. (2017), confirms the conclusions of the previous studies and expounds on the factors that influence the **ε**Hf values observed in seawater. This study takes samples from a variety of streams and rivers in the proglacial zone of the Greenland Ice Sheet, near Søndre Strømfjord on the west coast of Greenland. The authors found that the **ε**Hf value observed in their samples not only varied with the specific river sampled (even if it drains the same type of bedrock), but also with the time of year, and the source of the flow (Rickli et al. 2017). Samples from all sources were found to have distinctly negative **ε**Nd values (-42.8 to -37.9), and **ε**Hf values were extremely diverse depending on the sampling and source location. In contrast, **ε**Hf samples examined from glacial rivers that were directly sourced from glacial discharge-streams were observed to have values from -18.3 to -0.9, while those samples that originated from non-glacial streams (i.e. those that do not have a glacier at their source) were far more radiogenic, with values observed between +15.8 and + 46.3. these stark differences were attributed to both the underlying lithology the surficial water was reacting with, as well as the length of time the water had to interact with the exposed mineral beds. Notably it was observed that the longer the riverine waters had to interact with the underlying bedrock, the lower their **ε**Hf values became, this observation was echoed in observations of glacial lakes, which exhibited the same trend, thus, the authors concluded that the **ε**Hf value ultimately observed in the total riverine discharge was partially controlled by the length of time, and the underlying lithologies terrestrial waters interacted with on their way to the ocean (Rickli et al. 2017).

In summary, these studies highlight what are the most impactful elements leading to the **ε**Hf value ultimately observed in any sediment, whether it is a modern sedimentary deposit, or an ancient chemical sedimentary deposit are; (1) what are the source rocks (granitic vs. mafic) and how do their mineralogic properties affect the release of radiogenic vs. non-radiogenic Hf, (2) how old is the lithology being weathered? Due to the extended decay time of ^{176}Lu a significant amount of time must pass before a radiogenic Hf signal can develop, (3) what is the weathering regime, and how intense is it? Is the exposed bedrock immediately subject to rapid and perhaps intense (in the case of high CO_2 environments in the Archean) weathering as observed in the amazon, or have the lithologies experienced slow, or variable weathering such as the case with Glacial weathering, and finally, (4) what size of particles are being examined, and could there be contamination? Each study here has provided evidence that particle size and volume can have a dramatic effect on the **ε**Hf value measured, thus, one must do all that one can to ensure that the in order to detect the races of continental weathering we minimize or eliminate all sources of terrestrial contamination, and only examine those seawater-derived sediments that are as chemically pure as possible.

1.1 Banded Iron Formations

1.1.1 Diagenesis

To be used as a proxy for seawater composition one must be sure that the isotopic signatures recorded in any rock, and in Banded Iron Formations (BIFs) specifically, reflects that of the original isotopic signal created during the samples formation, and not that of some other syn-depositional or post-depositional process. Little work has been done on

the effects of syn- and post-depositional processes on the isotopic signatures found in BIF's, however, a summary published by Bau (1993) based on available evidence suggests these units preserve original isotopic signatures locked in during their formation when appropriate units are selected, and certain chemical criteria are met. Two syn-depositional processes were also identified as being potential sources of isotopic contamination in BIF's, first, the input of clastic contaminants during precipitation, is a particular concern as REE abundances in clastic material can be more than two orders of magnitude higher than in riverine/marine waters and chemical precipitates formed therein. As little as 1% clastic contamination can be sufficient to dominate the REE signal of a BIF, thus it is imperative that one discriminates against analysis of samples containing clastic material. Bau (1993) presents a simple method of identifying such samples by examining the abundance of elements that are regarded as immobile in aqueous solution (Ti, Zr, Hf, Y, Nb, Th, Ta, and Sc); high abundances of these elements in general is likely related to contamination from a clastic source. Based on comparison of the Th, Hf and Sc content of clastic-rich and clastic poor samples from the Dales Gorge BIF (Mt. Bruce Supergroup, Hamersley Basin Western Australia) elevated abundances of all three elements were observed in clastic-rich bands, and samples containing an Sc abundance of 2 ppm or more were considered to be sufficiently contaminated that they should be eliminated from further study.

Secondly, fractionation of elements may also occur during the precipitation of Fe-oxy-hydroxides and/or carbonates from solution, while precipitation of silica has little effect. The REE patterns of both oxide- and carbonate-facies iron formations appears to

be similar suggesting that crystallographic controls do not play a major role in in which REE's are scavenged by each element, however the difference in ionic radii between Fe^{2+} and the trivalent REE's results in the enrichment of HREEs in $FeCO_3$. Scavenging of REEs by Fe-oxy-hydroxides occurs via sorption of REEs provide charged surface sites on FeOOH molecules as they descend through the water column from their location of oxidation at the anoxygenic-oxygenic ocean interface. Therefore the REEs contained in a band of Fe-oxide is related to the initial Fe/REE ratio of the water column, the availability of oxygen, (i.e. the amount and rate of Fe-oxide produced), and the time it takes for FeOOH particles to reach the seafloor and be buried. During large sale formation of BIFs the total amount of FeOOH being formed is in such excess of the REEs present in the water column that essentially all REEs are precipitated, and further precipitation of Fe-oxides results in an increased ratio of Fe-oxide to REEs, but does not disturb the REE pattern preserved. When co-precipitation of Fe-carbonates is observed REE patterns in Fe-oxide precipitates are observed to have a comparative enrichment in the LREE's due to the greater stability of HREE with carbonates mentioned previously. If CO_3^{2-} concentrations were greater in the Precambrian then they are today (possibly due to higher CO_2 concentrations in the atmosphere) this effect may have an increased importance resulting in increased fractionation then is observed today.

Post-depositional processes considered to be significant sources of error by this study are diagenetic effects, metamorphism, hydrothermal interaction and weathering. Little is known about the mobility of REEs during diagenesis, studies of epiclastic sediments, carbonate sediments and cherts have not shown evidence for wide-spread REE

mobility in these materials, while the low concentration of REE's in pore water solutions and coastal sediments suggests there would not be a large impact on REE signatures from diagenetic processes (Bau, 1993 and the references therein). Similarly, even less is known about REE mobility during lithification of FeOOH and $Si(OH)_4$ gels, however experimental research suggests that the trivalent charge and large ionic size of REEs may result in them being essentially immobile within an FeOOH layer. Analysis of REE distribution form consecutive Fe-mineral-rich or quartz-rich bands from the Kuruman iron-formation show highly variable $(Sm/Yb)_{CN}$ and $(Eu/Sm)_{CN}$ ratios, strongly suggesting closed-systems conditions and a lack of REE mobility during diagenesis, otherwise these signals would have been homogenized between adjacent bands, and also indicate that the banding observed in BIFs is a primary, rather than diagenic feature (Bau, 1993).

Based on two previous studies, remobilization or fractionation of REEs during metamorphism is considered to be unlikely, as the water/rock ratios required to produce a change in REE signatures are much too low in iron-formation sequences, as water/rock ratios >100 would be required to produce change. If such conditions were achieved one would expect an increased mobility of LREEs and Eu compared to HREE's and trivalent REEs based on theoretical considerations, and the concentration of HREEs within the crystalline lattice of metamorphic magnetite crystals and LREEs becoming more concentrated along grain boundaries (Bau, 1993). Therefore, theoretical metamorphic fluids released during metamorphism of iron-formations would be comparatively LREE-rich with a positive Eu anomaly, while the rock would develop a LREE depletion and negative Eu anomaly. However, samples of BIF's that have experienced high-grade

metamorphism such as the Isua iron formation (West Greenland) do not show depletion of Eu or LREEs, and those that have experienced intense contact metamorphism (600-700 ˚C) such as iron-formation samples from the northern Midlands greenstone belt (Zimbabwe), are found to have REE_{CN} patterns similar to those of iron-formations at lower metamorphic grade further south, strongly suggestion that these units act as closed-systems during metamorphism. Further evidence of closed-system conditions is provided from the Penge iron-formation (Transvaal Supergroup, South Africa) where detritus-rich bands, in immediate contact with detritus-free bands, are still observed to contain higher REE abundances and lower $(Eu/Sm)_{CN}$ ratios then their detritus-free neighbors (Bau, 1993).

Alteration of REE signatures in iron-formations via hydrothermal fluids is controlled by the fluid composition and physio-chemical environment and may result in either loss or gain of REEs, increase or decrease of $(Sm/Yb)_{CN}$ ratios, and creation of negative or positive Eu_N anomalies. Eu anomalies are most likely to develop under reducing, slightly acidic conditions, with high-temperature fluids. Due to the low effective water/rock ratios significant loss of REEs during hydrothermal processes is likely to be low, while the formation of secondary mineral phases with high mineral/fluid partition coefficients can change REE_N patterns drastically. Thus, samples suspected to contain secondary hydrothermal minerals, either in the form of veining, dissolution and reprecipitation of primary phases, or alteration of primary phases by hydrothermal fluids are unsuitable for study, and samples suspected of having experienced hydrothermal alteration should be excluded from study (Bau, 1993).

Disruption of primary REE signatures via weathering processes depends on the water/rock ratio experienced, the primary minerals present, and the secondary minerals that form. Due to the wide range of source-rock mineralogy and physiochemical conditions that can be present during weathering of a sample (fO_2, fCO_2, pH, ligands for complexation) both LREEs and HREEs can become more or less mobile depending on the conditions. For this reason, and for reasons of simplicity during analysis, any sample exhibiting signs of weathering should be excluded from study (Bau, 1993).

In summary, alteration of primary REE signatures in iron-formations is possible due to a variety of syn- and post-depositional processes, however, BIFs in general can be considered to be resistant to alteration if the right conditions are maintained since their formation. REE contamination of BIFs is most likely to occur during deposition via clastic input, hence any sample containing a concentration of Sc > 2 ppm should be excluded from analysis. BIF's effectively behave as closed systems during diagenesis and metamorphism, however later events such as hydrothermal alteration and weathering can greatly disrupt REE concentrations and rations, and care should be taken to exclude BIF samples that may have been hydrothermally altered or show signs of weathering from further study.

1.2 Previous Work

1.2.1 Decoupled Hf-Nd isotopes in Banded Iron Formations

The premier paper presented by Viehmann et al. (2014) in the Journal *Geology* provides the first combined Hf and Nd isotope data for pure samples of a Banded Iron

Formation (BIF), suggesting that these units can be used to elicit a proxy signal for continental weathering. The samples selected for analysis were derived from the 2700 Ma Temagami BIF found in the Abitibi Greenstone Belt of north-central Ontario, Canada; a 200 m thick Algoma-type BIF (suggesting hydrothermal contributions of Hf and Nd are likely) that has undergone greenschist facies metamorphism since deposition, and contains no, or only minute, amounts of aluminosiliciclastic detritus. REY patterns of the Temagami BIF are reported to appear similar to those of modern seawater, including positive La, Gd and Y anomalies, and light REY depletion, but lack positive Eu, and negative Ce anomalies; which, combined with previous work on this BIF referenced therein, allows the authors to conclude that there is strong evidence to support a seawater derived origin of Hf, Nd and REY in this formation.

ICM-MS analysis of 9 BIF samples produced **ε**Nd values ranging from +0.2 to +3.0, with six samples clustering at +1.0 ± 0.3 and **ε**Hf values ranging from +6.7 to +24.1, with a cluster of seven samples falling between +6.7 and +9.6. In comparison, Temagami shales show **ε**Nd values between +2.4 and +2.7 and **ε**Hf values between +4.6 and +5.0. (Figure 1.13) These data were also used to test the ^{147}Sm-^{143}Nd and ^{176}Lu-^{176}Hf isochron systems to determine, and confirm, the age of the BIF, which was found to overlap within uncertainty the U-Pb emplacement ages determined for underlying metavolcanics (the ^{147}Sm-^{143}Nd isochron yielding an age of 2605 ± 3 Ma and the ^{176}Lu-^{176}Hf isochron yielding an age of 2760 ± 120 Ma respectively) compared to the U-Pb age of 2687 ± 2 Ma.

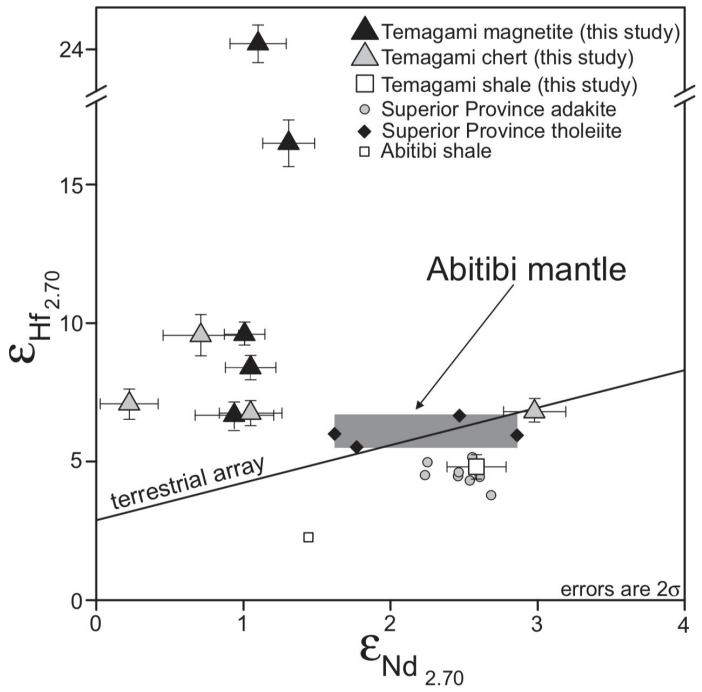

Figure 1.13: Plot of $\varepsilon Hf_{2.7Ga}$ versus $\varepsilon Nd_{2.7Ga}$ for Temagami (Canada) chert and magnetite layers and Temagami shale sample SMS-8, compared to terrestrial array (Vervoort et al., 1999), tholeiites and adakites from Superior Province (Polat and Münker, 2004), and Abitibi shale (Vervoort et al., 1999). Compared to $\varepsilon Nd_{2.7Ga}$, corresponding $\varepsilon Hf_{2.7Ga}$ values are more radiogenic (even more radiogenic than Neoarchean mantle), demonstrating that decoupling of ε_{Hf} and ε_{Nd} typical of modern seawater already prevailed in Neoarchean. *Figure and caption from Viehmann et al. 2014.*

These data are interpreted to indicate, and support, a significant contribution of Hf and Nd to Archean seawater from black smoker-type hydrothermal systems, however they are not identical to the estimates of the Abitibi mantle values. Nd is found to plot below (less radiogenic) the suggested values of +2.5 ± 1 for the Abitibi mantle, suggesting that Nd is a mix of both hydrothermally derived and continental Nd, while in contrast, Hf plots above (more radiogenic) then suggested Abitibi mantle values, or the Temagami shale

values. Based on the determination of Hf in 6 samples with average **ε**Hf values in excess of the Abitibi mantle, and two samples with extremely radiogenic values (~6-10 verses ~16 and ~24 respectively), the authors propose that the Temagami BIF has recorded Hf-Nd values that fall on the "seawater array" as opposed to the "terrestrial array" as defined by Vervoort et al. (1999). The authors also interpret these data to indicate that by the time of formation of the Temagami BIF, 2.7 Ga ago, a significant proportion of continental crust must have been exposed to sub-aerial weathering to account of the more radiogenic Hf signatures observed in these samples, a result of the decoupled preferential weathering of radiogenic-Hf-rich minerals vs. non-radiogenic-Hf-rich minerals such as zircon. This finding is further suggested to be inconsistent with models for crustal evolution that suggests flooded continents with as little as (4% of current) exposed landmass at this time in Earth's history.

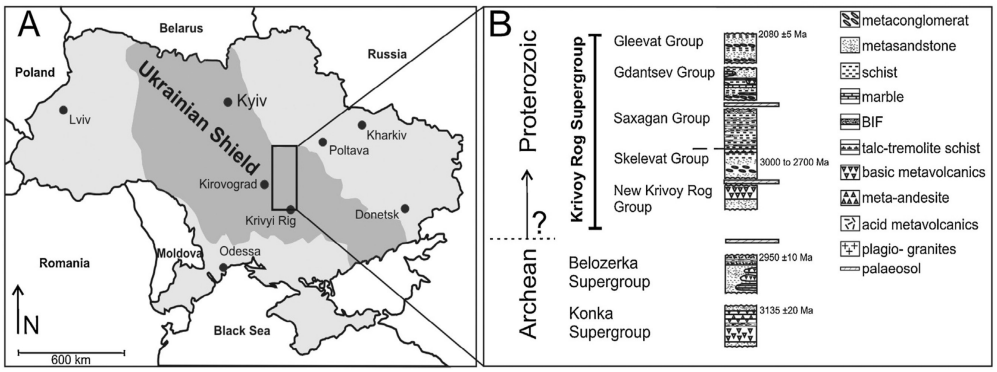

Figure 1.14: Location of the (A) Krivoy Rog area in the Ukrainian Shield, Central Ukraine, with (B) detailed stratigraphy of the Archean Konka and Belozerka Supergroups and the chemico-clastic Late Archean to Early Proterozoic Krivoy Rog Supergroup (modified from Kulik and Korzhnev, 1997). *Figure and caption from Viehmann et al. 2015.*

Since this premier study Viehmann and colleagues (Viehmann et al. 2015; Viehmann et al. 2018) have also investigated data from a second locality (Figure 1.14), the superior-type, Krivoy Rog BIF found in central Ukraine. Underlying siliciclastic units containing zircons have been dated using U-Pb and found to yield ages between 3.0 and 2.7 Ga., while Sm-Nd values from younger metavolcanics can only be dated as far back at 2.0 Ga. Sm-Nd errorchron data from these deposit produce an apparent age of 2.4 ± .35 Ga., while the presence of large Eu anomalies in REE data from all samples lead the authors to favor an order age of ~ 2.6 Ga., as these signals are ubiquitous in the Archean and extremely rare in the Proterozoic (Viehmann et al. 2015).

The entire Krivoy supergroup has undergone greenschist to amphibolite grade metamorphism. The BIF (up to 1400 m thick) of the Saxagan group has been interpreted to have been deposited during transgressive-regressive sequences of the semi-isolated Krivoy sea. Specific samples studied were composed of mainly magnetite and quartz with minor siderite, or hematite and low-grade metamorphic minerals such as amphibolies and chlorites. Based on REE data samples were subdivided into “pure BIF” those showing seawater-like REE patterns (2 samples), and “impure BIF” (6 samples) based on the amount of race element contamination, samples containing Zr concentrations <2.2 ppm were designated as impure. BIF samples were found to possess $\boldsymbol{\varepsilon}Nd_{2.60}$ Ga varying between −2.3 ± 0.4 and +0 ± 0.4, while the $\boldsymbol{\varepsilon}Hf_{2.60}$ values exhibit an extreme range of values from nearly chondritic, -0.91 ± 1.2, to strongly positive, +60 ± 1.0, and a Lu-Hf errorchron of 2775 ± 160 Ma, suggesting little alteration occurred during amphibolite-grade metamorphism that occurred in the region at ~ 2.0 Ga. The authors attribute the wide range

in Hf values between pure and impure BIF to represent a mixing curve between the truly dissolved, dissolved, and the suspended load of Hf derived from rivers as described by Merchel et al. (2017), and that aberrations from this trend represent mafic, fine-grained, wind-blown particles entering with a prevalence of radiogenic-Hf over particles derived from the dissolved or suspended fraction of rivers. These results support previous data obtained from the Temagami BIF, and further strengthen the case that Nd-Hf decoupling occurring in terrestrial environments, and that that riverine sorting has likely played a major role in the detection of this signal over geologically significant periods of time.

1.3 Sample Sites

Eoarchean Banded Iron Formations

1.3.1 Isua Banded Iron Formation

Much of the earliest history of our planet's surface has been lost to the continual processes of crustal recycling (i.e. subduction and volcanism) that continue to shape the face of our world today. There are however some few regions that still preserve rocks from Earth's earliest history, the oldest, and one of the most well preserved suits of these rocks are the metavolcanics and metasedimentary rocks of the Itsaq Gneiss Complex (located approximately 150 km northeast of Godthåb on the western coast of Greenland) within which can be found the famous Isua banded iron formation (Figure 1.15). The Isua BIF, dated to be 3.70 ± .7 Ga (Moorbath et al. 1973), a chemical sediment like all BIFs represented our first glimpse into the chemistry and conditions of Earth's early oceans (though, as noted below other localities have been discovered since this time). Unfortunately, this locality has been subject to several metamorphic overprinting events.

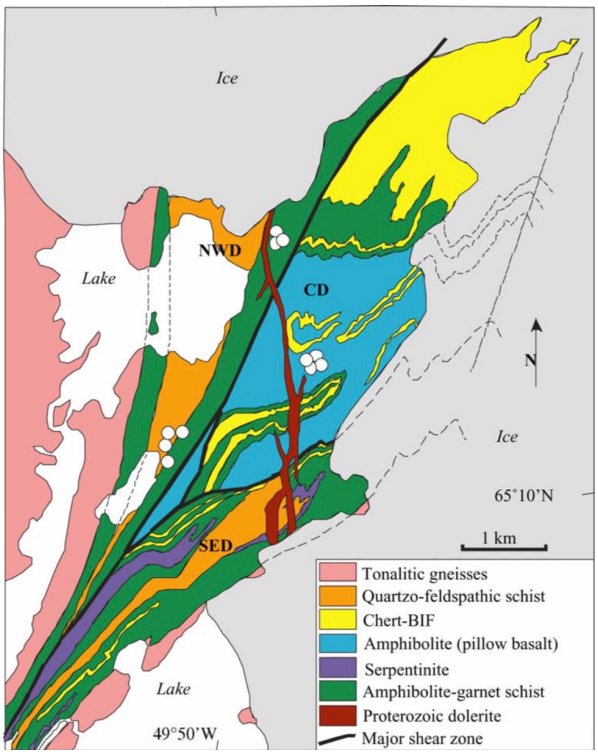

Figure 1.15: Geological map of the eastern part of the Isua greenstone belt. NWD: northwest tectonic domain; CD: central tectonic domain; SED: southeast tectonic domain, modified from Appel et al. (1998). Open circles show sample locations. *Figure and caption from Polat et al. 2005.*

The regional greenstone belt geology was assembled at about 2750 Ma, which combined several different sedimentary and volcanic terrains resulting in regional metamorphic overprints that range from upper greenschist facies to amphibolite grade metamorphism (Polat et al. 2005). Due to the differences in spatial deposition, minerals present, and overall REE profiles a number of different types of BIF have been identified, specifically: (1) quartz-magnetite BIF; (2) magnesian BIF; (3) aluminous BIF; (4) graphitic BIF; (5) Mg-Fe carbonate BIF; and (6) Ca-Mg carbonate BIF (Dymek and Klein, 1988).

Their data also suggested that the Isua BIFs most closely resembled other late Archean BIFs deposited in and around hydrothermal vents (Algoma type BIFs) and were likely formed in a similar manner.

Polat et al. (2005) agree with, and further this theory suggesting that as a natural consequence of a hotter young mantle on Earth, the preponderance of pillow basalts associated with the Isua BIFs would have provided ample reduced iron and other metals that would have been leached from the crust by hydrothermal activity, and their uncommon preservation may be due to subduction of hydrated mid-ocean ridges, the deposition of supracrustal rocks, combined with the underplating of these regions by TTG-type magmas, may have allowed these regions to be preserved as the addition of felsic material would have increased their buoyancy, possibly preventing them from being subducted. Considering the variety of BIF types present here, we simplified our study by selecting the most iron/silica rich samples, with 42.4-58.6% Fe_2O_3 and 34.5-58.1% SiO_2, respectively, for this study. Samples were kindly provided by Stephen Mojzsis and Kurt Konhauser.

1.3.2 Nuvvuagittuq Banded Iron and Banded Silica Formation

Located in the northeastern superior province of Québec, Canada, on the east coast of the Hudson Bay, the Nuvvuagittuq banded iron (BIFs) and banded silica formations (BSFs) are the oldest currently known examples of banded iron chemical precipitates, dating to the Eoarchean (≥ 3.75 Ga) in North America, as determined by zircons from trondhjemitic gneisses in the Nuvvuagittuq succession (Mloszewska et al., 2012). The Nuvvuagittuq greenstone belt is composed of an area ~10 km^2, and consists of volcano-

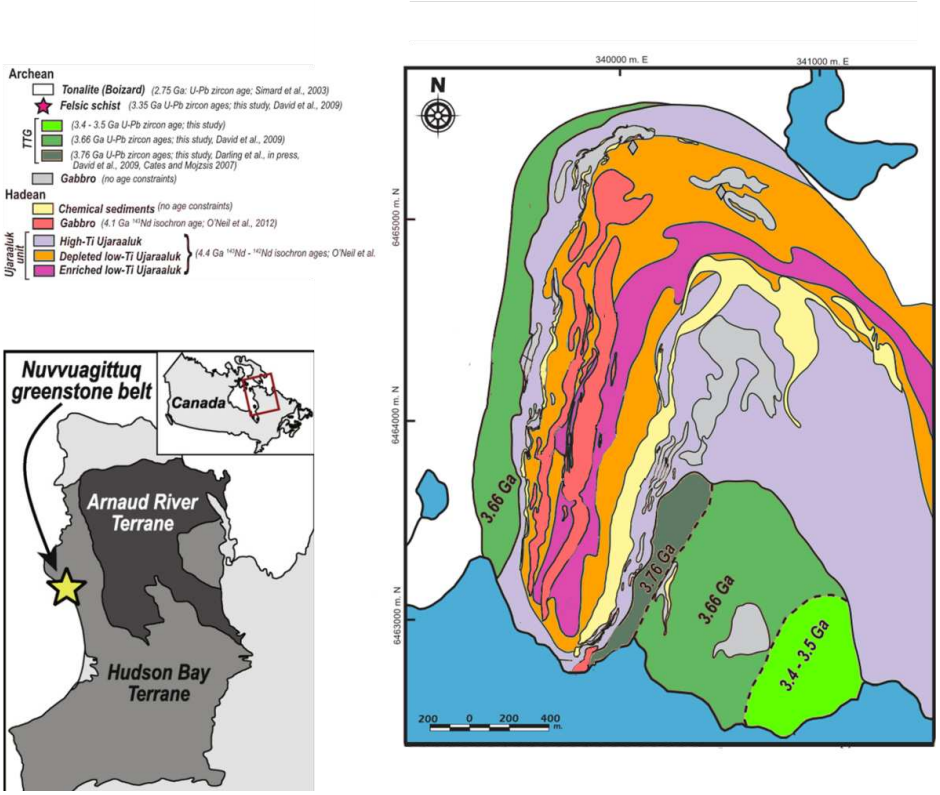

Figure 1.16: Geological map of the Nuvvuagittuq greenstone belt (modified from O'Neil et al. 2011). Yellow regions represent areas where BIF and BSF are found. *Figure and caption from Mloszewska et al., 2012.*

sedimentary sequences interspersed with BIF's and BSF, located in an isoclinal, north-plunging synform, that has been refolded into an open south-facing synform, which has experienced extensive retrograde metamorphism from upper amphibolite/lower granulite facies in the east down to greenschist facies in the west, corresponding to maximum temperatures as high as ~640˚C for the eastern sections of this succession (O'Neil et al. 2011, Mloszewska et al., 2012). The BIFs are composed of 5-30 meter-wide units of alternating magnetite and grunerite bands with variable amounts of finely layered quartz, which outcrop continuously in the west and discontinuously in the east. BSFs are located

50 m up section from the BIFs and outcrop continuously in the western limb of the fold (Figure 1.16), consisting of Fe-Ca-Mg silicates with quartz bands, which grades into a 100 m wide cherty unit of recrystallized quartz and disseminated pyrite (Mloszewska et al., 2012).

Bulk geochemistry for the BSF is characterized by high, but variable concentrations of SiO_2 (28-90 wt.%), $Fe_2O_{3\ total}$ (2-55% wt.%), MgO (2-12 wt.%) and CaO (3-16 wt.%), and have positive La/La^* anomalies (2.31±1), positive Eu/Eu^* anomalies (1.84±0.16), superchondritic Y/Ho ratios (37.40±6.83), depleted LREE and MREE relative to HREE, and an overall REE+Y profile similar to modern-day seawater, with the exception of Eu and Ce anomalies. BIF bulk geochemistry is characterized by high, variable concentrations of SiO_2 (33-63 wt.%), and $Fe_2O_{3\ total}$ (32-66 wt.%), high Cu and S concentrations suggestion a contribution from sulfide minerals, positive La/La^* anomalies (1.73±0.34), positive Eu/Eu^* anomalies (2.21±0.44), superchondritic Y/Ho ratios (33.82±2), depleted LREE and MREE relative to HREE, and an overall REE+Y profile similar to modern-day seawater with the exception of positive Eu and absent Ce anomalies (Mloszewska et al., 2012). The absence of any negative Ce anomalies in these samples is inferred to indicate an overall anoxic water column (as soluble Ce(III) is rapidly oxidized to insoluble Ce(IV) in oxic seawater), while consistently positive Eu anomalies are interpreted as indicating that basinal waters were strongly influenced by high-temperature hydrothermalism there has been little REE+Y mobility since deposition (Mloszewska et al., 2012). Petrographic evidence suggests that the precursors of both units consisted of ferric-oxyhydroxides, amorphous carbonate, silica phases rich in Ca-Mg-Fe and amorphous silica, with an

insignificant clastic input to the system. Presently observed magnetite in these units is thought to be a metamorphic by-product of primary hematite and siderite, quartz in these units is the stable produce of initially amorphous silica precipitates, while low Al_2O_3, TiO_2, Zr, Hf, Ta and Th concentrations suggest a lack of clastic input during the deposition of these samples. Samples for this study were kindly provided by Kurt Konhauser.

1.3.3 Moodies Group Banded Iron Formation, Paleoarchean

The Moodies Group banded iron formation, comprised of several discreet bands of iron stone 1-10's of meters thick, is located in one of the best preserved, ancient sedimentary sequences known to date, the 3.2 Ga Barberton Greenstone Belt, located in the Eastern-most region of South Africa. The entire sequence has undergone greenschist facies metamorphism, and the banded ironstone rich intervals are found within successions of shallow marine sandstones and can be identified as having five different lithofacies over a 63 m transect through a local gold mine; (1) predominantly siliciclastic beds, (2) cm-scale packages of closely spaced, laminated iron-minerals, (3) chert beds with concretions, (4) non-laminated sandstones and (5) a volcanic tuff (Bontognali et al. 2013).

The BIF first appears as being interbedded with cm-scale wavy sandstones, without notable volumes of chert. As the frequency of the iron-rich regions increases and siliclastics become more scarse the first chert concretions appear, and chert beds and concretions are always preceded and followed by iron-rich layers which are often lenticular in shape and laterally heterogeneous. The section is then interrupted by a 0.6 m-thick bed of volcanic tuff, after which the thickness of the chert and iron layers increases, and the interbedding

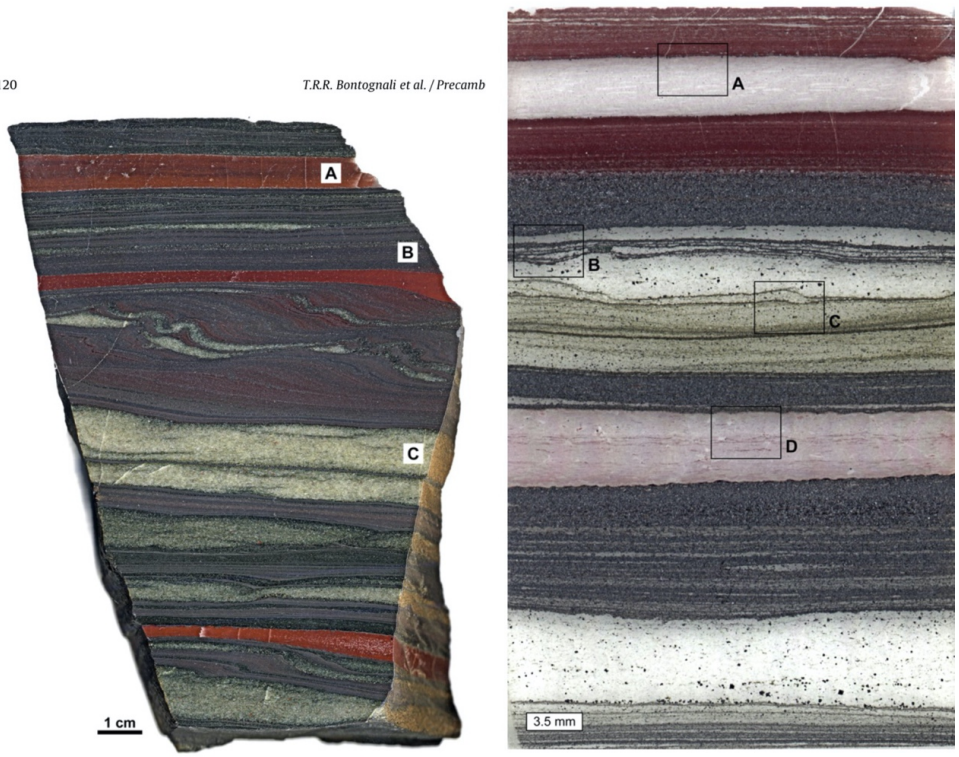

Figure 1.17: (Left panel) Photograph of a polished slab of Moodies BIF. (A) Chert concretion. (B) Sub- mm scale laminations of iron-bearing minerals (mainly magnetite and hematite). (C) Siliciclastic bed. Chert concretions variably show mm to sub mm-scale internal laminations due to the variable amount of incorporated iron minerals. Iron-rich laminations are due to both the fine interlamination with siliciclastic material and the variable amount of surrounding chert. (Right panel) Large-scale photograph representative of a Moodies BIF polished sample.(A) Contact between two chert beds. The color of the chert varies from dark red to almost transparent depending on the concentration of microscopic iron minerals (primarily hematite). (B) Iron-rich microbands finely interlaminated with siliciclastic grains (mainly fine quartz sand). (C) Siliciclastic bed showing laminations comprised of sand draped by iron-bearing minerals. (D) Chert bed including discontinuous laminae comprised of iron minerals. *Figure and caption from Bontonali et al. 2013.*

of sandstone decreases until an interval, several meters, thick is reached where the banding of the BIF is best expressed; the pattern then reverses itself grading backing into sandstones containing wavy lamination, cross stratification and soft sediment deformation structures (Bontognali et al. 2013). The iron-rich laminations are commonly sub-mm in scale and do not contain macroscopic globule or granular regions, the layers are composed of digenetic, often euhedral magnetite, that replaced or overgrew initial hematite, and sulfide minerals such as pyrite can occasionally be found in the iron mineral-rich lamina. Unweathered chert layers appear red due to fine-grained hematite laminations within, and can range in size from mm to ~7-8 cm in thickness, however, when they occur as isolated chert beds the are often nodular in shape, a morphology not observed in the iron or clastic-rich layers. Carbonatious material has also been observed in association with magnetite-rich layers, suggesting it may have formed by reduction of hematite with organic matter, though to date no microfossils have been confirmed in the Moodies Group BIF (Figure 1.17).

Overall the mineralogy, association with siliciclastic materials and greater geological context suggest that the Moodies Banded Iron formation was deposited in on a shallow marine shelf, below wave base, but near enough to sedimentary inputs that occasional siliciclastic grains were deposited within or alongside the BIF. Finally, the occurrence of chert only between iron rich layers suggests that the deposition of silica may have been directly tied to the oxidation of reduced iron in the water column, lining the Fe and Si cycles in Archean oceans (Bontognali et al. 2013).

1.3.4 Braemar Ironstones, Neoproterozoic

The Braemar ironstone formation is located in the south Australian, Adelaide Geosyncline, a Neoproterozoic to Cambrian age sedimentary basin, comprising one of the most complete and well-preserved Neoproterozoic successions, including evidence for two major glacial successions (Lottermoser and Ashley, 2000). The ironstones, part of the Umberatana group, are found in two stratigraphically continuous units of the Yudnamutana subgroup, the lower Pualco Tillite, and the overlying Benda Siltstone. In the Yunta area, 4 to 6 lenticular ironstone units are observed to grade into both the host diamictites and siltstones, and prominent ironstone outcrops are interbedded with diamictites, carbonate-rich rocks, quartzites, siltstones and manganiferous siltstones. Generally, the Braemar iron formations consists of lenticular, laminated, and diamictic ironstones interbedded with calcareous and dolomitic siltstones and thin quartzite units, and can be subdivided into two facies, the diamictic and the laminated ironstones, which are macroscopically different but compositionally identical (Figure 1.18).

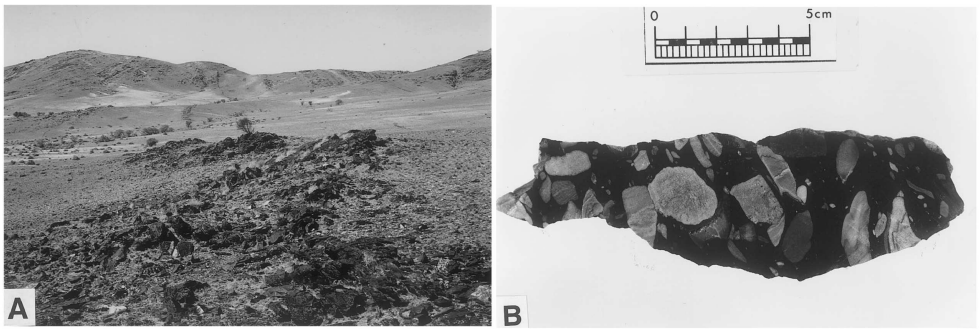

Figure 1.18: (A) Typical outcrop of the Braemar ironstone facies. Ironstone is intercalated with carbonate-bearing siltstone and minor diamictite and dolostone. Near Bimbowrie Hill, AMG: 420700 mE, 6455650 mN. (B) Diamictic ironstone with recrystallised carbonate-rich siltstone, quartz and carbonate clasts (sample BR24). Razorback Ridge, AMG: 379740 mE, 6352770 mN. *Figure and caption from Lottermoser and Ashley, 2000.*

Laminated ironstones and the matrix of the diamictic ironstones are fine-grained and composed of primarily of magnetite, hematite and quartz, with minor muscovite, chlorite, Biotite, carbonate, apatite, plagioclase and tourmaline. The lamination is generally well developed, with laminae defined by the relative abundance of magnetite and hematite, ranging from ~80 to 20 wt.%. Detrital mineral grains and lithic clasts occurring in both units are angular to sub-rounded and are composed of quartz, carbonate, plagioclase, K-feldspar, muscovite, tourmaline, foliated sediments, siltstones, quartzites and quartzofeldspathic rocks. In contrast, diamictic ironstones are massive and contain clasts ranging in size from 10 mm to 1.2 m, with similar angularity and rounding to the lithic clasts found in laminated ironstones.

Laminated ironstones can exhibit large variations in modal proportions of rock-forming minerals and Fe-oxides, with lamina displaying both sharp and gradational transitions to siltstone layers, in the latter case magnetite is observed to decrease while quartz and silicate content increases. Sedimentary structures can also present locally and include cross-laminations, microfaulting, piercement of laminae and micro- to meso-scale folding suggesting soft sediment deformation may have occurred. Since deposition, the Braemar ironstones have undergone greenschist facies regional metamorphism and deformation, experiencing temperatures of ~360-400˚C, as indicated by chlorite composition growth calculations (Lottermoser and Ashley, 2000).

The major oxide components of the laminated irons stones are SiO_2 and Fe_2O_3 comprising >70 wt.% of the rock. Minor constituents include Al_2O_3 ranging from 0.28 to 10.64 wt.%, CaO, K_2O, MgO, Na_2O and LOI, variations in which tend to be correlated to higher Si content, and suggest the addition of plagioclase, carbonate, biotite, chlorite and muscovite. Trace element constituents of the ironstones show large-scale variations dependent on type and quantity of minerals present. They are depleted in most transition metals (Sc, V), high field strength elements (Nb, U, Th, Zr, Hf, Pb, LREE) and large ion lithophile elements (Ba, Sr, Rb) compared to the upper continental crust. Weak correlations of Fe with several elements including As, Cu, Sb, V and Zn suggest a hydrothermal source of these elements, thus the Braemar ironstones represent chemical sediments with a minimal to significant contribution from detrital materials (Lottermoser and Ashley, 2000).

All ironstones were found to display REE patterns with variable LREE depletions, negative Ce anomalies and no Eu anomalies, with the exception of one sample which exhibited a distinctly positive Eu anomaly. From these data the Braemar ironstones have been subdivided into two different suites, siliceous-aluminous ironstones if SiO_2 >40 wt.% and Al_2O_3 > 6 wt.% and silica-alumina-poor if SiO_2 <40 wt.% and Al_2O_3 <6 wt.%. Silica-alumina-poor samples were found to have low concentrations of REE with moderate depletion of LREE and either depletion or enrichment of HREE. Siliceous-aluminous ironstones display REE patterns only slightly depleted LREE. The similarity of the REE patterns of Braemar siltstones and siliceous-aluminous ironstones suggests that these sediments gained their REE patterns from detrital sources, however, a different REE source

is implicated for the silica-alumina-poor samples where REE was gained during chemical precipitation from seawater (Lottermoser and Ashley, 2000).

Braemar ironstone facies show positive correlations of Al and Si with Ti, Ca, Mg, K, Ga, Hf, Rb, Sc, Sr, Ta, Th, Zr, La and Ce indicating that these elements are derived from detrital sources. When plotted on a detrital-chemical sediment mixing curve the ironstones cluster toward the chemical sediment endmember. REE's in the silica-alumina-poor samples (closest to the chemical sediment end member) differ enough from detrital sediment values that they are considered to be consistent with oceanic values, similar to those obtained for modern coastal seawaters.

Associated dolostones capping the Braemar facies (interpreted as inorganic cold-water deposits), as well as from ferroan dolomite and ferroan calcite within siltstones and ironstones have been analyzed and are considered to provide paleoenvironmental information on the postglacial marine transgressional environment. Carbon and oxygen isotope information from 15 samples selected from material displaying no petrographic evidence of carbonate mobilization or veining from within the Braemar facies display widely variable carbon isotope values ($\partial^{13}C_{PDB}$ -5.5 to +0.9‰ however most are negative) and oxygen values ranging from $\partial^{18}O_{SMOW}$ +10.6 to +29.5‰, which coincide with other values interpreted as support for major Neoproterozoic glaciations.

As indicated by stratigraphic, sedimentological and carbon/oxygen isotope data, glaciation played an important role in the formation of the Braemar ironstones. The occurrence of

detrital fragments in laminated ironstones and the formation of diamictic-ironstones suggests the Braemar ironstones accumulated in a basin along the border of a glaciated continental landmass. During glacial episodes the coastal waters were covered in a thick icecap which effectively cutting them off from atmospheric oxygen allowing the underlying ocean to become anoxic (due to decay of organic matter), and hydrothermal iron to accumulate in solution. During transgressive interglacial periods of the Pualco glacial event when ice cover retreated Fr-rich waters were exposed to oxygen creating the ironstone deposits formed from direct chemical oxidation of Fe in seawater, allowing the contemporaneous deposition of dropstones and clastic debris filled laminated ironstones onto the seafloor. As exhibited by the marine-like REE signatures of silica-alumina-poor samples and given the hydrothermal signature of Fe determined for the Braemar ironstones, these sediments were almost certainly deposited in an oceanic environment rather than a lacustrine environment as had been suggested by previous authors (Lottermoser and Ashley, 2000).

1.4 Summary

The Hf-Nd isotope systems are powerful tools for tracking both differentiation and evolution of the lithosphere and crust, as well as unraveling the sources of Hf and Nd in the words oceans. Combined, these isotopic systems have allowed us to investigate the effect of weathering not only on differing lithologies, but this isotopic system has also shed light on the effects of weathering rate, and how the components of weathered sediments result in different REE contributions to sedimentary deposits and oceanic reservoirs based on the size fraction of riverine components. Moreover, studies have found that both modern

and ancient chemical sedimentary deposits, namely manganese nodules and banded iron formations, can capture these weathering signals and preserve them with fidelity over geologically significant periods of time.

In this thesis, we explore the utility of the Hf-Nd system by trying to extend our current understanding of the Hf-Nd record preserved in banded iron formations from the Neoproterozoic to the Paleo- and Eoarchean, with the intent of providing a clearer picture of continental emergence and weathering throughout Earths history. After a detailed methodology section, this thesis is organized into discrete paper-based chapters that explore the results we have obtained from (1) the 3.2 Ga Moodies banded iron formation, (2) the ~750 Ma Braemar iron formation, and finally (3) the 3.8 Ga Isua banded iron formation, supplemented with several samples from other Eoarchean iron formations. We conclude the thesis with a broad summary chapter, which presents both overall perspectives on these data, as well as specific recommendations for how future work may be made more accurate, how the effects of metamorphic events may be further understood and overcome. This final chapter emphasizes both the need for more data, but also new avenues and lithologies that may be pursued to further resolve the story of continental emergence and its evolution over time.

1.5 References

Albarède, F., Simonetti, A. Vervoort, J.D., Blichert-Toft, J., Aouchami, W., (1998). A Hf-Nd isotopic correlation in ferromanganese nodules. *Geophysical Research Letters,* 25, 3895-3898.

Barrat, J.A., Keller, F., and Amossé, J., (1996). Determination of Rare Earth Elements in Sixteen Silicate Reference Samples by ICP-MS After Tm Addition and Ion exchange separation. *Geostandards Newsletter,* 20, 133-139.

Bau, M., (1993). Effects of syn- and post-depositional processes on the rare-earth element distribution in Precambrian iron-formations. *European Journal of Mineralogy*, 5, 257-267.

Bau, M., and Koschinsky, A., (2006). Hafnium and meodymium isotopes in seawater and in ferromanganese crusts: The "element perspective". *Earth and Planetary Science Letters,* 241, 952-961.

Begg, G.C., Griffin, W.L., Natapov, L.M., O'Reilly, S.Y., Grand, S.P., O'Neill, C.J., Horonsky, J.M.A., Proudjom Djomani, Y., Dean, T., Bowden, P., (2009). The Lithospheric architecture of Africa. Seismic tomography, mantle petrology and techtonic evolution. *Geosphere,* 5, 23-50.

Bayon, G., Vigier, N., Burton, K.W., Brenot, A., Carignan, J., Etoubleau, J., (2006). The control of weathering processes on riverine and seawater hafnium isotope ratios. *Geology*, 34, 433-436.

Bayon, G., Burton, K.W., Soulet, G., Vigier, N., Dennielou, B., Etoubleau, J., Ponzevera, E., German, C.R., Nesbitt, R.W., (2009). Hf and Nd isotopes in marine sediments: Constraintes on global silicate weathering. *Earth and Planetary Science Letters,* 277, 318-326.

Bayon, G., Skonieczny, C., Delvigne, C., Toucanne, S., Bermell, S., Ponzevera, E., André, L., (2016). Environmental decoupling in World river clays. *Earth and Planetary Science Letters,* 438, 25-36.

Bell., E.A., Harriston, T.M., McCulloch, M.T., Young, E.D., (2011). Early Archean crustal evolution on the Jack Hills Zircon source terrane inferred from Lu-Hf, $^{207}Pb/^{206}Pb$, and $\partial^{18}O$ systematics of Jack Hills zircons. *Geochemica et Cosmochimica Acta*, 75, 4816-4829.

Belousova, E.A., Kostitsyn, Y.A., Griffin, W.L., Begg, G.C., O'Reilly, S.Y., Pearson, N.J., (2010). The growth of continental crust: Constraints from zircon Hf-isotope data. *Lithos,* 119, 457-466.

Bontognali, T.R.R, Fischer, W.W and Föllmi, K.B., (2013). Siliciclastic associated banded iron formation from the 3.2 Moodies Group, Barberton Greenstone Belt, South Africa. *Precambrian Research,* 226, 116-124.

Cawood, P.A., Hawkesworth, C.J., and Dhuime (2013). The continental record and the eneration of continental crust. *GSA Bulletin*, 125, 14-32.

Chen, T.-Y., Ling, H.-F., Frank, M., Zhao, K.-D., Jiang, S.-Y., (2011). Zircon effect alone insufficient to generate seawater Nd-Hf isotope relationships. *Geochemistry Geophysics Geosystems*, 12, 1-9.

Chen, T.-Y., Li, G., Frank, M., Ling, H.-F., (2013). Hafnium isotope fractionation during continental weathering: Implications for the generation of the seawater Nd-Hf isotope relationships. *Geophysical Research Letters,* 40, 916-920.

Derry, L.A. and Jacobsen, S.B., (1990). The chemical evolution of Precambrian seawater: Evidence from REEs in banded iron formations. *Geochemica et Cosmochemica Acta,* 54, 2965-2977.

Dhuime, B., Hawksworth, C.J., Cawood, P.A., Storey, C.D., (2012). A Change in the Geodynamics of Continental Growth 3 Billion Years Ago. *Science,* 335, 1334-1336.

Dymek, R.F., and Klein, C., (1988). Chemistry, Petrology, and Origin of Banded Iron-Formation Lithologies from the 3800 Ma Isua Supracrustal Belt, West Greenland. *Precambrian Research,* 39, 247-302.

Elderfield, H., and Sholkovitz, E.R., (1987). Rare earth elements in the pore waters of reducing nearshore sediments. *Earth and Planetary Science Letters,* 82, 280-288.

Flament, N., Coltice, N., and Rey, P.F. (2013). The evolution of the $^{87}Sr/^{86}Sr$ of marine bcarbonates does not constrain continental growth. *Precambrian Research,* 229, 177-188.

Godfrey, L.V., Lee, D.-C., Sangrey, W.F., Halliday, A.N., Salters, V.J.M., Hein, J.R., White, W.M., (1997). The Hf isotopic composition of ferromanganese nodules and crusts and hydrothermal manganese deposits: Implications for seawater Hf. *Earth and Planetary Science Letters,* 151, 91-105.

Godfrey, L.V., Zimmermann, B., Lee, D.-C., King, R.L., Vervoort, J.D., Sherrell, R.M., Halliday, A.N., (2009). Hafnium and neodymium isotopic variations in NE Atlantic seawater. *Geochemistry, Geophysics, Geosystems*, 10, 1-13.

Haley, B.A., Klinkhammer, G.P., and McManus, J., (2004). Rare earth elements in pore waters of marine sediments. *Geochimica et Cosmochimica Acta,* 68, 1265-1279.

Harrison, T.M. (2009). The Hadean Crust: Evidence from >4 Ga Zircons. *Annual Review of Earth and Planetary Sciences,* 37, 470-505.

Homann, M., Sansjofre, P., van Zuilen, M., Heubeck, C., Gong, J., Killingsworth, B., Foster, I.S., Airo, A., Van Kranendonk, M.J., Ader, M., and Lalonde, S.V. (2018). Microbial life and biogeochemical cycling on land 3,220 million years ago. Nature Geoscience 11, 1–8. doi:10.1038/s41561-018-0190-9.

Jones III, J.V., Piatak, N., and Bedinger, G.M., (2006). Zirconium and Hafnium: Chapter V of Critical Mineral Resources of the United States – Economic and Environmentl Geology and Prospects for suture supply. *U.S. Department of the interior, US geologic Survey,* Professional Paper 1802-V.

Konhauser, K.O., Planavsky, N.J., Hardisty, D.S., Robbbins, L.J., Warchola, T.J., Haugaard, R., Lalonde, S.V., Partin, C.A., Oonk, P.B.H., Tsikos, H., Lyons, T.J., Bekker, A., Johnson, C.M., (2017). Iron Formations: A global record of Neoarchean to Paleoproterozoic enrironmental history. *Earth-Science Reviews*, 172, 140-177.

Lottermoser, B.G. and Ashley, P.M., (2000). Geochemistry, petrology and origin of Neoproterozoic ironstones in the eastern part of the Adelaide Geosyncline, South Australia. *Precambrian Research*, 101, 49-67.

Merchel, G., Bau, M., Schmidt, K., Münker, C., Dantas, E.L., (2017). Hafnium and neodymium isotopes and REY distribution in the truly dissolved, nanoparticle/colloidal and suspended loads of rivers in the Amazon Basin, Brazil. *Geochemica et Cosmochimica Acta*, 213, 383-399.

Mloszewska, A.M., Pecoits, E., Cates, N.L., Mojzsis, S.J., O'Neil, J., Robbins, L.J., Konhauser, K.O., (2012). The composition of Earth's oldest iron formations: The Nuvvuagittus Supracrustal Belt (Québec, Canada). *Earth and Planetary Science Letters*, 317-318, 331-342.

Moorbath, S., O'Nions, R.K., and Pankhurst, R.J., (1973). Early Archean Age for the Isua Iron Formation, West Greenland. *Nature*, 245, 138-139.

O'Neil, J., Francis, D., Carlson, R.W., (2011). Implications of the Nuvvuagittuq Greenstone Belt for the Formation of Earth's Early Crust. *Journal of Petrology*, 52, 985-1009.

Patterson, C., (1956). Age of meteorites and the earth. *Geochimica et Cosmochimica Acta,* 10, 230-237.

Pettke, T., Lee, D.-C., Halliday, A.N., Rea, D.K., (2002). Radiogenic Hf isotopic compositions of continental eolian dust from Asia, its variability and its implications for seawater Hf. *Earth and Planetary Science Letters*, 202, 453-464.

Piepgras, D.J., and Wasserburg, G.J., (1980). Neodymium Isotpoic Variations in Seawater. *Earth and Planetary Science Letters,* 50, 128-138.

Polat, A. and Frei, R. (2005) The origin of early Archean banded iron formations and continental crust, Isua, southern West Greenland. *Precambrian Research*, 138, 151-175.

Rickli, J., Frank, M. and Halliday, A.N., (2009). The hafnium-neodymium isotopic composition of Atlantic Seawater. *Earth and Planetary Science Letters*, 280, 118-127.

Rickli, J., Frank, M., Stichel, T., Georg, R.B., Vance, D., Halliday, A.N., (2013). Controls on the incongruent release of hafnium during weathering of metamorphic and sedimentary catchments. *Geochimica et Cosmochimica Acta,* 101, 263-284.

Rickli, J., Hindshaw, R.S., Leuthold, J., Wadham, J.L., Burton, K.W., Vance, D., (2017). Impact of glacial activity on the weathering of Hf isotopes – obbservations from Southwest Greenland. *Geochemica et Cosmochimica Acta,* 15, 295-316.

Soyol-Erdene, T.-O., and Huh, Y., (2013). Rare earth element cycling in the pore waters of the Bering Sea Slope (IODP Exp. 323). *Chemical Geology,* 358, 75-89.

Tang, H., Trail, D., Bell, E.A., Harrison, T.M., (2019). Zircon halogen geochemistry: Insigits into Hdean-Archean fluids. *Geochemical Perspectives Letters,* 9, 49-53.

Van de Flierdt, T., Frank, M., Lee, D-C., Halliday, A.H., Reynolds, B.C., Hein, J.R., (2004). New constraints on the sources and behavior of neodymium and hafnium in seawater from Pacific Ocean ferromanganese crusts. *Geochemica et Cosmochimica Acta,* 68, 3827-3843.

Van de Flierdt, T., Goldstein, S.L., Hemming S.R., Roy, M., Frank, M., Halliday, (2007). Global neodymium-hafnium isotope systematics – revisited. *Earth and Planetary Science Letters,* 259, 432-441.

Vervoort, J.D., Patchett, PJ., Blichert-Toft, J., Albarède, F., (1999). Relationships between Lu-Hf and Sm-Nd isotopic systems in the global sedimentary system. *Earth and Planetary Science Letters*, 168, 79-99.

Vervoort, J.D., Plank, T., Prytulak, J., (2011). The Hf-Nd isotopic composition of marine sediments. *Geochemica et Cosmochimica Acta,* 75, 5903-5926.

Viehmann, S., Hoffmann, J.E., Münker, C., and Bau, M., (2014). Decoupled Hf-Nd isotopes in Neoarchean seawater reveal weathering of emerged continents. *Geology*, 42, 115-118.

Viehmann, S., Bau, M., Hoffmann, J.E., Münker, C., (2015). Geochemistry of the Krivoy Rog Banded Iron Formation, Ukraine, and the impact of peak episodes of increased global magmatic activity on the trace element composition of Precambrian seawater. *Precambrian Research,* 270, 165-180.

Viehmann, S., Bau, M., Hoffmann, J.E., Münker, C., (2018). Decoupled Hf and Nd isotopes in suspended particles and in the dissolved load of Late Archean seatater. *Chemical Geology*, 483, 111-118.

White, W.M., Patchett, J., and BenOthman, D., (1986). Hf isotope ratios of marine sediments and Mn nodules: evidence for a mantle source of Hf in seawater. *Earth and Planetary Science Letters*, 79, 46-54.

Zhao, W., Sun, Y., Balsam, W., Lu, H., Liu, L., Chen, J., Ji, J., (2014). Hf-Nd isotopic variability in mineral dust from Chinese and Mongolian deserts: implications for sources and dispersal. *Scientific Reports*, 4, 1-6.

Zimmermann, B., Porcelli, D., Frank, M., Rickli, J., Lee, D.-C., Halliday, A.N., (2009). The Hafnium isotope composition of Pacific Ocean water. *Geochemica et Cosmochemica Acta,* 73, 91-101.

Chapter 2: Materials and Methods

METHODS

2.0 Sample Preparation

Hand samples of all banded iron formations (BIF) were cut with a water-saw to remove obviously weathered outer surfaces, and were re-cut as needed to remove any internal visible weathering rinds, until a fresh-a-sample as possible could be obtained. Samples were then crushed in a pure tungsten-carbide piston (Rockware labs, Golden, CO, USA) and powdered for 10 minutes in an agate ring mill until a uniform, fine-powder was obtained. The tungsten-carbide piston was washed and scrubbed with water twice, then sprayed with ethanol and dried using pressurized air between each sample, while the same procedure was followed for the agate shaker, but with an additional cleaning step wherein pure SiO_2 was powdered for 10 min was carried out between each BIF sample, followed by a second washing and drying of the agate shaker.

2.0.1 Instrumentation: ICP-MS and MC-ICP-MS

Of crucial importance in geochemistry is the ability to accurately and reliably determine what the sample in question is composed of. X-ray based techniques such as X-Ray Fluorescence spectroscopy and X-Ray Diffraction can provide chemical information at different scales, however, the gold standard for determining whole-rock geochemical composition, especially for the Rare Earth Elements (REEs), is Inductively Coupled Plasma Mass Spectrometry (ICP-MS), and a variant permitting high-precision isotope ratio measurements, Multi-collector Inductively Coupled Plasma Mass Spectrometry (MC-ICP-MS).

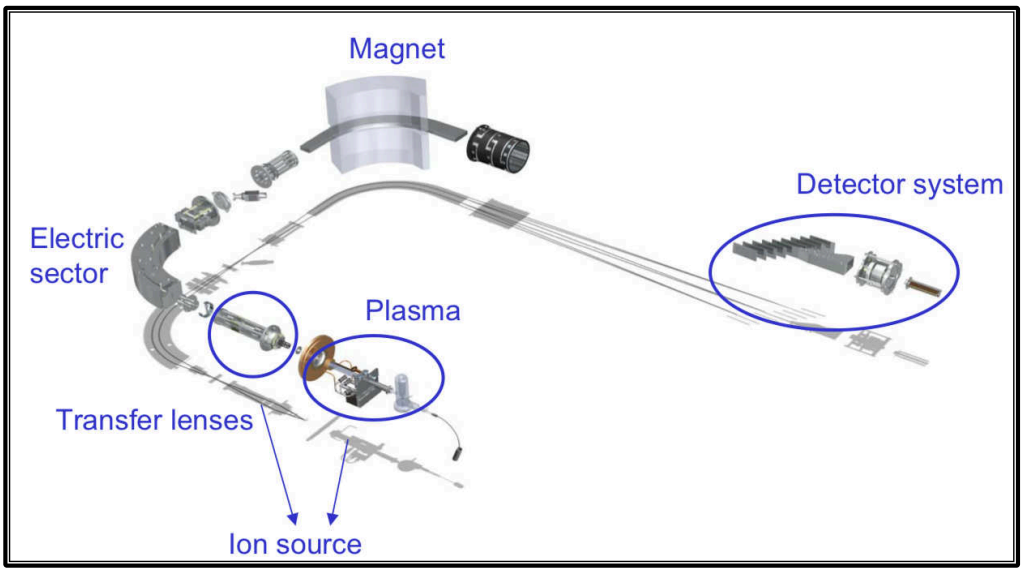

Figure 2.1: Schematic of the NEPTUNE MC-ICP-MC – Samples are introduced at the source (circled plasma) travel through the mass spectrometer, and individual ions are detected by separate faraday cups at the detector.

Both instruments operate similarly with the major difference between them coming at the end of the analysis; where the traditional ICP-MS has a single detector for all elements, the MC-ICP-MS has multiple detectors (faraday cups, with differing sensitivities) that can be moved and tuned to precisely capture elements with very specific masses. In essence, sample material, either as a fine mist (after nebulization) or as an aerosol of fine particles (after laser ablation), is ionized by an argon plasma with a temperature between 6000 and 10000˚K. This plasma decomposes sample atoms for the most part into a fully ionized state (these are almost exclusively positive ions as negative ions do not ionize easily), which is then passed through a series of cone interfaces, each serving as a physical restriction between progressive stages of actively-maintained vacuum, after which the positive ion plasma is then focused into a coherent beam. These ions are focused using electrostatic lenses and accelerated through the

mass spectrometer using a voltage gradient, during which they are separated by their mass-to-charge ratio by passing a large magnet and detected as charge "counts" for each mass at the detector, or detectors. Detector counts can then be processed to determine the raw number of counts for an element with a certain mass and charge (Figure 2.1), which can then be converted into total elemental abundance according to known element ratios, or in the case of elements that experience radioactive decay, can be used to determine the sift from natural ratios due to the accumulation of radioactive daughter products, such as the decay of ^{176}Lu into ^{176}Hf.

2.1 Analysis of the εHf-εNd system

For analysis of the εHf-εNd system it is imperative to chemically isolate both elements, separating them from all other isotopes or compounds that can cause interference on the same mass (isobars), as well as those elements that have mother-daughter decay products that result in the production of an isotope of interest. Specifically, the elements of concern for this study are Neodymium (Nd), Samarium (Sm), Ytterbium (Yb), Lutetium (Lu), and Hafnium (Hf). The procedures for separating them chemically and correcting for mass interferences is covered in detail in this chapter, as is the digestion and analysis protocol for the determination of major and trace element concentrations in Banded Iron Formations (BIF).

Isotope	Mass (Da)	Natural Abundance (%)	Interference	Daughter product
^{136}Ce	135.907140	0.19		
^{138}Ce	137.905985	0.25		
^{140}Ce	139.905433	88.45		
^{142}Ce	141.909241	11.11	^{142}Nd	
^{142}Nd	141.907719	27.20	^{142}Ce	
^{143}Nd	**142.909810**	**12.20**		
^{144}Nd	**143.910083**	**23.80**	**^{144}Sm**	**^{140}Ce**
^{145}Nd	144.912570	8.30		
^{146}Nd	145.913113	17.20		
^{148}Nd	147.916889	5.70		
^{150}Nd	149.920887	5.60		^{150}Sm
^{144}Sm	143.911998	3.07		
^{147}Sm	**146.914894**	**14.99**		**^{143}Nd**
^{148}Sm	147.914819	11.24		^{144}Nd
^{149}Sm	148.917180	13.82		
^{150}Sm	149.917273	7.38		
^{152}Sm	151.919728	26.75		
^{154}Sm	153.922205	22.75		
^{168}Yb	167.933894	0.13		
^{170}Yb	169.934759	3.04		
^{171}Yb	170.936323	14.28		
^{172}Yb	171.936378	21.83		
^{173}Yb	172.938208	16.13		
^{174}Yb	173.938859	31.83		
^{176}Yb	**175.942564**	**12.76**	**^{176}Lu and ^{176}Hf**	
^{175}Lu	174.94077	97.41		
^{176}Lu	**175.942679**	**2.59**	**^{176}Yb and ^{176}Hf**	**^{176}Hf**
^{174}Hf	173.940044	0.16		^{170}Yb
^{176}Hf	**175.941406**	**5.26**	**^{176}Yb and ^{176}Lu**	
^{177}Hf	**176.943217**	**18.60**		
^{178}Hf	177.943696	27.28		
^{179}Hf	178.945812	13.62		
^{180}Hf	179.946546	35.08		

Table 2.1: Isotopes of Interest, natural abundance, mass interferences and mother-daughter products, for the elements of interest in this study.

2.2 Methodology of Cation Exchange Column Chromatography

Cation exchange chromatography is physical process by which different elements can be separated from each other by passing them through columns containing various types of resin whose surface has been functionalized with organic or inorganic reactive functional groups. Based on the ligand type and the size of the resin grains, different elements will have different affinities for the resin, and by manipulating the matrix containing the elements (i.e. the fluids flowing through the columns), different resins can be calibrated to bind and then elute (release) different elements using different volumes or concentrations of acids. For this study several types of resin will be used that rely on all aspects of resin geometry including resin type, resin grainsize, solute concentration, solute type (HCl, vs HNO_3 vs HF) and elution time. Below are descriptions of the elements that are critical to separate for this study, and how each separation was achieved.

2.3 Neodymium (Nd)

Measurement of εNd requires the elemental ratio of $^{143}Nd/^{144}Nd$, thus, the only mass interference of concern for this system is ^{144}Sm (Table 2.1), this requires the geochemical separation of Nd from Sm by column geochemistry. This procedure will be discussed in detail in the latter section detailing separation and measurement of Lu (Sections 2.5.3D, 2.5.3E and 2.5.4D, 2.5.4E).

2.3.1 Calculation of εNd@ time = t

^{143}Nd is also a decay product of ^{147}Sm, therefor the calculation of $\varepsilon Nd_{(t)}$ (t = time of formation) requires a correction for the decay of ^{147}Sm into ^{143}Nd over time.

This correction can be achieved by utilizing the equations and decay constants as described below.

Concentration of $^{147}Sm/^{144}Nd$ in a sample:

$$\frac{^{147}Sm}{^{144}Nd} = \left(\frac{Sm}{Nd}\right)_{Total\ concentration} * 0.602$$

Modeled age of Sample from CHUR:

$$t = \frac{1}{\boldsymbol{\lambda}} ln\left[\frac{(^{143}Nd/^{144}Nd)^{0}_{sample} - 0.512638}{(^{147}Sm/^{144}Nd)^{0}_{sample} - 0.1967} + 1\right]$$

λ = decay constant of Sm = 6.54 E^{-12}

$^{143}Nd/^{144}Nd_{sample}$ at a given time "t":

$$\left(\frac{^{143}Nd}{^{144}Nd}\right)^{t}_{Sample} = \left(\frac{^{143}Nd}{^{144}Nd}\right)^{0}_{Measured} - \left(\frac{^{147}Sm}{^{144}Nd}\right)^{0}_{Measured} * \left(e^{\lambda t} - 1\right)$$

λ = decay constant of Sm = 6.54 E^{-12}

t = age of rock formation

0 = denotes the modern date of measurement

εNd at the time of formation:

$$\boldsymbol{\varepsilon}(Nd)_{(t)} = \left[\frac{(^{143}Nd/^{144}Nd)^{t}_{sample}}{(^{143}Nd/^{144}Nd)^{t}_{CHUR}} - 1\right] * 10^{4}$$

$$\left(\frac{^{143}Nd}{^{144}Nd}\right)^{t}_{CHUR} = 0.512638 - 0.1967 * \left(e^{\lambda t} - 1\right)$$

λ = decay constant of Sm = 6.54 E^{-12} t = age of rock formation

2.4 Samarium (Sm)

The importance of Sm to the εHf-εNd system is simply the interference between ^{144}Sm and ^{144}Nd, and the decay of ^{147}Sm into ^{143}Nd over time, as discussed above (Table

2.1). Correction for decay of ^{147}Sm into ^{143}Nd is covered in the equations listed above (section 2.3.1), and geochemical separation of these elements will be discussed in detail with the procedure for Lu separation below (Section 2.5.3D, 2.5.3E and 2.5.4D, 2.5.4E).

2.4.1 Ytterbium (Yb)

Only the heaviest isotope of Ytterbium, ^{176}Yb, causes concern for analysis of εHf-εNd, as it presents an isobaric interference with both ^{176}Lu and ^{176}Hf. Thus it must be chemically separated from both elements and corrected for at the time of measurement. Geochemical separation of this element will be discussed in the following section discussing the geochemistry and separation of Lu (Section 2.5.3D, 2.5.3E and 2.5.4D, 2.5.4E).

2.5 Lutetium (Lu)

The geochemical separation and isolation of Lu from both Yb and Hf is critical for analysis of the εHf-εNd system, as not only does it experience mass interference from both ^{176}Yb and ^{176}Hf, it also decays into ^{176}Hf, and thus must be accounted for when determining $\varepsilon Hf_{(t)}$ at the time of formation. The following discussion will cover the initial digestion of BIF samples, the initial separation of Lu and REE from Hf, and the calibration/procedural use of new columns for a 2-column setup for the purification of Nd, Sm, Yb and Lu. The following sections have been written in a procedural (instructional) format for brevity and to facilitate employment by future workers.

2.5.1 Digestion of BIF Samples and Separation Of Hf From Lu and REE

Bulk Sample Digestion and Fluoride Crystal Formation

Sample digestion begins by weighing an appropriate amount of sample material into a 15 mL Teflon beaker, between 0.5 to 2 g of BIF depending on the concentration of Hf and Lu in the each BIF (predetermination of concentrations can be performed using ICP-MS) to ensure measurable yields at the spectrometer between 10's to 200 ppb per element of interest. Next add three drops of HNO_3 to each beaker, then fill the beaker to the 2/3 mark with picotrace HF. Place beakers overnight on a hotplate at 110˚C, remove the beakers the next day and sonicate them for 1 hour, then place on the hotplate again overnight. The next day, removed beakers from the hotplate and allow them to cool to room temperature, then open them, and place back on the hotplate at 80˚C until they are dry. Again remove beakers from the hotplate and allow to cool to room temperature, then fill each one with 3.5 mL of picotrace HF, re-seal them, and place them on a hotplate at 90˚C for at least 2-3 days to form fluoride salts. As before, sonicate them after the first night on the hotplate. (Practical procedure provided below).

Bulk Sample Digestion and Fluoride Crystal Formation

Reagents

Picotrace Purity HF

14.4 M HNO_3

Procedure

☐ 1. Select 15 mL Teflon Savillex beakers and label them appropriately

☐ 2. Weigh sample material into each beaker and record weight (~1 g for BIF's)

☐ 3. Add six drops of HNO_3 to each beaker

☐ 4. Fill each beaker to ⅔ with HF

☐ 5. Place beakers on a hotplate @ 110˚C overnight

☐ 6. Remove beakers and Sonicate for 1 hour, place back on hotplate overnight

☐ 7. Remove beakers from hotplate and allow cooling to room temperature

☐ 8. Open beakers and evaporate contents to dryness on hotplate @ 80 ˚C

☐ 9. Remove beakers from hotplate and allow contents to cool to room temperature.

☐ 10. Add 3.5 mL of picotrace HF to beakers and re-seal them.

☐ 11. Allow beakers to sit for at least 2-3 days @ 90˚C to form Fluoride-salts.

a. Sonicate beakers for 2 hours after the first day to break up initial salts.

2.5.2 Separation Of Hf-Supernatant And Fluoride Crystals

Remove beakers containing fluoride crystals and HF from the hotplate after 3 days and allow them to cool to room temperature, then sonicate all beakers to helps breaks up fluorides. Label pre-cleaned (ie. Materials that have been washed for 2-3 nights with 6N HCl, then rinsed with ultra-pure H_2O and dried) centrifuge tubes and caps for each sample, and setup both Teflon beakers and centrifuge tubes near the centrifuge. Shake the Teflon containiners, and tap them on the table to get remove the Hf droplits from the inside of the lid, and carefully pour the contents of each Teflon beaker into the corresponding centrifuge tube, ensuring you get all possible drops of liquid into the tube (some solids may remain if they are stuck or the crystals have grown to large). After each centrifuge tube has been filled, cap it and place it in the centrifuge, and carefully set the Teflon beaker aside. After all Teflon beakers have been emptied into the centrifuge tubes, turn the centrifuge on for 2-3 min @ 5000 rpm. While centrifuging label new 15 mL Teflon beakers for each sample. When the centrifuge is finished very carefully pour the supernatant (liquid) from each tube into its NEW clean Teflon beaker, be careful not to get ANY of the solid material into this new beaker.

Once the supernatant is in the new beaker rinse any material remaining in the centrifuge tube back into its ORIGINAL container using 6N HCl, then fill the beaker to ~3/4 full of 6N HCl and store until ready for purification of Nd, Sm and Lu cuts. Finally, place the new Teflon beakers with the HF supernatant uncapped on a hotplate overnight to dry at 80˚C. (Practical procedure provided below).

Separation Of Hf-Supernatant And Fluoride Crystals

Centrifugation of HF from Fluorides

Reagents

Supernatant Beakers for Hf

5 mL Centrifuge Tubes and Caps

Procedure

☐ 1. Sonicate mixture for 10 min

☐ 2. Prepare new beakers and centrifuge tubes by labeling them for the supernatant

☐ 3. After sonication, tap each container to get droplets off the lid

☐ 4. Pour entire contents of beaker into centrifuge tube if possible (should be ~3.5 mL)

   a. Get all the material in (if all crystals don't fit, leave them in the beaker)

   b. Try not to spill fluid or lose crystals

   c. Tap container a lot to get crystal-gel into a "pourable" size

   d. Cap the centrifuge tubes

☐ 5. Place samples in centrifuge for 3-5 min @ 5000 rpm

   a. Make sure centrifuge is balanced

☐ 6. Pour supernatant from each tube carefully into the corresponding new Hf beaker

a. Don't get any solids, you may have to centrifuge twice

☐ 7. Partially fill centrifuge tube with 6 N HCl if continuing immediately, and agitate (spin) the tube to loosen solids, then pour solids back into their original beaker

a. Repeat until all solids are in beaker, fill beaker with 6N HCl, cap and place on a hotplate over night to re-dissolve.

☐ 8. Place Hf supernatant beakers, uncapped, in fume hood over night at 80˚C to dry.

2.5.3 Calibration of Column 1 for Lu, Yb, Nd, Sm Separation

Separation of these 4 elements was achieved using a BIORAD column filled with 2mL AG50-X8 200-400 mesh resin. The initial calibration was carried out as follows:

2.5.3A Calibrating Nd-Sm-Lu Column #1

2 mL AG50-X8 200-400 mesh in BIORAD Columns

Preparing Standard Solutions

Create standards for the elements of interest, i.e. for Ce, Nd, Sm, Yb, Lu.

1) Pour each standard solution into its cap and pipette from that so you don't contaminate the rest of the solution. Pour any remainder down the drain not back in the solution container
2) Make 3 mL of each solution for calibration, use 0.3 mL each elemental standard, and 2.7 mL of μH_2O to produce an ~ 100 ppm solution
3) Dry the solution inside a clean beaker until no liquid is left
4) Add 3 mL of 2.5 M HCl to each beaker to re-suspend each element
5) Test 1 mL of each spike solution to make sure the colour change as follows:

A) Place 1 mL spike solution into a clean plastic container

B) For solutions suspended in acid stronger then 0.6 N (in our case 2.5 M HCl) you must dry the solution then resuspend in 1 mL 0.3 N HCl
C) Add one drop “Eriochrom Black T” to each solution
D) Add six drops Ammonia to each container
E) Mix, solutions should turn red if REE’s are present at pH 10, often need to leave overnight for the colour to develop.

2.5.3B Rough Column Calibration

1) Begin by conditioning columns with 2 mL of 2.5 M HCl
2) Place labeled collection cups under each column
3) Add 1 mL of each standard solution onto the corresponding column (one element type per column)
4) Collect each mL of liquid as it comes out of the column, dry down sample, add 1 ml 0.3 N HCl, 6 drops Ammonia, 1 mL water and test with one drop Eriochrom Black.
5) Keep adding 1 mL of 2.5 M HCl until the Lu and Yb columns have changed to red, then back to blue.
6) Switch and add 1 mL 4 M HNO_3 to remaining columns proceeding as before until Nd and Sm columns have changed to red, then back to blue.
7) Clean columns by passing 2 mL μH_2O, followed by 10 mL 6 M HCl, qnd restock them in 2.5 N HCl.

See Figure 2.2 for results:

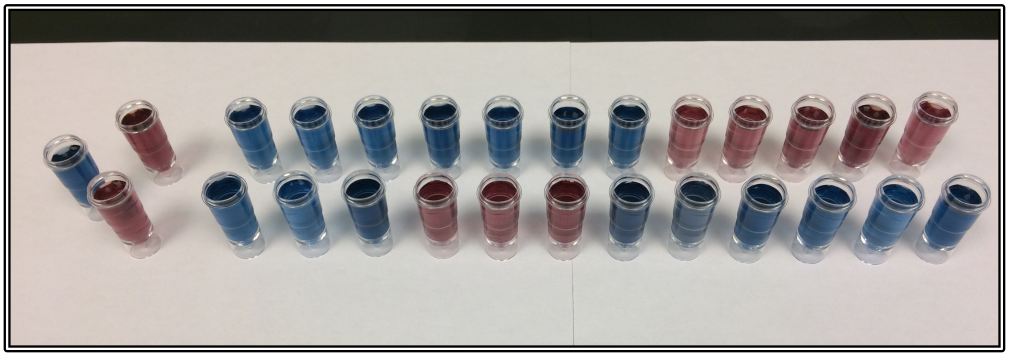

Figure 2.2: Results for an approximate calibration of AG50-X8 using Eichrom black. Top row contains Nd/Sm and bottom row contains Lu/Yb.

2.5.3C Final Column Calibration with ICP-MS

1. Create a stock solution of a Geo-standard (in this case BHVO-2) to use on each column you test containing a mix of.
2. Create a 10 ppb standard of Ce, Nd, Sm, Yb and Lu for analysis.
3. Using the elution volumes from the rough calibration prepare a protocol that will collect the 1 mL fractions that showed positive results, as well as the mL before and after them to test for co-elution with other unwanted elements.
4. Collect each mL individually from 2-4 columns (increases accuracy and gives better idea of variation between columns), then evaporate aliquots to dryness
5. Resuspend each mL in 3 mL of 2.5% Nitric Acid and add a 1 ppb of Indium (In is an internal standard), these solutions are stable for long periods of time at this point if stored in sealed containers, or can be placed directly into ICP-MS tubes for analysis.
6. Load samples into ICP-MS trays, remembering to include your 10 ppm standards, 2.5% Nitric blanks, and an μH_2O blank.
7. Analyze samples for any elements of concern present in your standard solution and create elution curves.

8. Prepare an elution protocol that captures the elements you want and avoids those you don't using the data from your calibrated columns.
9. Repeat calibrated protocol with the remained of your stock BHVO-2 and IFG solutions to perfect the elution curves with further ICP-MS measurement runs. Our final elution curve results can be found in figure 2.3, with the protocol in the following section.

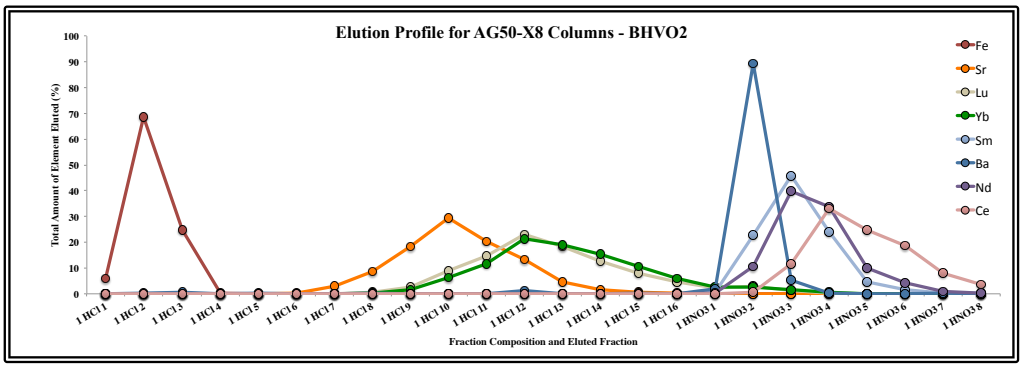

Figure 2.3: Elution profile using BHVO-2 for BIORAD columns with 2mL AG50-X8 200-400 mesh, for collection of Lu, Yb, Nd and Sm, highlighting the elution timing for elements of interest and their potential interferences.

2.5.3D Lu-Yb-Nd-Sm Separation Procedure For BIORAD Columns

Take each sample containing fluoride crystals and 6N HCl from the previous centrifuge step and place them on a hotplate overnight at 110˚C. The next day allow the samples to cool to room temperature, then open them and evaporate to dryness at 80˚C. Once dry, resuspend each sample in 1 mL 2.5 N HCl, close cap, and heat to 80˚C overnight (Practical procedure provided below).

Lu-Yb-Nd-Sm Separation Procedure For BIORAD Columns With 2ML AG50-X8 200-400 mesh

Fluoride Crystal Sample Digestion

Reagents

6 M HCl

2.5 M HCl

Procedure

☐ 1. Begin with the remnant, solid/gel filled beakers filled with 6N HCl from the Hf centrifuge step described in section 2.5.2

☐ 2. If not done previously**,** place beakers on a hotplate overnight @ 110 ˚C

☐ 3. The next day, evaporate sample to dryness at 100 ˚C or, overnight at 80 ˚C

☐ 4. Resuspend samples in 1 mL 2.5 N HCl, and heat to 80 ˚C overnight.

2.5.3E Separation of REE From Bulk Elements and Iron

Remove samples from hotplate and allow them to cool to room temperature while simultaneously draining a corresponding cation-exchange column containing *AG50-X8 200-400 mesh*. Once all columns have drained completely into a discard dish, condition each column with 2 mL of 2.5 N HCl. Once the columns have drained again shake each corresponding Teflon beaker containing your 1 mL sample, tap the Teflon to ensure all droplets fall off the lid, then carefully open each beaker, and add the 1 mL sample to its corresponding column. Using a new, clean, pipette tip for each sample repeat this for all samples. Once the samples have fully entered the column, and using a new tip, rinse each sample into the column further by adding 1 mL 2.5 N HCl, repeat this twice more. Once all columns have stopped emptied add 7 ml 2.5N HCl, and proceed to rinse your initial Teflon beakers and lids three times each with ultra-pure H_2O. Once the columns are empty, place the rinsed beaker under the corresponding column and add 7 more ml 2.5N HCl to capture your Sr, Yb and Lu cut. Once all

columns are empty remove your collection beakers, and replace the discard dishes and add 3 mL 4 N HNO_3. Once all the columns are dry place the corresponding collection beakers under the columns again and add 5 mL 4 N HNO_3 to capture the Ce, Nd, and Sm fractions, proceed to dry all beakers overnight at 80˚C, can clean each column by passing 2 mL ultra-pure H_2O, then 10 mL 6 N HCl, and final 2 mL 2.5 N HCl through them, and stocking them in 2.5N HCl. (Practical procedure provided below).

Separation Of REE From Bulk Elements and Iron

Reagents

Small Biorad Columns filled with AG50-X8 200-400 mesh

Collection Beakers

2.5 N HCl

6 N HCl

4 N HNO_3

Procedure

- ☐ 1. Open columns and allow them to drain completely
- ☐ 2. Condition columns by adding 2 mL 2.5 M HCl
- ☐ 3. Load 1 mL sample (in 2.5 M HCl) onto each column
- ☐ 4. Rinse sample onto columns with 1 mL 2.5 N HCl
    - ☐ a. Repeat 1 mL rinse-2
    - ☐ b. Repeat 1 mL rinse-3
- ☐ 5. Add 7 mL 2.5 N HCl to wash out Rb,Ca, K
- ☐ 6. Rinse collection beakers 3 times with µH_2O if reusing from first step
- ☐ 7. Add 7 mL 2.5 N HCl to capture Sr, Yb and Lu and collect!
- ☐ 8. Remove collection beakers, change acid, and add 3 mL 4 N HNO_3

☐ 9. Replace collection beakers

☐ 10. Add 5 mL of 4 N HNO_3 to collect Ce, Nd and Sm.

11. Dry contents of collection beakers completes overnight @ 90 ˚C

12. **NOTE: If the elution appears reddish, orange, or yellowish re-evaporate, and re-suspend in 1 mL 2.5 N HCl, and run through columns again.

☐ 13. Rinse columns with 2 mL UP-H_2O

☐ 14. Wash columns twice with 5 mL of 6 N HCl.

☐ 15. Re-condition columns with 1 ml 2.5 N HCl, then cap and store columns with 2 mL of 2.5 N HCl.

For procedural outline refer to Figure 2.4.

Nd-Sm-Lu Column #1 - Biorad AG50X8 Cl 200-400 mesh (4cm * 0.8cm)														
Step	Eluent	Volume	Completed ✓											
Condition Column	2.5 N HCl	2 mL												
Load sample	2.5 N HCl	1 mL												
1st Rinse	2.5 N HCl	1 mL												
2nd Rinse	2.5 N HCl	1 mL												
Discard - Rb, Ca, K	2.5 N HCl	7 mL												
Collect - Sr, Lu, Yb	2.5 N HCl	7 mL												
Discard - Ba	4 N HNO_3	3 mL												
Collect - Sm, Nd, Ce	4 N HNO_3	5 mL												
Clean	H_20	2 mL												
Clean	6 N HCl	5 mL												
Clean	6 N HCl	5 mL												
Stock	2.5 N HCl	2 mL												

Figure 2.4: Elution protocol for obtaining Lu, Yb, Nd and Sm, on an AG50-X8 column.

2.5.4 *Calibration of Column #2 for Isolation of pure Lu, Yb, Nd, Sm Samples*

As discussed above, ultimate determination of $^{143}Nd/^{144}Nd$ ratios, as well as precise determination of Lu concentration in each sample, we require the complete separation of Nd from Sm, and Yb from Lu. Initial calibrations were accomplished in a similar manner as above, however the resin and column configurations were changed to 2 mL LN-SPEC 50-100 µm resin in thin (0.8 cm x 8 cm) glass columns for better separation of elements. The calibration procedure is outlined below.

2.5.4A Calibrating Nd-Sm-Lu-Yb Column #2

2 mL LN-SPEC 50-100 µm in (0.8cm x 8 cm) Glass Columns

Preparing Standard Solutions

Begin by creating standards that mimic your natural sample concentrations, i.e. for Ce, Nd, Sm, Yb, Lu ~ 100 ppb, and follow the outline as laid out in section 2.5.3A.

2.5.4B Rough Column Calibration

1. Begin by conditioning columns with 3 mL of 0.3 M HCl
2. Place labeled collection cups under each column
3. Add 1 mL of each standard solution to the corresponding column (one element type per column)
4. Collect each mL of liquid as it comes out of the column, add corresponding amount of Ammonia and water and test with Eriochrom Black
5. Keep adding 1 mL of 0.3 N HCl until the Ce and Nd columns have changed to red, then back to blue.
6. Switch and add 1 mL 0.6 N HCl to remaining columns proceeding as before until Sm columns have changed to red, then back to blue.
7. Switch and add 1 mL 4 N HCl to remaining columns proceeding as before until Yb and Lu columns have changed to red, then back to blue (note these take a long time to develop and will appear only faintly purple for several hours).
8. Clean columns by passing 10 mL 6 M HCl through them twice.

See Figure 2.5 for overnight results, prior to overnight colour development.

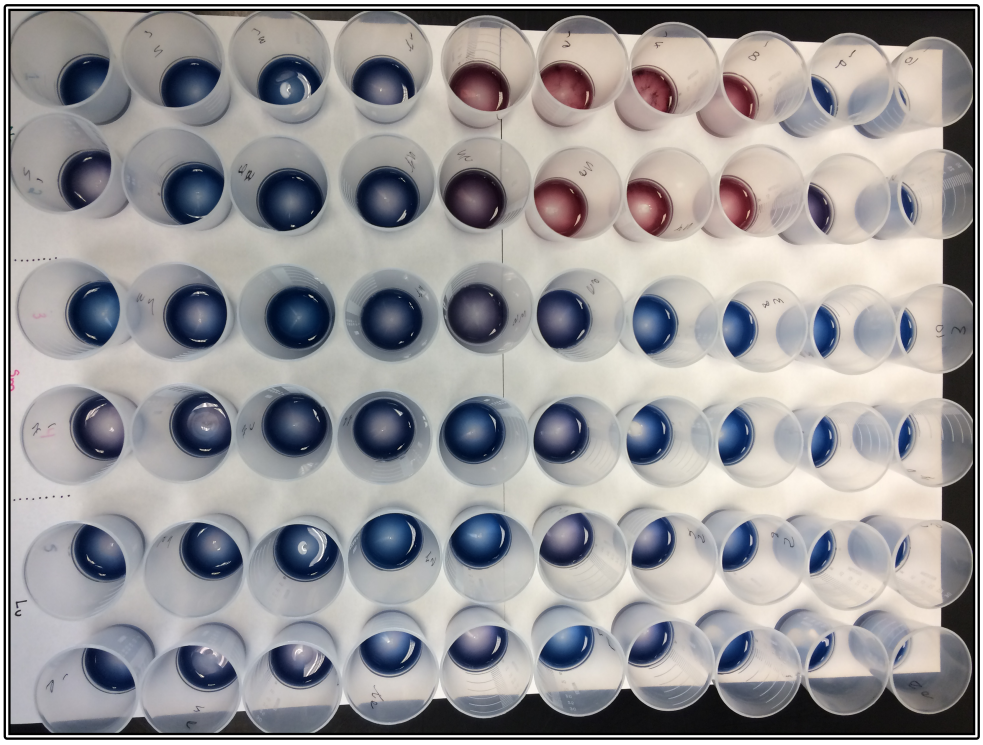

Figure 2.5: Example results of Ln-Spec column calibration using Eiochrom black. Top two rows are Nd, the middle two are Sm, and the bottom 2 are Lu.

2.5.4C Final Column Calibration with ICP-MS

1) Create a standard solution of 50 ppb to use on each column you test containing Ce, Nd, Sm, Yb and Lu.
2) Dilute from this a 10 ppb standard for analysis.
3) Using the elution volumes from the rough calibration prepare a protocol that will collect the 1 mL fractions that showed positive results, as well as the mL before and after them to test for co-elution with other unwanted elements.

4) Collect each mL individually from 2-4 columns (increases accuracy and gives better idea of variation between columns), then evaporate aliquots to dryness

5) Resuspend each mL in 3 mL of 2.5% Nitric acid and add a 1 ppb of Indium (In is an internal standard), these solutions are stable for long periods of time at this point if stored in sealed containers, or resuspend directly into ICP-MS tubes for analysis.
6) Load samples into ICP-MS trays, remembering to include the 10 ppm standards, 2.5% Nitric Blanks and an UP-H_2O blank.
7) Analyze samples for any elements present in your standard solution and create elution curves.
8) Prepare an elution protocol that captures the elements you want and avoids those you don't using the data from your calibrated columns.
9) Repeat calibrated protocol with a real sample standard like BHVO-2 and IFG that have been prepared for ICP-MS calibrations.

Results of this elution procedure can be seen in Figure 2.6, and the procedure follows:

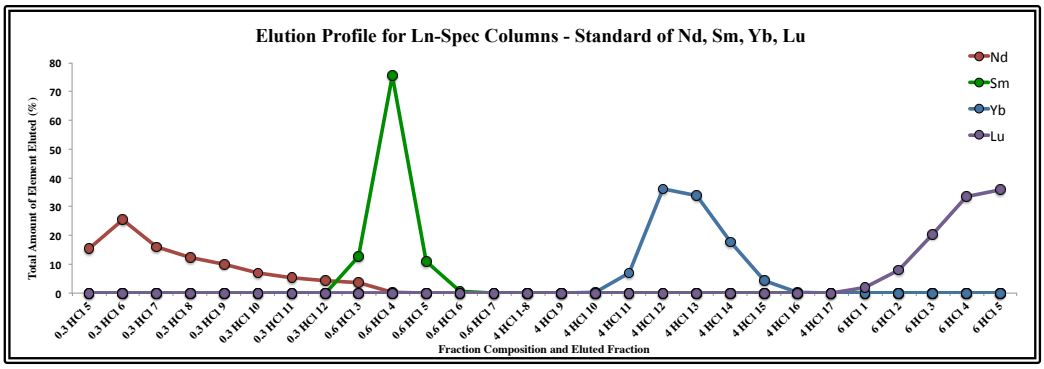

Figure 2.6: Elution profile for BHVO2 on an Ln-Spec column, highlighting the elution timing for the elements of interest Nd, Sm, Yb and Lu.

2.5.4D Preparation For Separation of Nd-Sm-Yb-Lu

Evaporate the samples from the prefious column if you have not already done so, then resuspend them in 0.3 N HCl overnight @ 80˚C. Repeat this once.

Preparation For Separation of Nd-Sm-Yb-Lu

Reagents

0.3 M HCl

Procedure

☐ 1. Evaporate mixed Nd,Sm,Yb,Lu samples (obtained in section 2.5.3E) to dryness to remove HNO_3 from previous column

☐ 2. Resuspend sample with 2 mL 0.3 N HCl and allow to equilibrate overnight.

☐ 3. Resuspend sample with 1 mL 0.3 N HCl and allow to equilibrate overnight.

2.5.4E Final Separation of Nd-Sm-Yb-Lu

Drain all columns into drainage dishes while sample removing samples from hotplate and allowing them to reach room temperature. Condition each column containing *2 mL Eichrom Ln-Spec 50-100 mesh* with 2 mL of 0.3 N HCl, then load each 1 mL sample onto its corresponding column once the condition step has dried. Rinse each sample into the column with 3 mL 0.3 N HCl, and label 15 ml Teflon beakers for each Nd sample. Once all columns have drained place the corresponding Teflon under each column, then elute Nd with 8 mL 0.3 N HCl. Remove samples and place on a hotplate to dry overnight at 80˚C. Place column back over drainage dishes and add 3 mL 0.6 N HCl, while labeling new 7 mL Teflon beakers for Sm. Once the rise has drained place collection beakers under the columns and add 2 ml 0.6 N HCl, then place on the hotplate. Place beakers over the drainage dishes and 8 x 2 mL of 4 N HCl (for a total of 16 mL) to rinse Yb, and label 7 mL Teflon beakers for the collection of Lu. Once all columns have drained completely place the columns over the collection beakers and add 7 mL of 6 N HCl, then place on a hotplate to dry once all the elutant has passed through the columns. Clean the columns by filling them entirely twice with 6 N HCl, then rinsing once with 2 mL 0.3 N HCl, and once drained, store them in 0.3

N HCl, NOTE don't ever let these columns get dry. (Practical procedure provided below).

Final Separation of Nd-Sm-Yb-Lu

2 mL LN-SPEC 50-100 µm in (0.8cm x 8 cm) Glass Columns

Reagents

Long quartz columns filled with 2 mL Eichrom Ln-Spec 50-100 mesh

Collection Beakers for 3 different element cuts Nd, Sm and Lu

0.3 N HCl

0.6 N HCl

4 N HCl

6 N HCl

Procedure

☐ 1. Drain columns (stocked in 2 mL 0.3 N HCl)

☐ 2. Condition columns with 2 mL 0.3 N HCl

☐ 3. Load sample (suspended in 0.3 N HCl) carefully onto resin

☐ 4. Rinse column with 3 mL 0.3 N HCl to get sample into resin

☐ 5. Place collection cups for Nd under each column, and elute with 8 mL 0.3 N HCl

☐ 6. Remove collection cups, and rinse with 3 mL 0.6 N HCl

☐ 7. Place collection cups for Sm, and elute with 2 mL 0.6 N HCl

☐ 8. Remove collections cups, and rinse Yb with 16 mL 4 N HCl

☐ 9. Place collections cups for Lu, and elute with 5 mL 6 N HCl

☐ 10. Place all samples to dry overnight

☐ 11. Wash columns twice with 10 mL 6 N HCl, and stock with 2 mL 0.3 N HCl.

For protocol overview see Figure 2.7, and Figure 2.8 for column geometry and use.

Nd-Sm-Lu Column #2 - Eichrom Ln-Spec 50-100 2 mL in Long Columns														
Step	**Eluent**	**Volume**	**Completed ✓**											
Condition Column	0.30 N HCl	2 mL												
Load sample	0.30 N HCl	1 mL												
Rinse	0.30 N HCl	3 mL												
Collect - Nd	0.30 N HCl	8 mL												
Rinse	0.60 N HCl	3 mL												
Collect - Sm	0.60 N HCl	2 mL												
Wash - Yb	4 N HCl	16 mL												
Collect - Lu	6 N HCl	6 mL												
Clean	6 M HCl	10 mL												
Clean	6 M HCl	10 mL												
Stock	0.3 M HCl	2 mL												

Figure 2.7: Elution profile for complete separation of Nd, Sm, and Lu for isotopic analysis.

2.6 Hafnium (Hf)

For the εHf-εNd system the ration we are interested in measuring is $^{176}Hf/^{177}Hf$, and similarly to $^{143}Nd/^{144}Nd$ this ratio suffers from both mass interferences on ^{176}Hf from both ^{176}Lu and ^{176}Yb, as well as the fact that ^{176}Hf is a daughter product from the decay of ^{176}Lu. Thus separation of Hf from both Lu and Yb is of utmost importance for this element. The separation protocol used in this study is modeled after Blichert-Toft et al. (1997) and requires a 2-column separation procedure as outlined below to prepare a sample of pure Hf and Zr for analysis on an MC-ICP-MS.

As the initial digestion of the samples, as well as centrifugation of the Hf containing supernatant from the Lu-containing fluoride crystals has already been discussed in sections 2.5.1 and 2.5.2, thus, this section will begin immediately with the procedures for the 2-column separation of Hf on Column #1 and Column#2.

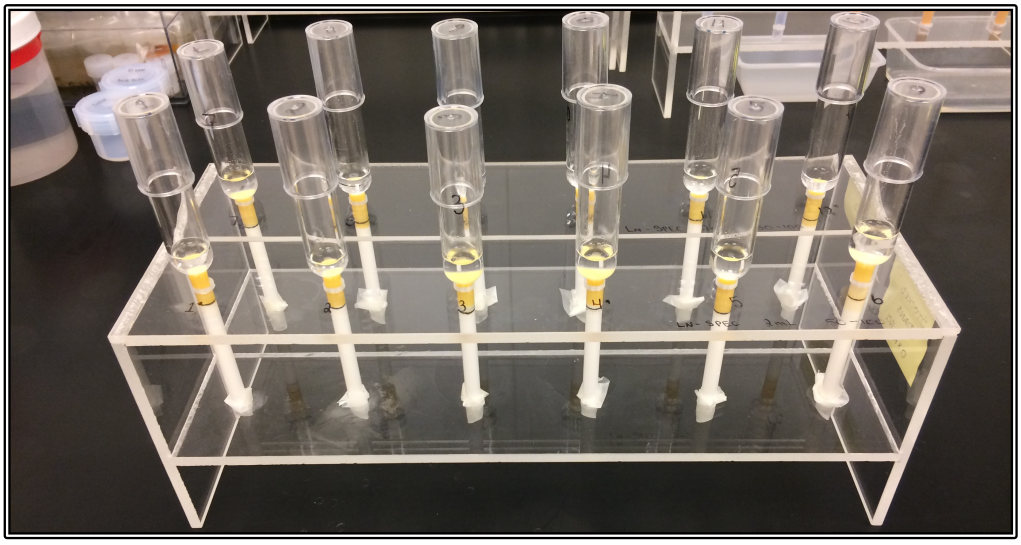

Figure 2.8: Prepared Ln-Spec columns prepared and conditioned in 0.3 N HCl ready for use as described in the protocol above.

2.6.1 Preparation For Column #1

After the supernatant from the centrifugation step has dried it must be resuspended in order to proceed. Depending on the amount of initial sample you digested the first step will vary, but add 1 mL of (0.5 M HCl + 0.5 M HF) for every 500 g of sample dissolved, cap the sample and allow 3-6 hours for it to dissolve, not full dissolution does not always occur, then dry the sample overnight. The following day evaporate your sample to dryness at 90˚C, then add 1 mL of (0.5 M HCl + 0.5 M HF) to each sample, cap it, and place it on a hotplate overnight at 90˚C. (Practical procedure provided below).

Preparation For Column #1

Reagents

Acid Solution O.5 M HCl + 0.5 M HF = (18 mL $HF_{Picotrace}$, 84 mL 6 N HCl, 900 mL μH_2O)

Procedure

☐ 1. Redissolve Hf-supernatant residue with 1 mL solution (0.5 M HCl + 0.5 M HF)

   a. Add 1 mL for every 500 mg initial sample dissolved

   b. Cap and leave solution on hot plate for ~ 3-6 h

   c. Evaporate solution to dryness.

☐ 2. Redissolve residue again with 1 mL solution (O.5 M HCl + 0.5 M HF)

   a. Place on hotplate @ 90˚C overnight

   b. Cool and store the solution as is, until ready to proceed to the next steps.

2.6.2 Hafnium Ion-Exchange Column #1

Begin by draining a Biorad column filled with *10 mL of AG1-X8 100-200 mesh* for each Hf supernatant sample dried and redissolved as above. Label a small, clean (1.5 mL) centrifuge tube for each sample and load the corresponding sample into it. Centrifuge all samples for 3 min at 8000 rpm, while simultaneously draining the Biorad columns into discard trays, then conditioning them with *0.5 M HCl + 0.5 M HF*. Once columns have drained, carefully load each column with its corresponding sample using a new 1 mL pipette for each sample and be careful not to get any "gels" from the bottom of the centrifuge tube onto the column. Load the first and second 1 mL rinse of *0.5 M HCl + 0.5 M HF* onto the columns, allowing them to empty completely before continuing, then add 8 mL *0.5 M HCl + 0.5 M HF* to each column. While the columns drain rinse the initial Teflon beakers and lids three times each with ultra-pure H_2O, and label relabel them if the labels have worn off. Once the columns are empty fill them again with 10 mL *0.5 M HCl + 0.5 M HF* and allow them to empty completely. Finally, once the columns are dry again, place the columns under the Teflon collections beakers and add 6 mL 6N HCl to capture the Hf. Once the columns have drained, add 10 drops

perchloric acid ($HClO_4$) to each beaker containing the Hf elutant, and place on a hotplate at 80˚C overnight. Finally, place the columns back over the draining dishes and clean them by first filling them with 24 N Hf, allowing this to completely empty, then followed by two cycles of filling the columns with ultra-pure H_2O, then approximately 6 N HCl. Finally, finally half-fill the columns with ultra-pure H_2O and store for later use. (Practical procedure provided below).

Hafnium Ion-Exchange Column #1

Reagents

BioRad Column – 10 mL of AG1-X8 100-200 mesh

Acid Solution 0.5 M HCl + 0.5 M HF

Pipette tips 1 mL and 5mL or 10 mL (cleaned)

Small Centrifuge Tubes

Acid Holding Beaker

Beakers for Hf Elution

Acid 6 M HCl – Exact

Acid $HClO_4$ – Distilled

Ultrapure H_2O

Acid 24 M HF – Approximate

Acid 6 M HCl – Approximate

Procedure

☐ 1. Label small centrifuge tubes, and pour each sample into one

   a. Centrifuge samples for ~3 min @ 8000 rpm to get rid of any ‘gels’

☐ 2. Get large (5 mL or 10 mL) clean pipette tip from acid bath

   a. Rinse 3 times with μH_2O and wrap in Parafilm to keep clean

☐ 3. Place trays under columns, uncap columns, let drain, then load conditioning step

☐ 4. Load sample, careful not to get any 'gel' from the centrifuge tube into pipette

   a. Drip sample carefully onto empty column

   b. Use new pipette tip for each sample then discard all tips

☐ 5. Load 1st rinse onto columns as soon as empty

   a. May reuse tip as long as it doesn't touch anything

☐ 6. Load 2nd rinse onto columns by repeating as above

☐ 7. Load 1st large wash onto columns

   a. Fill twice with 4 mL in large pipette to reach total volume (8 mL) needed

☐ 8. Rinse the supernatant beakers three times with μH_2O for use in capture step

☐ 9. Load 2nd large wash onto columns

   a. fill twice with 5 mL in large pipette to reach total volume (10 mL) needed

☐ 10. Rinse acid holding beaker and large pipette tip twice with μH_2O

   a. Fill acid holding beaker with 6 M HCl

   b. MUST be exactly 6 M HCl, not just 'close' to it

☐ 11. Make sure all acid drops have gone through and columns are empty, then place collection beakers below their corresponding columns

☐ 12. With beakers below columns add the 6 M HCl to each

   a. Hf comes out in the first mL so don't miss it!

☐ 13. Add 10 drops of $HClO_4$ to each collection beaker

   a. Be very careful it's concentrated!

☐ 14. Place all beakers in a fume hood to evaporate overnight at 80˚C

   a. DON'T allow samples to dry completely

☐ 15. Prepare for column wash by mixing the concentrated (24 M $HF_{Picotrace}$)

a. Prepare in special bottle marked column #1 cleaning

b. Mix approximately ⅓ H_2O and ⅔ $HF_{Picotrace}$ together in this bottle

c. Need 10 mL of this solution for each column used.

☐ 16. Carefully pour HF solution into each column until full

☐ 17. Proceed through remainder of cleaning steps, 3x H_2O rinse, 2x HCl rinse

☐ 18. When columns are done being washed carefully finish filling waste trays with water to dilute acid as much as possible, then carefully pour down the sink with tap on full

☐ 19. Take Parafilm and place on end of each column and cap them

a. Add a small amount of μH_2O to each column to keep damp.

☐ 20. Remove samples from hotplate and cap for next steps, or proceed to next steps (perchloric evaporation) directly.

a. ½ to all acid except $HCLO_4$ should have evaporated

b. Protocol is outlined in Figure 2.9.

Step	Eluent	Volume	Completed ✓											
Condition Column	0.5 M HF, 0.5 M HCl	6 mL												
Load sample	0.5 M HF, 0.5 M HCl	1 mL												
1st Rinse	0.5 M HF, 0.5 M HCl	1 mL												
2nd Rinse	0.5 M HF, 0.5 M HCl	1 mL												
Discard bulk sample	0.5 M HF, 0.5 M HCl	8 mL												
Discard bulk sample	0.5 M HF, 0.5 M HCl	10 mL												
Collect Hf, Zr, Ti	6 M HCl	6 mL												
Clean	24 M HF	10 mL												
Clean	H_20	10 mL												
Clean	6 M HCl	10 mL												
Clean	H_20	10 mL												
Clean	6 M HCl	10 mL												
Clean	H_20	10 mL												

Figure 2.9: Outline for separation of Hf, Zr and Ti using 2 mL AG1-X8 100-200 resin in a BIORAD column.

2.6.3 Perchloric Acid Evaporation

The perchloric acid evaporation step is imperative to the final elution of Hf, and thus must be done carefully and with precision. The function of this step is to remove and remaining HF from the elutant containing Hf, preventing the desired Hf from being lost in the final column. Begin this procedure by placing each eluted sample containing Hf and 10 drops of perchloric acid on a hotplate at 180˚C. Evaporate the samples down until then are roughly 3mm x 3mm in size, tapping them occasionally to cause droplets on the side to fall to the bottom, then add 10 more drops of perchloric acid to each sample. While your samples are evaporating begin draining the final set of Hf-columns (the long Teflon column containing *2 mL of AG 50-X8 200-400 mesh*.) Once your perchloric samples have again evaporated down to ~ 3 x 3 mm, add one final dose of 10 drops of perchloric acid, and begin conditioning your final Hf-columns by filling them completely with 2.5 N HCl and leaving them overnight to drain. When your Hf samples have boiled down to ~3 x 3 mm for the third time you can remove them from the hot plate and allow them to cool in the fume hood for several minutes. Once cooled, seal each beaker with its corresponding lid, and place with its corresponding Hf-column for the following day. (Practical procedure provided below).

Perchloric Acid Evaporation

Reagents

Distilled $HClO_4$

Procedure

☐ 1. Fill air treatment pump with water and turn on both pump and air filter

☐ 2. Turn on hotplate to 180 ˚C

   a. This is the minimum evaporative temperature for $HClO_4$

☐ 3. Place samples into hotplate holder

☐ 4. Evaporate samples to a drop ~5 mm x 5 mm, checking at 20 min intervals

   a. ** DO NOT allow samples to dry completely

   b. * White fumes will appear when $HClO_4$ is evaporating

☐ 5. Begin conditioning column #2 for use by opening and draining them, they should be stocked with μH_2O when not in use

☐ 6. When column #2 are empty, fill them completely with 2.5 M HCl

   a. MUST be **exactly** 2.5 M HCl not just close

   b. Place caps loosely on top while draining

   c. Allow column #2 to drain overnight

☐ 7. When samples have dried down to ~5 mm x 5 mm, add 10 more drops $HClO_4$

   a. You can turn up temperature to 190 ˚C if in a hurry

☐ 8. Once samples have evaporated down as above add 10 drops $HClO_4$ once more

☐ 9. When only a small drop remains (as above) remove samples from the hot plate, allow them to cool in the fume hood, then cap them and place them on the counter until ready for use in the columns

☐ 10. Let pump/air filter clear out air in the box for ~10-15 min then turn off

---

2.6.4 Hafnium Ion-Exchange Column #2

The final Hf-column removed Titanium (Ti), leaving a cute of pure Zr and Hf. This column is incredibly sensitive to HF acid, thus, HF must only be introduced when we are ready to elute the Hafnium. Presuming the following procedure has been followed you may begin by adding 0.5 mL 2.5 HCl to each column to re-wet them. Proceed by again labeling a small, clean, 1.5 mL centrifuge tube for each sample, then proceeding with the following steps. Placing the corresponding sample from each

Teflon beaker used in the perchloric acid step into a corresponding centrifuge tube, then with a clean pipette add 0.4 mL 2.5 HCl, and 60 µL H_2O_2. Close the tubes, shake them, then centrifuge all samples @ 8000 rpm for 2 minutes. Once all the Hf-columns have drained, and the samples have been centrifuged, carefully pipette each sample from the centrifuge tube onto the column resin (using a new pipette time each time), making absolutely sure there are no bubbles or blockages between the sample and the resin. While the columns drain create a mix of 60 mL HCl 2.5 + 240 µL H_2O_2 (per 12 columns) then, once all the columns have drained add 0.4 mL of this solution to each column, careful not to introduce bubbles, or touch the resin or sample (if so use a new pipette tip). Once this solution has passed through the columns, add 5 mL of the same solution to each column, making sure no bubbles are blocking the column. As this solution passes through the columns rinse each collection beaker 3 times with ultra-pure H_2O, and relabel them as necessary, and wait for the columns to empty. Once all columns are empty place the Teflon collections jars under each column and add the final mixture of 60 mL 2.5 N HCl and 1 mL $HF_{Picotrace}$ to elute the Zr and Hf, note the Hf will likely come out in the first few drops so don't miss it. Finally, once all columns have emptied place the samples on a hotplate to dry overnight at 80˚C and cap them the next morning until it is time for analysis. Columns can be cleaned and reused by back washing with ultra-pure H_2O, 4 N HF and 6 N HCl, as described below, and stored in ultra-pure H_2O. (Practical procedure provided below).

Hafnium Ion-Exchange Column #2

Reagents

Centrifuge Tubes 1 mL

Long Thin Column Teflon columns (0.8 cm x 10 cm) – 2 mL of AG 50-X8 200-400 mesh

Reagent grade Peroxide - H_2O_2 (Kept in Fridge)

2.5 N HCl (Exact)

$HF_{Picotrace}$

Procedure

☐ 1. Label centrifuge tubes for each sample

☐ 2. Fill one centrifuge tube with H_2O_2, and return the rest to the fridge

☐ 3. Re-wet columns with 1 mL 2.5 N HCl (if they sat overnight)

☐ 4. To each sample beaker add 0.4 mL 2.5 N HCl and 60 µL H_2O_2

   a. Double these amounts if the samples are going to be split

☐ 5. Pour each sample from its beaker into the corresponding centrifuge tube

☐ 6. Centrifuge samples for 3 min at 8000 rpm

☐ 7. Once columns have drained load each sample onto the column by carefully dripping the sample right onto the resin

   a. if the resin is down the tube a bit carefully drip directly into the tube

   b. make sure there are no bubbles at all blocking the flow

☐ 8. Mix acid for next steps while columns drain, 60 mL HCl 2.5 + 240 µL H_2O_2

☐ 9. Check to make sure sample has gone into column

   a. Often it will get stuck and you will need to use a pipette to get any bubbles out

   b. Be careful not to disturb the resin

☐ 10. Add 0.4 mL of 2.5 N HCl + trace H_2O_2 rinse to each column by carefully dropping it one drop at a time onto the resin so you don't get bubbles

   a. If bubbles occur remove as above

☐ 11. Once first rinse has gone into the column add the next 5 mL as follows…

   a. Dropper the first mL onto the resin as done in the previous steps

b. Make sure there are no bubbles blocking the column

c. Add the remaining 4 mL as usual

☐ 12. Once columns are nearly finished, make the elution solution by mixing 60 mL 2.5 N HCl and 1 mL $HF_{Picotrace}$ (final solution is 2.5 N HCl + 0.3 N HF)

☐ 13. Place collection beakers under each column (if used in previous steps rinse three times with μH_2O first

☐ 14. Add 5 mL of 2.5 HCl + 0.3 HF solution to each column, careful to avoid bubbles as above

Cleaning Column#2

☐ 1. Backwash each column using the special pump to suck water back up the column

a) This removes bubbles produced during steps using H_2O_2

b) Can use "dirty" shared water in this step

☐ 2. Adjust resin stoppers with a pipet tip if necessary to prevent them from falling out

☐ 3. Allow resin to resettle making sure no bubbles are in the columns, re-backwash as necessary to remove bubbles

☐ 4. Once drained proceed to washing steps beginning with 10 mL of 4 N HF for each Teflon tube used, created by mixing ~⅓ $HF_{Picotrace}$ with ⅔ μH_2O.

☐ 5. Wash twice more with 10 mL of 6 N HCl

☐ 6. Backwash columns again using clean μH_2O being careful not to contaminate columns during the washing process

---

Outline of this procedure can be found in Figure 2.10, and see Figure 2.11 for setup and column geometry prior to use.

Step	Eluent	Volume	Completed ✓											
Condition Column	2.5 M HCl	8 mL												
Load sample	2.5 M HCl, 60 µL H_2O_2	0.3 mL												
Rinse	2.5 M HCl, trace* H_2O_2	0.4 mL												
Discard Ti	2.5 M HCl, trace* H_2O_2	5 mL												
Collect Hf, Zr	2.5 M HCl, 0.3 M Hf	5 mL												
** 60 µL H_2O_2 in 15 mL HCl or 240 µL H_2O_2 in 60 mL HCl*														
Backwash	H_20	10 mL												
Clean	4 M HF	10 mL												
Clean	6 M HCl	10 mL												
Clean	6 M HCl	10 mL												
Backwash	H_20	10 mL												

Figure 2.10: Procedure for isolating Hf and Zr on Long Teflon columns using 2 mL AG50-X8 200-400 resin.

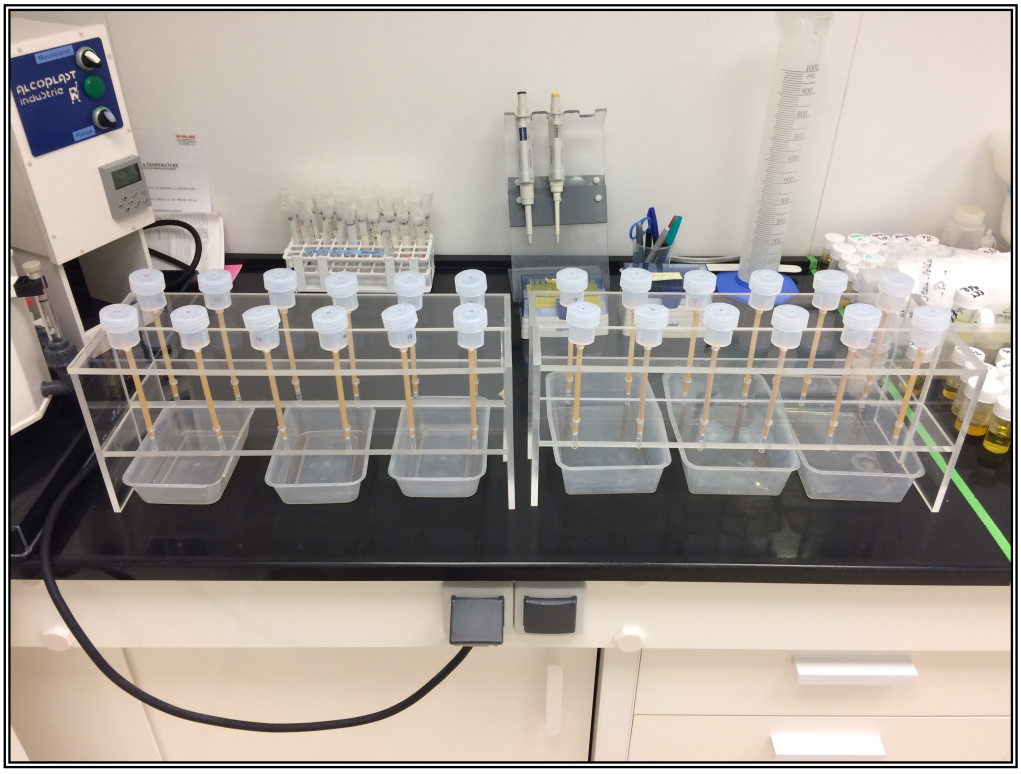

Figure 2.11: Long Teflon columns prepared and conditioned in 2.5 N HCl ready for use as described in the protocol above.

2.7 Calculation of εHf@ time = t

^{176}Hf is a decay product of ^{176}Lu, therefor the calculation of $\varepsilon Hf_{(t)}$ (t = time of formation) requires a correction for the decay of ^{176}Lu into ^{176}Hf over time. This correction can be achieved by utilizing the equations and decay constants as described below.

Concentration of ^{176}Lu/^{177}Hf in a sample

$$\frac{^{176}Lu}{^{177}Hf} = \left(\frac{Lu}{Hf}\right)_{Total\ concentration} * 0.142$$

Modeled age of Sample from CHUR:

$$t = \frac{1}{\boldsymbol{\lambda}} ln\left[\frac{(^{176}Hf/^{177}Hf)^{0}_{sample} - 0.28286}{(^{176}Lu/^{177}Hf)^{0}_{sample} - 0.0334} + 1\right]$$

$\boldsymbol{\lambda}$ = decay constant of ^{176}Lu = 1.867 E^{-11}

t = age of rock formation

0 = denotes modern date of measurement

^{176}Hf/^{177}Hf$_{sample}$ at a given time "t"

$$\left(\frac{^{176}Hf}{^{177}Hf}\right)^{t}_{Sample} = \left(\frac{^{176}Hf}{^{177}Hf}\right)^{0}_{Measured} - \left(\frac{^{176}Lu}{^{177}Hf}\right)^{0}_{Measured} * \left(e^{\boldsymbol{\lambda}t} - 1\right)$$

^{176}Hf/^{177}Hf$_{CHUR}$ at a given time "t"

$$\left(\frac{^{176}Hf}{^{177}Hf}\right)^{t}_{CHUR} = 0.28286 - 0.0334 * \left(e^{\boldsymbol{\lambda}t} - 1\right)$$

$\boldsymbol{\lambda}$ = decay constant of ^{176}Lu = 1.867 E^{-11}

t = age of rock formation

$\boldsymbol{\varepsilon}$Hf at time of formation

$$\boldsymbol{\varepsilon}(Hf)_{(t)}\left[\frac{(^{176}Hf/^{177}Hf)^{t}_{sample}}{(^{176}Hf/^{177}Hf)^{t}_{CHUR}} - 1\right] * 10^{4}$$

2.8 Trace Element Geochemistry

Initial Determination of trace element values is required to optimize the amount of spike needed to determine very precisely the Lu and Hf content of our samples as BIF are extremely low in these elements (10's-100's ppb/g sample). As well as to determine the overall composition of REE in the sample . The procedure used for this analysis is a follows:

2.8.1 Trace Element Procedure For BIF

Reagents

Standards (BIR1, BCR2, BHVO2)

Picotrace Purity HF

14.7 M HNO_3

Picotrace HF

Ultra Pure H_2O

Procedure

1. Select 5 or 7 mL Teflon Savillex beakers and label them appropriately
2. Include one Blank, and three standards (BIR1, BCR2, BHVO2)
3. Weigh sample material into beakers and record weight (0.05 – 0.1 g for BIF's)
4. Add one drop of UP H_2O after weighing to prevent sample loss from static
5. Add 36 drops of 14.4 N HNO_3 (1 mL), and Add 72 drops of Picotrace HF (2 mL) to each beaker
6. Cap and place on a hotplate for 48 h @ 90˚C
7. Sonicate after 24 h and increase to 110˚C
8. Remove samples from hot plate, allow cooling to room temperature

a. Agitate samples to ensure all condensation and droplets are collected in the bottom of the container
b. Carefully uncap samples and place both sample and lid on hotplate to dry for 12-48 h (until dry) @ 90˚C

9. Add 1 mL 14.4 N HNO_3 to each sample, recap each bottle
    a. Place samples back on the hotplate for 24 h at 90˚C
    b. Sonicate samples and return to hotplate for 24 h
10. Remove samples from hot plate, allow cooling to room temperature
    a. Agitate samples to ensure all condensation and droplets are collected in the bottom of the container.
    b. Uncap samples and place both sample and lid on a hotplate to dry for 12-48 h (until dry) @ 90˚C
11. Add 5 mL 6 N HCl to each sample, recap each bottle
    a. Place samples back on the hotplate for 24 h at 90˚C
    b. Label stock solution containers (15-20 mL) and weigh each one empty
12. Remove samples from hot plate, allow cooling to room temperature
    a) Pour sample solution from each Teflon container into corresponding stock container
    b) Rinse each container/lid twice with 6 N HCl and add it to the stock container
    c) Fill Teflon container once with 3 N HCl and add it to the stock container
13. Clean Teflon containers for follow-up steps
    a) Rinse container and lid 2-3 times with UP-H_2O
    b) Add ~ 2 mL of 14.4 N HNO_3 to each container and re-cap
    c) Place containers on hotplate @ 90˚C for 24 h

2.8.2 Analysis of Trace Element Compositions on an ICP-MS and Treatment of Data

Prior to analysis a 1 ml aliquot of each sample was weighed into a clean Teflon® vial (and then weight recorded) and 70 ppb Tm spike solution was added (and weight recorded) to each sample as described in Barrat et al. (1996). Samples were places on a hotplate at 90˚C and allowed to dry for 24 hours. All samples were then re-dissolved with addition of three drops of 14.4 N HNO_3 and each was rinsed into a new, clean, Falcon Tube® using 14 ml of a 2.5 % HNO_3 solution. All samples were then analyzed on a IC-PMS at the LabEx facilities at IUEM. A sample blank and three known sample standards were analyzed at the beginning of each sample suite to identify any potential errors during sample preparation, and signal drift during analysis was monitored by running a calibration standard of BVHO2 after every three samples.

2.8.2A Use of Tm Spike for Analysis

Determination of atomic abundances in a sample using ICP-MS is an attractive method due to the speed of analysis and its ability to determine even trace amounts of an element in a sample, however it can present a number of problems during analysis. Barrat et al. (1996) identify a variety of both non-spectroscopic matrix effects (analyte suppression or enhancement, analyte signal drift, memory effects), spectroscopic interferences (polyatomic ions, refractory oxide ions, doubly charged ions and isobaric ions), as well as possible loss of sample during analysis as sources of error to consider. To account for these sources of error, and quantify these effects, these authors advocate the addition of an isotopically pure spike of Tm during analysis, due to the availability of inexpensive, high purity Tm solutions/powders, that Tm is mono-isotopic and does not interfere with other rare earth elements (REE's), and the fact that ^{169}Tm has only one isobaric interference, $^{153}Eu^{16}O$, which is easily corrected for, and that the addition

of Tm to a sample will create a positive Tm anomaly which, taken together with an initial cosmological abundance of Tm, can be used to constrain the initial Tm value, and hence constrain any loss from the factors outlined above, during analysis.

Using this technique the abundance of REE can be accurately calculated using the following equations as outlined in Barrat et al. (1996:)

$C_{Tm*} = 0.02561((C_{Er}/0.166)*(C_{Yb}/0.1651))^{0.5}$

C_{Tm*} = concentration of Tm from analyzed sample solution in µg/g

C_{Er} = concentration of Er in analyzed solution in µg/g

C_{Yb} = concentration of Yb in analyzed solution in µg/g

(2) $R = M_{sol} (C_{Tm} – C_{Tm*}) / M_{Tm}$

R = chemical yield

M_{sol} = weight of solution in g

C_{Tm} = measured concentration of Tm in solution in µg/g

M_{Tm} = amount of Tm added to solution in µg

$[X] = (M_{Tm}*C_x) / (M*(C_{Tm} - C_{Tm*}))$

[X] = concentration of the element in the sample in ppm

C_x = concentration of element X in solution in µg/g

M = weight of the sample in g

Or preferably $[X] = (M_{Tm} / M)*((C_{Tm} / C_{Tm*}) – 1)^{-1}*(C_x / C_{Tm*})$

The final equation uses element ratios rather than measured concentrations to determine a given elemental concentration in a sample and is preferable for use as it is more robust, i.e. less prone to signal drift then directly measured element concentrations (Barrat et al., 1996). Use of this technique allows for the correction of analytical errors during sample analysis, and a more accurate determination of elemental abundance in unknown silicate samples.

2.9 Isotope Dilution

Isotope dilution is an analytical mechanism by which geochemists can determine with extreme accuracy the actual concentration of an element in a sample. This method involves adding unusually large amounts of a purified isotope to a sample that is otherwise rare, non-existent, or has a precise ratio compared to other isotopes of the same element in nature. The best isotopes to use are those that are extinct (i.e. no longer exist in nature, are artificial, i.e. can only be made by humans, or are very rare in nature, in which case they are enriched for by centrifugation, much like uranium is purified for reactors or weapons). Ultimately, a known amount of "spike" (rare isotope), with a known concentration and a known composition, is added to a sample for analysis, and the ratio of that newly added rare isotope is compared to the other isotopes in the sample analyzed. Given that we know to high accuracy the composition of each isotope for each element, any difference between the natural isotope abundance and the ratio measured must be due to the amount of that isotope added and the amount of natural material present (e.g., natural elemental concentration). Through a series of complex mathematical equations, we can then determine exactly how much of the original element was in the sample to create the change observed after adding and analyzing the isotope ratio of the spiked mixture.

2.9.0 Creation and Calibration of a new ^{179}Hf-^{176}Lu Spike

Spike Calibration Procedure

2.9.1 Determining Spike Composition

Both Hf (~74.8 ppb) and Lu (~100 ppb) pure spikes, bracketed by standards (200 ppb JMC 475 for Hf and 20 ppb P-CAL for Lu), were analyzed for all isotopes (Yb 172, 173), (Lu 175, 176) and Hf (176, 177, 178, 179, 180) on a Neptune MC-ICP-MS to determine their precise isotopic composition. Sample order was as follows: standard (x4), spike, standard (x4), spike (x4), standard (x4).

Due to the exotic composition of the spike, mass-bias corrections could not be performed using the natural ratios of hafnium or lutetium. Instead mass bias corrections were calculated as an average value from the standards that bracketed each spike sample, and applied to the spike measurements using the following equation:

$$f = \frac{ln\left(\frac{^{179}Hf/^{177}Hf_{True}}{^{179}Hf/^{177}Hf_{Measured}}\right)}{ln\left(\frac{Mass_{^{179}Hf}}{Mass_{^{177}Hf}}\right)}$$

Mass-corrected ratios were then calculated for all isotope ratios relative to a constant isotope (175 for Lu and 177 for Hf) as follows:

$$Ratio_{True} = \left(\frac{^{179}Hf}{^{177}Hf}\right)_{measured} * \left(\frac{Mass_{^{179}Hf}}{Mass_{^{177}Hf}}\right)^{f}$$

Applying the following equations, then averaging the mass-corrected ratios for the 8-spike analysis spike composition was determined; results are found in Table 2-3.

For contribution of each isotope in the Lutetium spike:

$$\%^{175}Lu = \frac{100}{\left(\frac{^{175}Lu}{^{175}Lu} + \frac{^{176}Lu}{^{175}Lu}\right)\left(1/\frac{^{175}Lu}{^{175}Lu}\right)}$$

$$\%^{176}Lu = \frac{100}{\left(\frac{^{175}Lu}{^{175}Lu} + \frac{^{176}Lu}{^{175}Lu}\right)\left(1/\frac{^{176}Lu}{^{175}Lu}\right)}$$

For contribution of each isotope in the Hafnium spike:

$$\%^{176}Hf = \frac{100}{\left(\frac{^{176}Hf}{^{177}Hf} + \frac{^{177}Hf}{^{177}Hf} + \frac{^{178}Hf}{^{177}Hf} + \frac{^{179}Hf}{^{177}Hf} + \frac{^{180}Hf}{^{177}Hf}\right)\left(1/\frac{^{176}Hf}{^{177}Hf}\right)}$$

$$\%^{177}Hf = \frac{100}{\left(\frac{^{176}Hf}{^{177}Hf} + \frac{^{177}Hf}{^{177}Hf} + \frac{^{178}Hf}{^{177}Hf} + \frac{^{179}Hf}{^{177}Hf} + \frac{^{180}Hf}{^{177}Hf}\right)\left(1/\frac{^{177}Hf}{^{177}Hf}\right)}$$

$$\%^{178}Hf = \frac{100}{\left(\frac{^{176}Hf}{^{177}Hf} + \frac{^{177}Hf}{^{177}Hf} + \frac{^{178}Hf}{^{177}Hf} + \frac{^{179}Hf}{^{177}Hf} + \frac{^{180}Hf}{^{177}Hf}\right)\left(1/\frac{^{178}Hf}{^{177}Hf}\right)}$$

$$\%^{179}Hf = \frac{100}{\left(\frac{^{176}Hf}{^{177}Hf} + \frac{^{177}Hf}{^{177}Hf} + \frac{^{178}Hf}{^{177}Hf} + \frac{^{179}Hf}{^{177}Hf} + \frac{^{180}Hf}{^{177}Hf}\right)\left(1/\frac{^{179}Hf}{^{177}Hf}\right)}$$

$$\%^{180}Hf = \frac{100}{\left(\frac{^{176}Hf}{^{177}Hf} + \frac{^{177}Hf}{^{177}Hf} + \frac{^{178}Hf}{^{177}Hf} + \frac{^{179}Hf}{^{177}Hf} + \frac{^{180}Hf}{^{177}Hf}\right)\left(1/\frac{^{180}Hf}{^{177}Hf}\right)}$$

Table 2.2: Hf Spike Composition

Sample Name	Mass corrected Ratios				
	$^{176}Hf/^{177}Hf$	$^{177}Hf/^{177}Hf$	$^{178}Hf/^{177}Hf$	$^{179}Hf/^{177}Hf$	$^{180}Hf/^{177}Hf$
Hf Pcal	0.2820373	1.0000000	1.4667582	0.7325000	1.8866153
Spike	0.1502385	1.0000000	2.9117875	77.2199733	7.5315468
Hf Pcal	0.2820481	1.0000000	1.4667032	0.7325000	1.8864591
Spike	0.1498188	1.0000000	2.9155288	77.4300429	7.5472224
Hf Pcal	0.2820362	1.0000000	1.4666922	0.7325000	1.8864950
Spike	0.1496898	1.0000000	2.9174353	77.5276020	7.5548575
Hf Pcal	0.2820431	1.0000000	1.4666408	0.7325000	1.8863317
Spike	0.1497757	1.0000000	2.9164411	77.4838840	7.5503536
Hf Pcal	0.2820241	1.0000000	1.4664682	0.7325000	1.8861533
Spike	0.1496425	1.0000000	2.9171779	77.5184887	7.5527296
Spike	0.1495663	1.0000000	2.9174598	77.5597915	7.5573089
Spike	0.1495444	1.0000000	2.9179938	77.5656296	7.5571227
Spike	0.1496921	1.0000000	2.9172869	77.5265942	7.5550906
Hf Pcal	0.2820695	1.0000000	1.4666970	0.7325000	1.8862261
Hf Pcal	0.2821153	1.0000000	1.4672483	0.7325000	1.8868373
Hf Spike	0.1501159	1.0000000	2.9142165	77.2562274	7.5374741
Hf Spike	0.1505150	1.0000000	2.9091474	76.9886322	7.5168233
Hf Spike	0.1500463	1.0000000	2.9149489	77.2925817	7.5404047
Hf Spike	0.1501567	1.0000000	2.9133693	77.2132226	7.5327259
Hf Pcal	0.2821123	1.0000000	1.4672386	0.7325000	1.8869180
Average Spike Ratio	0.1499002	1.0000000	2.9152328	77.3818892	7.5444717
Hf Spike Composition	^{176}Hf % 0.17	^{177}Hf % 1.12	^{178}Hf % 3.28	^{179}Hf % 86.95	^{180}Hf % 8.48

Table 2.3: Lu Spike Composition

Sample Name	Mass corrected Ratios	
	$^{175}Lu/^{175}Lu$	$^{176}Lu/^{175}Lu$
Lu PCAL	1.0000000	0.0268042
Spike	1.0000000	2.9333935
Lu Pcal	1.0000000	0.0268715
Spike	1.0000000	2.9338725
Lu Pcal	1.0000000	0.0268936
Spike	1.0000000	2.9316435
Lu Pcal	1.0000000	0.0270381
Spike	1.0000000	2.9239547
Lu Pcal	1.0000000	0.0269128
Lu Spike	1.0000000	2.9295838
Lu Spike	1.0000000	2.9313257
Lu Spike	1.0000000	2.9360263
Lu Spike	1.0000000	2.9387725
Lu Pcal	1.0000000	0.0273016
Average Spike Ratio	1.0000000	2.9323216
Hf Spike Composition	^{175}Lu % 25.43	^{176}Lu % 74.57

2.9.2 Determining Spike Concentration

To determine the concentration of the Lu and Hf spikes a mixing series between the known standards BIR1, BCR-2, and BHVO-2 and the spike were created. Dilutions of the known standards and the spike were weighed as accurately as possible when they were created to ensure we knew the exact mass that was used to create each standard and spike mixture, and hence could use the standards to calculate the spikes exact concentration. The sample and spike weights recorded as well as the final spike concentration obtained for each can be found in Table 4 and 5.

Mass-bias and mass-corrected ratios were then calculated as above for the enriched isotope in the lutetium (176/175Lu) and hafnium (179/177Hf) spikes, and the total concentration of the spike was then determined by calculating the contribution of each component (standard and spike) to the overall observed signal on the mass spectrometer as follows:

$$Hf\ Spike_{Concentration} =$$

$$\frac{Standard_{Concentration}\left(Ratio_{179/177Hf} * Standard_{\%177Composition} - Standard_{\%179Composition}\right)}{\left(Spike_{\%179Composition} - Spike_{\%177Composition} * Ratio_{179/177Hf}\right)}$$

Table 2.4: Hf spike concentration based on the concentration of Geo-Standards

GeoRem Preferred Values for Hafnium		
Sample Name	ppb Hf/g sample	Uncertainty +/- ppb
BIR	582.2	8.8
BIR25	582.2	8.8
BCR	4972	34
BCR25	4972	34
BHVO2	4470	25
BHVO25	4470	25
Weight of Samples and Spike		
Sample Name	Weight Sample (g)	Weight Spike (g)
BIR	0.09439	0.55853
BIR25	0.11182	0.69650
BCR	0.11069	1.02478
BCR25	0.09817	1.32825
BHVO2	0.18333	3.04112
BHVO25	0.10228	0.74850
Hf Ratio of Sample and Spike Concentration		
Sample Name	$^{179}Hf/^{177}Hf$	Spike (ppb)
BIR	1.68321	20.46
BIR25	1.72603	20.32
BCR	0.92322	22.20
BCR25	1.00230	21.51
BHVO2	1.06942	19.71
BHVO25	0.90342	22.63
Average Spike Concentration (ppb)		21.14
Mother Spike Concentration (ppb)		19223.12

Table 2.5: Lu spike concentration based on the concentration of Geo-Standards

GeoRem Preferred Values for Lutetium		
Sample Name	ppb Lu/g sample	Uncertainty +/- ppb
BIR	248.4	3.2
BIR25	248.4	3.2
BCR	504.9	7.8
BCR25	504.9	7.8
BHVO2	275.4	2.4
BHVO25	275.4	2.4
Weight of Samples and Spike		
Sample Name	Weight Sample (g)	Weight Spike (g)
BIR	0.09439	0.55853
BIR25	0.11182	0.69650
BCR	0.11069	1.02478
BCR25	0.09817	1.32825
BHVO2	0.18333	3.04112
BHVO25	0.10228	0.74850
Hf Ratio of Sample and Spike Concentration		
Sample Name	$^{176}Lu/^{175}Lu$	Spike (ppb)
BIR	0.11402	4.99
BIR25	0.11965	5.05
BCR	0.09534	5.06
BCR25	0.12728	5.13
BHVO2	0.24341	5.19
BHVO25	0.12253	4.92
Average Spike Concentration (ppb)		5.06
Mother Spike Concentration (ppb)		22380.55

2.9.3 Determination Hf-Nd-Sm and Lu Concentrations using Isotope Dilution

To obtain the most precise results with the least error it is important to tailor the amount of spike added to each sample to be at an optimal ratio compared to the actual concentration of each element in the sample. The optimal spike to sample ratios is described as the lowest point ($R_{optimal}$) in a mixing parabola between the spike and the sample concentrations (Figure 2.12), and is calculated using the following equation:

$$R_{Optimal} = \sqrt{\left(\frac{Amount_{Heavy\ isotope}}{Amount_{Light\ isotope}}\right)_{Sample}\left(\frac{Amount_{Heavy\ isotope}}{Amount_{Light\ isotope}}\right)_{Spike}}$$

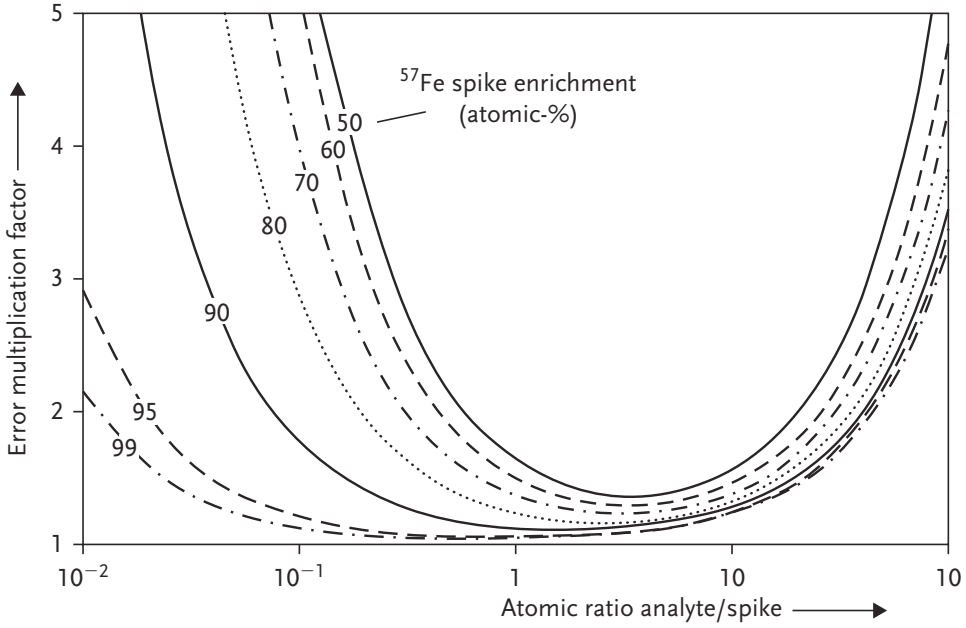

Figure 2.12: Error multiplication factors for isotope dilution mass spectrometry determination an element (example: iron) as a function of the analyte/spike atomic ratio for different spike enrichments of ^{57}Fe. *From Isotopic Analysis (2012), Chapter 8.2.3, by Vanhaecke and Degryse.*

2.10 ^{176}Hf/^{177}Hf MC-ICP-MS Corrections

Corrections for the determination of the ^{176}Hf/^{177}Hf ratio of our samples as measured on the mass spectrometer requires taking into account mass interferences from both ^{176}Lu and ^{176}Yb. These corrections are applied to the raw voltage count data from the instrument after as follows:

$$Total\ Volts_{176Hf} = Volts\ Hf_{measured} - Volts\ Hf_{blank}$$

$$Total\ Volts_{177Hf} = Volts\ Hf_{measured} - Volts\ Hf_{blank}$$

$$Total\ Volts_{173Yb} = Volts\ Yb_{measured} - Volts\ Yb_{blank}$$

$$Total\ Volts_{175Lu} = Volts\ Lu_{measured} - Volts\ Lu_{blank}$$

$$Mass\ Bias_{179/177Hf} = f = \frac{Ln(^{179/177}Hf_{Natural}/(^{179}Hf_{volts}/^{179}Hf_{volts}))}{Ln(^{179}Hf_{mass} - ^{177}Hf_{mass})}$$

$$^{179/177}Hf_{Natural} = 0.7325$$

Mass of each isotope is listed in Table 2.1

As our samples were suspected (and due to zircon inclusion and Lu decay over time) expected to be far from the natural abundance measurements for ^{176}Hf and ^{177}Hf, thus standard bracketing was used to calculate this mass bias between each set of standards and samples. The sample order was as follows: standard, sample x4, then standard again. Mass bias drift for each actual sample was then calculated by averaging the drift from the first and last bracketing standard for each 4-sample set. The standard used for this purpose was the international standard for hafnium JMC 475.

2.10.1 Ytterbium Correction:

$$Volts_{176Yb} = r = (^{173/176}Yb_{Natural}/(^{173}Yb_{mass}/^{176}Yb_{mass})^{f}$$

$$^{173/176}Yb_{Natural} = 1.26411$$

Mass of each isotope is listed in Table 2.1

$$^{176}Yb_{volts} = {}^{173}Yb_{total\ volts}/r$$

2.10.2 Lutetium Correction:

$$Volts_{176Lu} = r = (^{175/176}Lu_{Natural}/(^{175}Lu_{mass}/^{176}Lu_{mass})^{f}$$

$$^{175/176}Lu_{Natural} = 37.6100$$

Mass of each isotope is listed in Table 2.1

$$^{176}Lu_{volts} = {}^{176}Yb_{total\ volts}/r$$

2.10.3 Final ^{176}Hf Value:

$$^{176}Hf_{\ corrected} = Total\ Volts_{176Hf} - {}^{176}Yb_{volts} - {}^{176}Lu_{volts}$$

2.10.4 Mass corrected Ratio of $^{176}Hf/^{177}Hf$:

$$^{176}Hf/^{177}Hf = (^{176}Hf_{\ corrected}/^{177}Hf_{total\ volts}) * (^{176}Hf_{mass}/^{177}Hf_{mass})^{f}$$

2.11 $^{179}Hf/^{177}Hf$ corrections for determining Hf concentration with a ^{179}Hf Spike

As with determination of the $^{176}/^{177}$Hf ratio the initial steps are very similar and outlined as follows. Mass bias was again a calculated average determined from averaging the drift from 2 JMC-475 standards, bracketing 4 samples as in this case we know for a fact that our $^{179/177}$Hf ratios will not be natural due to the addition of a ^{179}Hf spike to the sample.

$$Total\ Volts_{177Hf} = Volts\ Hf_{measured} - Volts\ Hf_{blank}$$

$$Total\ Volts_{179Hf} = Volts\ Hf_{measured} - Volts\ Hf_{blank}$$

$$Mass\ Bias_{179/177Hf} = f = \frac{Ln(^{179/177}Hf_{Natural}/(^{179}Hf_{volts}/^{179}Hf_{volts}))}{Ln(^{179}Hf_{mass} - {}^{177}Hf_{mass})}$$

$$^{179/177}Hf_{Natural} = 0.7325$$

Mass of each isotope is listed in Table 2.1

$$^{179}Hf/^{177}Hf_{\ spiked} = (^{179}Hf_{\ total\ volts}/^{177}Hf_{total\ volts}) * (^{179}Hf_{mass}/^{177}Hf_{mass})^{f}$$

By having carefully weighed the initial mass of the sample, the initial mass of the spike added, combined with knowing the exact composition and concentration of the spike (as discussed previously) we can calculate very precisely the initial amount of Hafnium in the sample by observing the difference in its spiked $^{179/177}$Hf ratio compared to what is expected in natural samples as follows:

$$Total\ Hf_{\frac{ppb}{g}} =$$

$$\frac{Spike_{Concentration} * \left(Spike_{mass} * (Ratio_{\substack{\frac{177}{179}Hf \\ measured}} * Spike_{\%177Composition} - Spike_{\%179Composition}) \right)}{\left(Sample_{mass} * (Natural_{\%179Composition} - (Ratio_{\substack{\frac{177}{179}Hf \\ measured}} * Natural_{\%177Composition}) \right)}$$

2.12 *^{176}Lu/^{175}Lu corrections for determining Lu concentrations using a ^{176}Lu Spike*

The procedure for determination of the $^{176/175}$Lu ratio, is a combination of the steps needed for calculating $^{176/177}$Hf due to mass interferences from ^{176}Yb followed by the same equations as used for determining the total concentration of Hf in a sample. Mass bias was calculated by averaging the drift from 2 bracketing Lu P-CAL standard solutions, bracketing 4 samples as again, in this case we know for a fact that our $^{176/175}$Lu ratios will not be natural due to the edition of the ^{176}Lu spike to the sample.

$$Total\ Volts_{175Lu} = Volts\ Lu_{measured} - Volts\ Lu_{blank}$$

$$Total\ Volts_{177Lu} = Volts\ Lu_{measured} - Volts\ Lu_{blank}$$

$$Total\ Volts_{173Yb} = Volts\ Yb_{measured} - Volts\ Yb_{blank}$$

$$Mass\ Bias_{175/176Lu} = f = \frac{Ln(^{175/176}Lu_{Natural}/(^{175}Lu_{volts}/^{176}Lu_{volts}))}{Ln(^{175}Lu_{mass} - ^{176}Lu_{mass})}$$

$$^{175/176}Lu_{Natural} = 37.6100$$

Mass of each isotope is listed in Table 2.1

2.12.1 Ytterbium Correction:

$$Volts_{176Yb} = r = ({}^{173/176}Yb_{Natural}/({}^{173}Yb_{mass}/{}^{176}Yb_{mass})^{f}$$

$${}^{173/176}Yb_{Natural} = 1.26411$$

Mass of each isotope is listed in Table 2.1

$${}^{176}Yb_{volts} = {}^{173}Yb_{total\ volts}/r$$

2.12.2 Final ^{176}Lu Value

$${}^{176}Lu_{\ corrected} = Total\ Volts_{176Lu} - {}^{176}Yb_{volts}$$

2.12.3 Mass corrected Ratio of ^{176}Lu/^{175}Lu:

$${}^{176}Lu/{}^{175}Lu = ({}^{176}Lu_{\ corrected}/{}^{175}Lu_{total\ volts}) * ({}^{176}Lu_{mass}/{}^{175}Lu_{mass})^{f}$$

Again by having carefully weighed the initial mass of the sample, the mass of the spike added, combined with knowing the exact composition and concentration of the spike (as discussed previously) we can calculate very precisely the initial amount of Lutetium in the sample by observing the difference in its spiked $^{176/175}$Lu ratio compared to what is expected in natural samples as follows:

$$Total\ Lu_{\frac{ppb}{g}} =$$

$$\frac{Spike_{Concentration} * \left(Spike_{mass} * (Ratio_{\ \underset{measured}{\frac{176}{175}Lu}} * Spike_{\%175Composition} - Spike_{\%176Composition}) \right)}{\left(Sample_{mass} * (Natural_{\%176Composition} - (Ratio_{\ \underset{measured}{\frac{176}{175}Lu}} * Natural_{\%175Composition}) \right)}$$

2.13 Major Element Geochemistry by ICP AES

Major elements were determined at the PSO/IUEM (Pôle Spectrométrie Océan, Institut Universitaire Européen de la Mer, Brest, France), based on the analytical procedure of Cotten et al. (1995). Approximately 250 mg of rock power was dissolved in 15 mL closed Teflon vessels filled with 3 mL of concentrated HF (40%), 3 mL of concentrated HCl (32%), and 1 mL of concentrated HNO_3 (65%), which were heated to 90°C for 24 hours. Finally before analysis, 93 ml of H_3BO_3 aqueous solution (20 g/L H_3BO_3) was added to neutralize the excess HF. All reagents used were analytical grade. Elements were measured by inductively coupled plasma-atomic emission spectrometry (ICP-AES) using a Horiba Jobin Yvon® Ultima 2 spectrometer. The boron included in the solution was used as an internal standard. Calibrations were made using international standard, ACE, JB2, WSE. The relative standard deviation is ≤1% for SiO2 and ≤2% for the other major elements.

2.14 References

Barrat, J.A., Keller, F., and Amossé, J. Determination of Rare Earth Elements in Sixteen Silicate Reference Samples by ICP-MS After Tm Addition and Ion exchange separation. *Geostandards Newsletter,* 20, (1996).

Blichert-Toft, J., Chauvel, C., & Albarède, F. Separation of Hf and Lu for high-precision isotopic analysis of rock samples by magnetic sector-multiple collector ICP-MS. *Contributions to Mineral Petrology*, 127, (1997).

Cotton, J., Le Dez, A., Bau, M., Caroff, M., Maury, R.C., Dulski, P., Fourcade, S., Bohn, M., Brousse, R. Origin of anomalous rare-earth element and yttrium enrichments in subaerially exposed basalts: Evidence from French Polynesia. *Chemical Geology,* 119, (1995).

Vanhaecke, F. and Degryse, P. Isotopic Analysis: Fundamentals and Applications Using ICP-MS. *Weinheim, Germany:* Wiley-VCH Verlag & Co. KGaA, Boschstr., (2012).

Chapter 3: Hafnium isotope evidence for emergence of the continents prior to 3.22 billion years ago

3.1 Abstract

The emergence of the continents above sea level during the early Precambrian would have created the first terrestrial habitats, initiated subaerial weathering of continental material, and marked the beginning of the modern sedimentary cycle, yet the history of continental emergence is largely unknown[1]. Emergence depends more on the thermal evolution of the upper mantle and its control on hypsometry than on the amount of differentiated crust, and current models suggest that for all proposed histories of early mantle differentiation, the Earth was a near-waterworld until ca. 3 Gyr ago[1]. Here we report that similar to modern seawater and ferromanganese nodules[2], banded iron formations (BIFs) from multiple localities in the 3.22 Gyr old Moodies Group, Barberton Greenstone Belt, South Africa, show Hf-Nd isotope systematics that depart from the terrestrial array in a manner that can only be explained by sedimentary transport and weathering under subaerial conditions. Initial epsilon Hafnium values ($\varepsilon Hf(i)$, calculated for t = 3.22 Gyr ago) for this sample set range from -14.7 to +36.6, among the most extreme ever reported, but comparable to modern Amazon river waters and sediments[3]. Our findings constitute the earliest geochemical evidence of subaerial weathering processes effecting oceanic chemistry, ruling out a Mesoarchean waterworld and placing continental emergence by 3.22 Gyr ago.

3.2 Main Text

The emergence of continental landmasses above sea level during the Archean would have dramatically changed the chemistry of the oceans and atmosphere, and had profound effects on the biosphere, yet the history of continental emergence is poorly constrained. Numerical modeling suggests that the amount of emergent landmass is not related to the production of continental crust, but rather depends on mantle temperature and its control on continental hypsometry[1]. These models suggest that for nearly any possible history of continental crust production, the Earth's surface was effectively flooded prior to 3.5 Gyr ago, and that less then 2% of the modern landmass had emerged from the ocean by 3.2 Gyr ago, gradually expanding to 5-8% of the modern landmass by 2.5-2.0 Gyr ago[1]. However, this scenario is contradicted by oxygen isotope data suggesting a near-modern aerial extent of emerged landmass (29%) by 2.5 Gyr ago[4], and there exist no geochemical constraints prior to 2.7 Gyr ago[5].

The radiogenic Lu-Hf and Sm-Nd isotope systems, when considered together, are unique in their ability to fingerprint continental weathering under subaerial conditions (For detailed Hf-Lu systematics please see the supplementary information). Nearly all geologic materials fall on a well-defined array in ^{176}Lu-$^{176/177}Hf$ and ^{147}Sm-$^{143/144}Nd$ isotope space called the "terrestrial array"[6,7] as the result of crust and mantle differentiation processes, however, a decoupling of Hf and Nd isotope compositions can occur during subaerial weathering, causing a departure from the terrestrial array to more radiogenic Hf values in weathering fluids at Earth's surface. Crucially, this leads to the formation of the so-called "seawater array", a radiogenic hafnium isotope signature of subaerial continental weathering that is expressed today in rivers and seawater worldwide[2,3,8].

The first observation of this radiogenic hafnium isotope signature was made by Albarède et al.[2] in modern ferromanganese nodules, deep-ocean chemical sediments that derive

most of their trace element content directly from seawater. Similar to modern ferromanganese nodules, Archean chemical sediments, specifically banded iron formations (BIFs), are chemical precipitates that sample the trace element composition of the ancient seawater from which they formed[9,10]. Viehmann et al.[5,11] previously analyzed BIFs as old as 2.7 Gyr for their $\varepsilon Hf_{(i)}$ and $\varepsilon Nd_{(i)}$ compositions and reported a decoupling similar to that observed in modern rivers and seawater, indicating the existence of appreciable emerged continental landmass at that time. However, older BIF, deposited when Earth is thought to have been a near-waterworld, have yet to be examined for potential geochemical constraints on continental emergence.

Accordingly, we examined the ^{176}Lu-$^{176/177}Hf$ and ^{147}Sm-$^{143/144}Nd$ composition of Paleoarchean BIFs from the 3.22 Gyr old Moodies Group, Barberton Greenstone Belt (BGB), South Africa (Figure 3.1A), one of the oldest well-preserved Paleoarchean sedimentary sequences known at present. Moodies Group strata have experienced only greenschist-facies metamorphism, with maximum temperatures reaching ~400˚C[12,13]. Its age is well constrained by U-Pb dating of single zircons from multiple tuff horizons and crosscutting dikes, with sedimentation beginning ~ 3.223 ± 0.001 and ending ~ 3.219 ± 0.009 Gyr ago[14,15]. Field observation and geological mapping (Figure 3.2) shows that Moodies BIFs were deposited in a nearshore environment below wave-base, and are over- and underlain by jaspilite, shales, laminated siltstones, and fine-grained, thin bedded, graded sandstones, interpreted as distal turbidites[(16, this study)]. These BIFs are unique among other Paleoarchean occurrences by their unambiguous association with shallow-water sedimentary facies, and their extraordinary preservation offers a unique window into the composition of near-shore seawater 3.22 billion years ago.

We sampled fresh, unweathered BIF from two outcrop locations of the MdI2 unit from the northern and central BGB (Table 3.1). Out of 48 samples available, those 23 samples

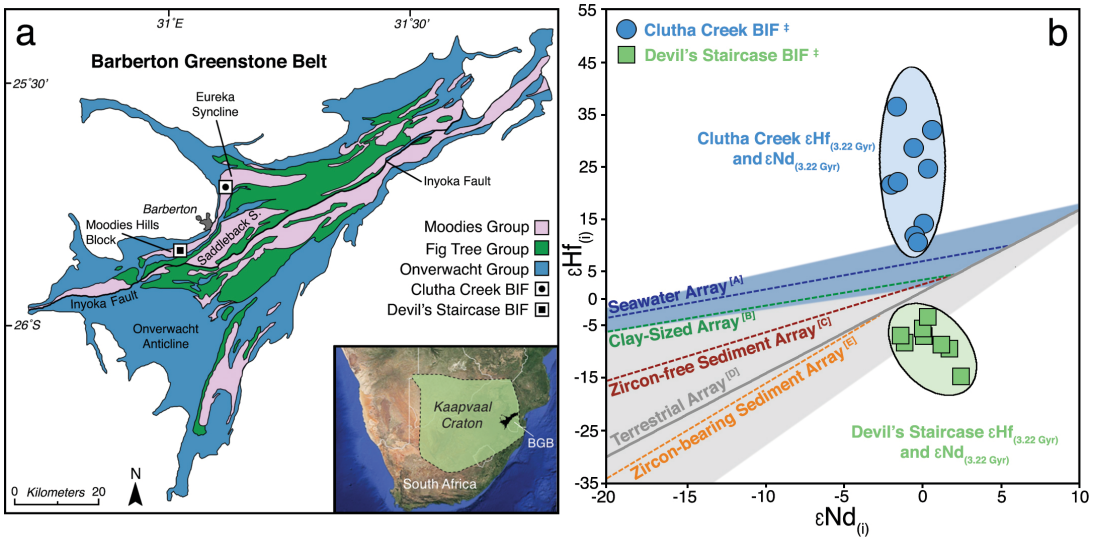

Figure 3.1. Location of sample sites in the Moodies Group, Barberton Greenstone Belt, South Africa, and sample $\varepsilon Hf_{(3.22\ Gyr)}$ and $\varepsilon Nd_{(3.22\ Gyr)}$ values compared to the modern Hf-Nd array. (a) Location and geological map of the BGB, South Africa and Swaziland, showing sample site locations. (b). Moodies Group BIF Hf-Nd data superimposed on the modern terrestrial and seawater arrays, modified after ref. [23]. Moodies Group BIF data clearly comprise two distinct populations as a function of sample locality: those from the Devil's Staircase location fall below the zircon-bearing sediment array, while those from the Clutha Creek location fall within or above the seawater array. Data show an extreme range in $\varepsilon Hf_{(3.22\ Gyr)}$ values but limited spread in $\varepsilon Nd_{(3.22\ Gyr)}$ values, the fingerprint of emerged continental weathering. New data from this study are denoted with the following symbol ‡, while references to previous studies are denoted alphabetically as follows: [A] ref. [2], [B] ref. [22], [C,E] ref. [21], and [D] ref. [7].

---

showing the highest Lu/Hf ratios and lowest Zr/Ti concentrations, thus representing the least detritally-contaminated material, were selected for Lu-Hf and Sm-Nd isotope analyses (Table 3.1). Although some of the samples that we examined possess a negative Ce anomaly that can be attributed to a late overprinting event[17], all available evidence indicates that this late-stage alteration did not affect the Lu-Hf and Sm-Nd isotope composition of the selected samples. Specifically, $\varepsilon Nd_{(3.22\ Gyr)}$ compositions of all samples are remarkably consistent with values reported by other authors across the Barberton Greenstone Belt, and all samples plot along a

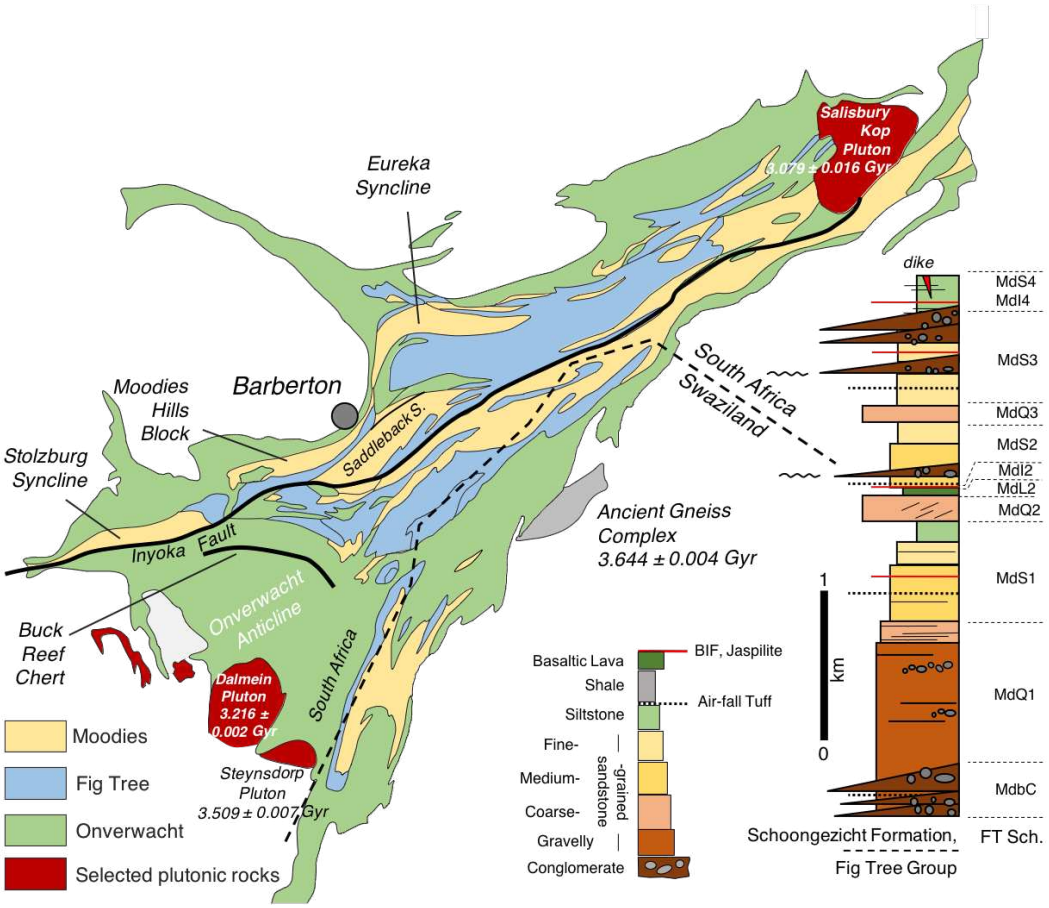

Figure 3.2. Geological map of the Moodies Group BIF with selected surrounding igneous plutons. The stratigraphic column on the right-side of the diagram is an idealized section for the entire Moodies Group. Our BIF samples are all obtained from MdI2, which is associated with a horizon of basaltic lava hosted within a larger unit of course to medium grained-sandstones and conglomerates.

---

^{147}Sm-$^{143/144}Nd$ errorchron of 3.144 ± 0.2 Gyr defined by a larger dataset for the entire Barberton Greenstone Belt (Figure 3.3). Neither Sm-Nd nor Lu-Hf isotope compositions show any correlation with the magnitude of the Ce anomaly, and notably, samples with the most radiogenic Hf compositions have no, or only slight, Ce anomalies (Tables 3.1 and 3.2).

Sample ID	Sample Locality Moodies BIF 3.22 Gyr	Zr Concentration (ppm)	± 5%	Ti Concentration (ppm)	± 5%	Wt% SiO_2	Wt% Fe_2O_3	Wt% AlO_2	Ce/Ce*	εHf at 3.22 Gyr	± 2σ
M6	Devil's Staircase	4.77	0.24	107.2	5.4	63.3	39.6	0.37	0.70	-8.77	0.20
M10	Devil's Staircase	11.39	0.57	273.9	13.7	63.4	34.7	1.00	0.57	-3.47	0.06
M12	Devil's Staircase	6.78	0.34	213.0	10.7	33.7	63.3	0.74	0.56	-6.94	0.13
M14	Devil's Staircase	4.81	0.24	151.0	7.6	63.0	37.9	0.39	0.51	-6.96	0.13
M15	Devil's Staircase	8.08	0.40	221.2	11.1	47.6	51.5	0.75	0.35	-9.28	0.12
M16	Devil's Staircase	5.22	0.26	149.3	7.5	67.2	31.7	0.44	0.29	-14.71	0.02
M44	Devil's Staircase	12.50	0.62	255.7	12.8	56.3	41.4	0.70	0.52	-8.21	0.12
M45	Devil's Staircase	6.35	0.32	152.8	7.6	53.3	45.9	0.40	0.58	-5.71	0.21
M27	Clutha Creek	5.78	0.29	263.1	13.2	57.1	40.9	1.02	0.97	22.07	0.16
M29	Clutha Creek	2.82	0.14	62.2	3.1	68.2	30.8	0.21	0.88	14.30	0.22
M30	Clutha Creek	2.56	0.13	51.4	2.6	67.2	31.2	0.22	0.93	10.76	0.23
M31	Clutha Creek	3.00	0.15	110.6	5.5	73.8	20.7	0.24	0.86	24.83	0.02
M32	Clutha Creek	3.94	0.20	85.9	4.3	69.3	30.2	0.24	0.88	12.01	0.13
M36	Clutha Creek	2.12	0.11	33.2	1.7	80.2	18.6	0.18	0.85	21.79	0.38
M46	Clutha Creek	6.67	0.33	136.6	6.8	74.3	14.1	0.35	0.87	28.86	0.97
M47	Clutha Creek	2.85	0.14	52.8	2.6	81.7	16.4	0.23	0.88	32.12	0.04
M50	Clutha Creek	3.00	0.15	32.70	1.6	80.1	22.3	0.2	0.87	36.63	0.33

Sample Site	Geological Unit	GPS Coordinates
Devil's Staircase	MdI2	25°49'55.82"S 31° 0'50.49"E
Clutha Creek	MdI2	25°41'52.81"S 31° 5'10.89"E

Table 3.1. Major element composition, abundance of detrital indicators Zr and Ti, Ce anomalies (calculated as $Ce/Ce^{*} = Ce / 0.5*(La + Pr)$, all data first normalized to PAAS) and $\varepsilon Hf_{(3.22\ Gyr)}$ values of samples from the Moodies Group BIF unit MdI2.

Sample ID	Sample Locality Moodies BIF 3.22 Gyr	Nd Concentration (ppm)	± 5%	Sm Concentration (ppm)	± 5%	Modern $^{147}Sm/^{144}Nd$	± 2σ	Modern $^{143}Nd/^{144}Nd$	± 2σ	εNd at 3.22 Gyr	± 2σ
M6	Devil's Staircase	2.55	0.13	0.49	0.02	0.11456	0.0011	0.51096	0.000006	1.14	0.36
M10	Devil's Staircase	6.37	0.32	1.24	0.06	0.11694	0.0012	0.51097	0.000007	0.38	0.35
M12	Devil's Staircase	6.18	0.31	1.20	0.06	0.11676	0.0012	0.51087	0.000004	-1.42	0.42
M14	Devil's Staircase	3.77	0.19	0.72	0.04	0.11523	0.0012	0.51092	0.000004	0.05	0.39
M15	Devil's Staircase	7.83	0.39	1.44	0.07	0.11060	0.0011	0.51090	0.000003	1.64	0.40
M16	Devil's Staircase	6.06	0.30	1.11	0.06	0.11015	0.0011	0.51093	0.000004	2.39	0.38
M44	Devil's Staircase	8.86	0.44	1.76	0.09	0.11934	0.0012	0.51094	0.000003	-1.14	0.44
M45	Devil's Staircase	4.33	0.22	0.81	0.04	0.11282	0.0011	0.51086	0.000006	-0.04	0.35
M27	Clutha Creek	1.83	0.09	0.44	0.02	0.14464	0.0014	0.51146	0.000006	-1.53	0.48
M29	Clutha Creek	0.82	0.04	0.17	0.01	0.12757	0.0013	0.51118	0.000009	0.11	0.36
M30	Clutha Creek	0.74	0.04	0.16	0.01	0.13155	0.0013	0.51125	0.000009	-0.28	0.37
M31	Clutha Creek	1.47	0.07	0.29	0.01	0.11729	0.0012	0.51098	0.000010	0.36	0.30
M32	Clutha Creek	0.83	0.04	0.17	0.01	0.12356	0.0012	0.51107	0.000008	-0.48	0.36
M36	Clutha Creek	0.79	0.04	0.17	0.01	0.13307	0.0013	0.51119	0.000011	-1.94	0.33
M46	Clutha Creek	3.84	0.19	0.72	0.04	0.11272	0.0011	0.51084	0.000005	-0.51	0.38
M47	Clutha Creek	1.12	0.06	0.23	0.01	0.12287	0.0012	0.51111	0.000007	0.60	0.38
M50	Clutha Creek	0.74	0.04	0.16	0.01	0.137242	0.0012	0.51130	0.000006	-1.60	0.38

Table 3.2. Nd and Sm concentrations, measured $^{147}Sm/^{144}Nd$, $^{143/144}Nd$, and $\varepsilon Nd_{(3.22\ Gyr)}$ of samples from the Moodies Group BIF unit MdI2.

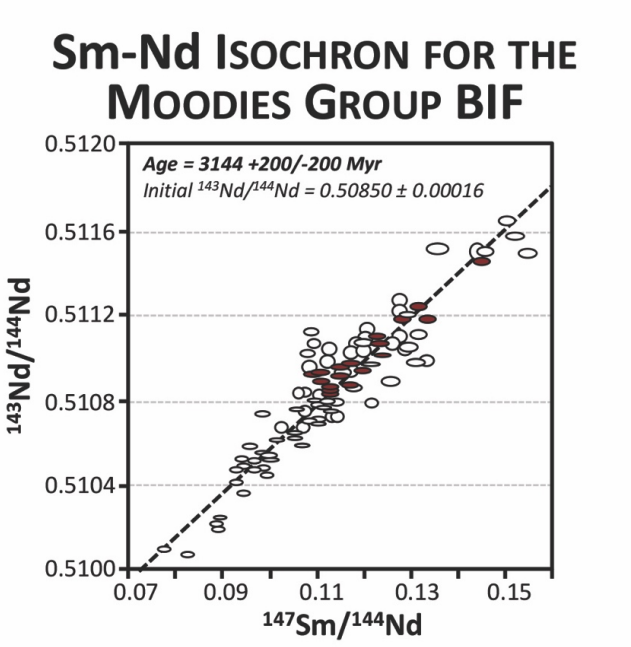

Figure 3.3. Moodies Group BIF Sm-Nd errorchron. Along with a compilation of Sm-Nd isotope data from the Fig Tree and Moodies Groups as well as surrounding volcanic suites, the Sm-Nd isotope composition of Moodies Group BIF samples (red ellipses) define an errorchron at 3.144 ± 0.2 Gyr and an initial $^{143/144}$Nd ratio of 0.5085, consistent with a Moodies Group depositional age of 3.219 – 3.223 Gyr ago[15, 16].

Relative to $\varepsilon Nd_{(3.22\ Gyr)}$, the range in $\varepsilon Hf_{(3.22\ Gyr)}$ values is distinctively extreme, with values ranging from -14.7 to +36.6. They can be divided into two populations: one falling on or below the modern zircon-bearing terrestrial array, and a second on or above the modern seawater array (Figure 3.1B and Tables 3.2 and 3.3). While the $\varepsilon Nd_{(3.22\ Gyr)}$ results appear to represent a mixing of MORB and continentally-derived Nd sources[18], consistent with the Moodies Group's near-shore depositional environment and mixed ultramafic–to–felsic provenance, the Hf isotope data depart significantly from nearly all previously reported compositions, including the terrestrial array (Figure 3.1B).

Sample ID	Sample Locality Moodies BIF 3.22 Gyr	Hf Concentration (ppb)	± 2σ	Lu Concentration (ppb)	± 2σ	Modern $^{176}Lu/^{177}Hf$	± 2σ	Modern $^{176}Hf/^{177}Hf$	± 2σ	εHf at 3.22 Gyr	± 2σ
M6	Devil's Staircase	94.96	0.05	21.37	0.01	0.03139	0.00000	0.28240	0.000006	-8.77	0.20
M10	Devil's Staircase	273.88	0.20	36.62	0.20	0.01864	0.00009	0.28176	0.000004	-3.47	0.06
M12	Devil's Staircase	141.24	0.08	25.31	0.04	0.02498	0.00002	0.28206	0.000005	-6.94	0.13
M14	Devil's Staircase	116.47	0.09	16.51	0.01	0.01962	0.00001	0.28172	0.000004	-6.96	0.13
M15	Devil's Staircase	176.41	0.10	26.59	0.00	0.02102	0.00001	0.28174	0.000004	-9.28	0.12
M16	Devil's Staircase	128.03	0.03	21.54	0.03	0.02342	0.00005	0.28174	0.000004	-14.71	0.02
M44	Devil's Staircase	188.03	0.09	21.25	0.02	0.01576	0.00001	0.28145	0.000004	-8.21	0.12
M45	Devil's Staircase	104.37	0.08	15.77	0.00	0.02108	0.00001	0.28185	0.000007	-5.71	0.21
M27	Clutha Creek	113.52	0.05	31.51	0.02	0.03871	0.00000	0.28372	0.000005	22.07	0.16
M29	Clutha Creek	46.85	0.02	17.24	0.01	0.05125	0.00002	0.28428	0.000007	14.30	0.22
M30	Clutha Creek	43.35	0.02	19.17	0.02	0.06100	0.00004	0.28478	0.000009	10.76	0.23
M31	Clutha Creek	58.63	0.03	23.35	0.07	0.05613	0.00014	0.28488	0.000008	24.83	0.02
M32	Clutha Creek	76.04	0.04	16.98	0.01	0.03116	0.00001	0.28297	0.000004	12.01	0.13
M36	Clutha Creek	27.41	0.01	13.59	0.01	0.06922	0.00002	0.28560	0.000012	21.79	0.38
M46	Clutha Creek	140.18	0.05	44.26	0.31	0.04396	0.00058	0.28424	0.000009	28.86	0.97
M47	Clutha Creek	45.09	0.01	17.88	0.05	0.05521	0.00014	0.28503	0.000010	32.12	0.04
M50	Clutha Creek	27.37	0.00	12.67	0.01	0.06444	0.00002	0.28572	0.000011	36.63	0.33
M317	Moodies Sanstone	7793.18	7.69	162.10	15.77	0.00290	0.00028	0.28093	0.000015	1.57	0.10
M318	Moodies Sanstone	1843.18	0.31	98.05	0.03	0.00742	0.00000	0.28113	0.000011	-1.22	0.38

Table 3.3. Hf and Lu concentrations, measured $^{176}Lu/^{177}Hf$, $^{176}Hf/^{177}Hf$, and $\varepsilon Hf_{(3.22\ Gyr)}$ of samples from the Moodies Group BIF unit MdI2 and stratigraphically equivalent sandstones.

Insight into the origin of these extreme $\varepsilon Hf_{(3.22\ Gyr)}$ compositions can be drawn from the positive correlation between $\varepsilon Hf_{(3.22\ Gyr)}$ values and concentrations of SiO_2, Zr, Sc, and Ti, which suggest variable contributions of detrital and dissolved sources of Hf with distinct isotope compositions (Figure 3.4A, Table 3.1, Figure 3.5). Samples with high concentrations of the detrital indicators Zr, Sc, and Ti are dominated by non-radiogenic Hf compositions, while the purest chemical sediments (< 40 ppb Hf, < 40 ppm Ti) universally show radiogenic Hf isotope compositions. These differences are best attributed to differences in sedimentary input at the two sample localities, in particular to increased chemical sedimentation rate and/or lower detrital input at the Clutha Creek locality relative to the Devil's Staircase locality ~30 km away (Table 3.3). This is consistent with field observations of a closer association and intermixing of clastic sediments in the latter. Although many of these εHf values appear extreme compared to previously published data, based on the theoretical Hf isotope

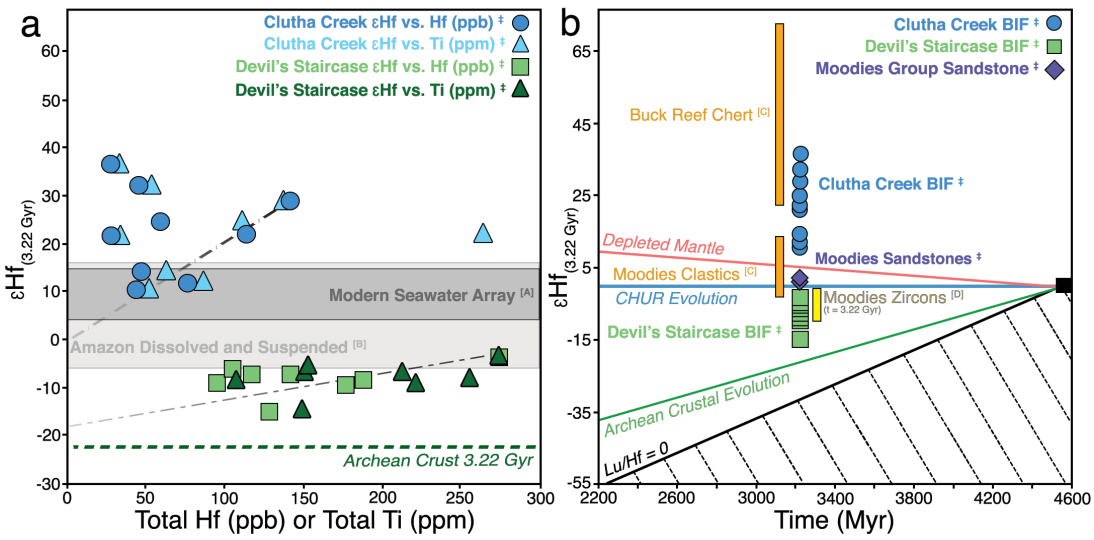

Figure 3.4. Moodies Group BIF $\varepsilon Hf_{(3.22\ Gyr)}$ data plotted as a function of detrital indicators and the $\varepsilon Hf_{(i)}$ evolution of various terrestrial reservoirs through the Hadean and Archean. (a) Crossplot of the total concentrations of detrital indicators Hf and Ti vs. $\varepsilon Hf_{(3.22\ Gyr)}$. Two clear trends emerge when detrital input, site locality and $\varepsilon Hf_{(3.22\ Gyr)}$ are considered, with the lower trend representing detrital contamination by fine-grained materials akin to riverine suspended loads, and the upper trend representing dissolved Hf in chemically pure precipitates. (b) $\varepsilon Hf_{(3.22\ Gyr)}$ data for Moodies Group BIF and sandstone samples compared to other available Paleoarchean sediment data as well as theoretical trajectories for continental crust and mantle evolution between 4.5 and 2.2 Gyr. The nonradiogenic Moodies BIF $\varepsilon Hf_{(3.22\ Gyr)}$ values are consistent with crustal evolution 3.22 Gyr ago, while the radiogenic values cannot be explained by evolution of terrestrial reservoirs. References to previous studies are denoted alphabetically as follows: [A] ref. [2], [B] ref. [3], [C] ref. [20], [D] ref. [19]; and new data from this study are denoted by ‡.

---

composition of the crust 3.22 Gyr ago (see supplementary information), as well as on the Hf isotope composition of Moodies Group detrital zircons[19] projected to their εHf values 3.22 Gyr ago, the highly negative $\varepsilon Hf_{(3.22\ Gyr)}$ compositions can be accounted for by a detrital component rich in older zircons (Figure 3.4B) that are distinctly less radiogenic than bulk Moodies clastic sediments[(20, this study)].

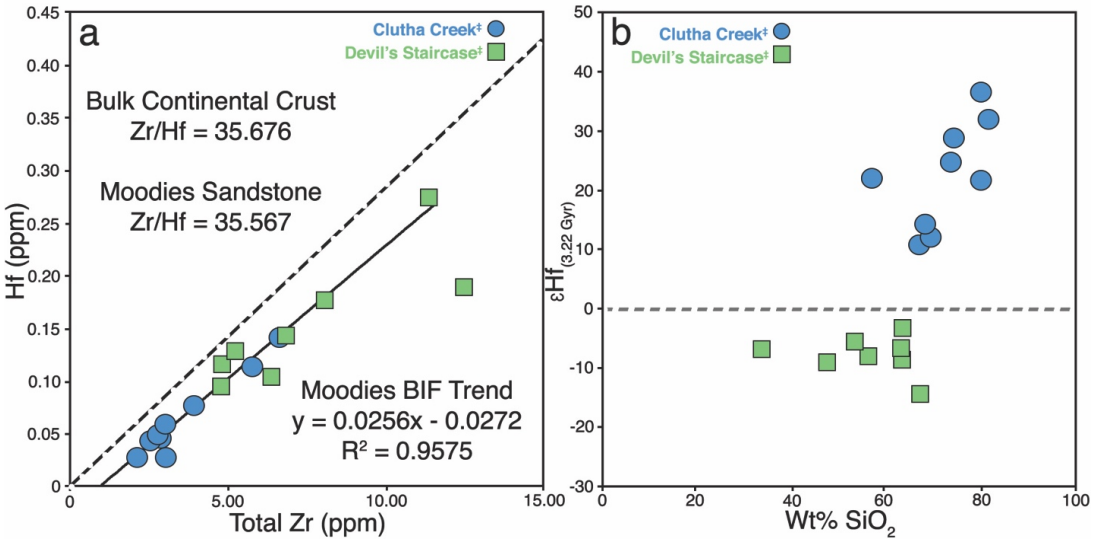

Figure 3.5. Cross plots of Zr and Hf concentrations and $\varepsilon Hf_{(3.22\ Gyr)}$ values vs. total weight percent (Wt%) SiO_2 for Moodies Group BIF samples. (A) Zr/Hf ratios for Moodies Group BIF samples. All BIF values fall below the expected ratio for Zr/Hf compared to the bulk silicate Earth, or the values of coeval Moodies sandstones, indicating a decoupling of the Zr and Hf systems. One outlying data point was excluded for the purposes of calculating the Moodies Group BIF Zr/Hf ratio. (B) $\varepsilon Hf_{(3.22\ Gyr)}$ values for Moodies BIF samples compared to their SiO_2 content. Grouping appears to reflect a site-specific trend of increasing εHf with increasing SiO_2, most notably at the Clutha Creek locality.

The highly radiogenic Hf isotope compositions of the Moodies Group BIFs are best explained by the chemical weathering and physical sorting of emerged continental material[2,3,5-8,11,21-23]. Our results are remarkably similar to those from modern Amazon river sediments, where Hf-Nd isotope decoupling is demonstrated to already have occurred in a continental setting due to incongruent weathering of source materials, but is difficult to detect in fluvial systems due to the suspended detrital components that dominate the riverine Hf load[3]. Only by separating the size fractions of the sediments within the river water itself into suspended load (with non-radiogenic εHf), dissolved/colloidal load (intermediate εHf), and truly dissolved load (strongly radiogenic εHf), can the prominently decoupled Hf-Nd signal of emerged

continental weathering be discerned in the Amazon watershed[3]. By their chemically-pure nature, nearly devoid of all but the finest detrital components, BIFs are ideally placed for capturing Hf isotope compositions at the most radiogenic end of this sedimentary sorting process. Approximately one-third of Moodies BIF εHf isotope compositions are significantly more positive (>20 εHf) than those observed in modern fluvial systems or modern seawater. We interpret these values as representing the truly dissolved, extremely radiogenic portion of Hf entering the ocean from a continent undergoing intense chemical weathering, presumably due to higher surface temperature, higher atmospheric CO_2, and more intense rainfall at 3.22 Gyr ago [24]. Indeed, our data fall well below the upper range of εHf compositions (up to ~ +250 εHf) reported for acid leachates of granites[8] and are thus consistent with values that may be expected in fluids released during intense chemical weathering.

This isotopic signal of continental emergence is well supported by sedimentological evidence in the Moodies Group in the form of paleosols[25], highly mature sandstones[24,26], conglomerate clast weathering rinds[27], sedimentary structures indicating subaerial exposure such as eolian strata[28], desiccation cracks[29], putative raindrop imprints[30], and microbial mats draping alluvial or fluvial conglomerates that appear to have thrived on atmospherically-deposited nitrate[13].

Today, this same Hf isotopic signal is characteristic of passive margins where extensive sedimentary sorting occurs, but is largely absent in sediments on active margins[6]. In the specific case of the Moodies Group, the strata record a partially felsic plutonic provenance, with granites undergoing subaerial weathering and deposition onto an inferred oceanic plateau[15,31, and references therein]; at this time, shallow oceanic plateaus may have covered significant portions of the Earth's surface[32] which may have allowed for prolonged subaerial exposure and extensive sedimentary sorting similar to that occurring on passive margins today. Intriguingly, even more radiogenic Hf isotope compositions have been reported for the 3.45 Gyr old Buck

Reef Chert of the underlying Onverwacht Group[20], which may represent evidence for an even more ancient emergence of continental landmasses.

Despite our data representing a seawater signal, it is difficult to extrapolate our results to estimate the degree of continental emergence at the global scale, considering that the residence time of dissolved Hf in the oceans is low and that Hf as well as Nd are poorly mixed in modern oceans[33]. Nonetheless, the fact that this signal was detected in chemical sediments deposited below wave base suggests that as today, subaerial weathering of emerged continental material exerted important control on the composition of seawater well beyond the shoreline. Our data extend the available evidence for this control over seawater composition to at least 3.22 Gyr ago, and constitute strong geochemical evidence against a near-waterworld prior to 3.0 Gyr ago[1].

The presence of emerged continental landmass 3.22 Gyr ago, especially one felsic in composition, has a broad range of implications for the ancient biosphere. The enhanced dissolution of geological material subaerially exposed to the CO_2-rich Paleoarchean atmosphere would have provided an enhanced flux of essential elements to the oceans and constituted a newfound supply of limiting nutrients to the early biosphere. Phosphorus may have been particularly scarce in Precambrian seawater[34,35], and in this case, enhanced weathering of phosphorus-rich felsic material would have been a particularly important stimulant of marine productivity. Indeed, the unusually abundant microbial mats that formed the rich tidal-facies biosphere preserved in the Moodies Group[13,29] thrived near deltaic sources of nutrients in the shallow-water environments of Earth's primitive shorelines. Our results link the earliest emerged continental landmasses, and the new ecological niches and weathering regimes they presented, to an enhanced supply of nutrients to continental margins, and in turn, to the stimulation of biological productivity in near-shore microbial ecosystems. Ultimately, the emergence of the continents set Earth on an irrevocable trajectory towards a rich terrestrial

biosphere and efficient transfer of nutrients from land to sea, a process that continues to this day to impart control over the biological, redox, and climate evolution of Earth's surface.

3.3 Methods

3.3.1 Trace element analyses

Trace element compositions were obtained after digesting ~100 mg aliquots of samples and resuspending them in 5% HNO_3 with trace HF and a Tm-spike.

3.3.2 Isotopic ratio analyses

Hf isotopes were analyzed by digesting of ~1 g of BIF sample in concentrated HF + HNO_3, followed by a modified (for high iron and low Hf and Lu concentrations) 2-column Hf and Zr purification, followed by a 2-column separation for Nd, Sm, Yb and Lu, and analyzed on a Neptune MC-ICP-MS at Pôle Spectrométry Océan (PSO).

3.3.3 Hf and Lu concentration determinations

Precise determination of Hf and Lu concentrations was achieved after purification (same method as described above) by isotope dilution using ^{179}Hf and ^{176}Lu spiked samples, subsequently measured on the MC-ICP-MS Thermo Neptune at the PSO. Nd isotopes were determined using 70–90 mg of samples digested in concentrated HF + HNO_3 that were passed through a two-column procedure and analyzed on the MC-ICP-MS Neptune and TIMS Triton at the PSO. For detailed methods please see Supplementary Information - Materials and Methods.

3.4 Supplementary Information

3.4.1 Hafnium-Lutecium Geochemistry

During partial melting of the mantle, Hf and Nd preferentially remain in the melt and are eventually sequestered in felsic minerals, while Lu and Sm become enriched in mafic minerals[6]. In the absence of weathering, the crustal ratio of approximately 2:1 is expected for Hf and Nd, and the isotopic compositions $\varepsilon Hf_{(t)}$ and $\varepsilon Nd_{(t)}$ ($^{176/177}Hf$ and $^{143/144}Nd$ isotope ratios in samples normalized to the mean chondritic composition at time "t" and multiplied by 10^4) define the "terrestrial array"[7,21-23] that originates from this geochemical pairing at the whole-rock scale. At the mineralogical scale, Hf is almost entirely partitioned into weathering-resistant phases such as zircon and baddeleyite, while Sm, Nd and Lu are partitioned into less weathering-resistant phases. Some minerals, such as apatite and sphene, are initially Lu-rich, and with time, ^{176}Lu decays to the radiogenic daughter product ^{176}Hf. During subaerial weathering, Sm, Nd, Lu, and by consequence, radiogenic ^{176}Hf, are all preferentially released to leaching fluids, while weathering-resistant phases retain non-radiogenic Hf on land and the continental margins, thus creating the more radiogenic signature of the "seawater array"

3.4.2 Supplementary Materials and Methods

Sampling

Whole-rock hand-samples of Moodies Group BIF were sampled from exposed outcrops and were subsequently cut with a diamond saw to remove weathered surfaces, crushed in a tungsten carbide cylinder, and powdered in an agate mortar to produce adequate amounts of clean sample material for analysis.

Trace element analyses

Trace element compositions were obtained after digesting ~100 mg aliquots of samples in $HClO_4$ + HF mixtures and resuspending them in 5% HNO_3 with trace HF and a Tm-spike.

Solutions were measured on an HR-ICP-MS Thermo Element 2 at the *Institut Universitaire Européen de la Mer,* Plouzané.

Isotopic ratio analyses

Hf isotopes were analyzed by digesting of ~1 g of BIF sample in concentrated HF + HNO_3, followed by a modified (for high iron and low Hf and Lu concentrations) 2-column Hf and Zr purification, as outlined by Blichert-Toft et al. (1997)[36], followed by a two column separation for Nd, Sm, Yb and Lu, and analysis on a Neptune MC-ICP-MS at Pôle Spectrométry Océan (PSO), Plouzané, France. $^{176}Hf/^{177}Hf$ was corrected for Yb and Lu interferences on mass-176, and mass-bias was corrected using multiple bracketing standards: BHVO-2, BCR2 and JMC (for Hafnium), and a P-CAL elemental solution for Lutetium.

Hf and Lu concentration determinations

Precise determination of Hf and Lu concentrations was achieved after purification (same method as described above) by isotope dilution using ^{179}Hf and ^{176}Lu spiked samples, subsequently measured on the MC-ICP-MS Thermo Neptune at the PSO. Nd isotopes were determined using 70–90 mg of samples digested in concentrated HF + HNO_3 that were passed through a two-column procedure modified after Richard et al. (1976)[37], and analyzed on the MC-ICP-MS Neptune and TIMS Triton at the PSO against the JNdi-1 standard. Finally, $\varepsilon Hf_{(i)}$ and $\varepsilon Nd_{(i)}$ values at the time of BIF deposition were calculated using the following values: $(^{176/177}Hf)_{CHUR} = 0.28286$, $(^{176}Lu/^{177}Hf)_{CHUR} = 0.0334$, ^{176}Lu-decay constant $\lambda_{176Lu} = 1.856*10^{-11}$, $(^{143}Nd/^{144}Nd)_{CHUR} = 0.512638$, $(^{147}Sm/^{144}Nd)_{CHUR} = 0.1967$, and ^{147}Sm-decay constant $\lambda_{147Sm} = 6.54*10^{-12}$.

Calculations for the evolution of the crust and depleted mantle

The initial composition of the depleted mantle was based on the results of ref. [38] and taken to be $^{176/177}Hf = 0.283294$, and $^{176}Lu/^{177}Hf = 0.03933$, at time t = 4558 Myr. The initial composition of the crust was derived from ref. [39], with $^{176}Lu/^{177}Hf = 0.0113$, and initial values for CHUR of $^{176/177}Hf = 0.282785$ and $^{176}Lu/^{177}Hf = 0.0336$, with an Lu decay constant of $\lambda_{176Lu} = 1.856*10^{-11}$ from ref. [40].

3.5 Acknowledgements - The authors would like to thank Yoan Germain, Alexis de Prunelé and Emmanuel Ponzevera for their technical assistance during Hf and Lu analysis on the Neptune MC-ICP-MS at the Pôle Spectrométry Océan (PSO), Plouzané, France. I.S.F. also thanks Sidonie Revillon for her guidance and advice for chemical separation at the Institut Universitaire Européen de la Mer, Plouzané, and Victoria Bennett for comments on this work. The authors thank landowners MTPA and SAPPI for allowing access to their properties for sample acquisition and field work.

Funding - This work was supported through a LabexMER International Research Chair to A.K.T., funded through the "Laboratoire d'Excellence" LabexMER (ANR-10-LABX-19) and co-funded by a grant from the French government under the program "Investissements d'Avenir". A.K.T. was also supported by a NSF EAR Low-Temperature Geochemistry award 15422113. C.H. was funded through DFG grants He2418/14-1 and He2418/17-1. I.S.F. acknowledges support from the Region of Brittany “Allocations de recherche doctorale”.

3.6 References

1. Flament, N., Coltice, N. & Rey, P. F. The evolution of the 87Sr/86Sr of marine carbonates does not constrain continental growth. *Precambrian Res.* **229,** 177–188 (2013).
2. Albarède, F., Simonetti, A., Vervoort, J. D., Blichert-Toft, J. & Abouchami, W. A Hf-Nd isotopic correlation in ferromanganese nodules. *Geophys. Res. Lett.* **25,** 3895–3898 (1998).
3. Merschel, G., Bau, M., Schmidt, K., Münker, C. & Dantas, E. L. Hafnium and neodymium isotopes and REY distribution in the truly dissolved, nanoparticulate/colloidal and suspended loads of rivers in the Amazon Basin, Brazil. *Geochim. Cosmochim. Acta* **213,** 383–399 (2017).
4. Bindeman, I. N. *et al.* Rapid emergence of subaerial landmasses and onset of a modern hydrologic cycle 2.5 billion years ago. *Nature* **557,** 545–548 (2018).
5. Viehmann, S., Hoffmann, J. E., Münker, C. & Bau, M. Decoupled Hf-Nd isotopes in Neoarchean seawater reveal weathering of emerged continents. *Geology* **42,** 115–118 (2014).
6. Vervoort, J. D., Patchett, P. J., Blichert-Toft, J. & Albarède, F. Relationships between Lu–Hf and Sm–Nd isotopic systems in the global sedimentary system. *Earth Planet. Sci. Lett.* **168,** 79–99 (1999).
7. Vervoort, J. D., Plank, T. & Prytulak, J. The Hf–Nd isotopic composition of marine sediments. *Geochim. Cosmochim. Acta* **75,** 5903–5926 (2011).
8. Bayon, G. *et al.* The control of weathering processes on riverine and seawater hafnium isotope ratios. *Geology* **34,** 433–436 (2006).

9. Bau, M. & Dulski, P. Distribution of yttrium and rare-earth elements in the Penge and Kuruman iron-formations, Transvaal Supergroup, South Africa. *Precambrian Res.* **79,** 37–55 (1996).

10. Konhauser, K. O. *et al.* Iron formations: A global record of Neoarchaean to Palaeoproterozoic environmental history. *Earth Sci. Rev.* **172,** 140–177 (2017).

11. Viehmann, S., Bau, M., Hoffmann, J. E. & Münker, C. Decoupled Hf and Nd isotopes in suspended particles and in the dissolved load of Late Archean seawater. *Chem. Geol.* **483,** 111–118 (2018).

12. Tice, M. M., Bostick, B. C. & Lowe, D. R. Thermal history of the 3.5–3.2 Ga Onverwacht and Fig Tree Groups, Barberton greenstone belt, South Africa, inferred by Raman microspectroscopy of carbonaceous material. *Geology* **32,** 37–40 (2004).

13. Homann, M. *et al. Microbial life and biogeochemical cycling on land 3,220 million years ago*. *Nature Geoscience,* **accepted manuscript,** (2018).

14. Heubeck, C. *et al.* Timing of deposition and deformation of the Moodies Group (Barberton Greenstone Belt, South Africa): Very-high-resolution of Archaean surface processes. *Precambrian Res.* **231,** 236–262 (2013).

15. de Ronde, C. E. J. & Kamo, S. L. An Archaean arc-arc collisional event: a short-lived (ca 3 Myr) episode, Weltevreden area, Barberton greenstone belt, South Africa. *S. Afr. J. Sci.* **30,** 219–248 (2000).

16. Bontognali, T. R. R., Fischer, W. W. & Föllmi, K. B. Siliciclastic associated banded iron formation from the 3.2Ga Moodies Group, Barberton Greenstone Belt, South Africa. *Precambrian Res.* **226,** 116–124 (2013).

17. Hayashi, T., Tanimizu, M. & Tanaka, T. Origin of negative Ce anomalies in Barberton sedimentary rocks, deduced from La–Ce and Sm–Nd isotope systematics. *Precambrian Res.* **135,** 345–357 (2004).

18. Alexander, B. W., Bau, M. & Andersson, P. Neodymium isotopes in Archean seawater and implications for the marine Nd cycle in Earth's early oceans. *Earth Planet. Sci. Lett.* **283,** 144–155 (2009).

19. Zeh, A., Gerdes, A. & Heubeck, C. U–Pb and Hf isotope data of detrital zircons from the Barberton Greenstone Belt: constraints on provenance and Archaean crustal evolution. *Journal of the Geological Society* **170,** 215–223 (2013).

20. Garçon, M. *et al.* Erosion of Archean continents: The Sm-Nd and Lu-Hf isotopic record of Barberton sedimentary rocks. *Geochim. Cosmochim. Acta* **206,** 216–235 (2017).

21. Bayon, G. *et al.* Hf and Nd isotopes in marine sediments: Constraints on global silicate weathering. *Earth Planet. Sci. Lett.* **277,** 318–326 (2009).

22. Zhao, W. *et al.* Hf-Nd isotopic variability in mineral dust from Chinese and Mongolian deserts: implications for sources and dispersal. *Sci Rep* **4,** 1–6 (2014).

23. Bayon, G. *et al.* Environmental Hf–Nd isotopic decoupling in World river clays. *Earth Planet. Sci. Lett.* **438,** 25–36 (2016).

24. Hessler, A. M. & Lowe, D. R. Weathering and sediment generation in the Archean: An integrated study of the evolution of siliciclastic sedimentary rocks of the 3.2Ga Moodies Group, Barberton Greenstone Belt, South Africa. *Precambrian Res.* **151,** 185–210 (2006).

25. Nabhan, S., Wiedenbeck, M., Milke, R. & Heubeck, C. Biogenic overgrowth on detrital pyrite in ca. 3.2 Ga Archean paleosols. *Geology* **44,** 763–766 (2016).

26. Heubeck, C. & Lowe, D. R. Sedimentary petrography and provenance of the Archean Moodies Group, Barberton Greenstone Belt. *Geol. Soc. Spec. Pap.* **329,** 259–286 (1999).

27. Hessler, A. M., Lowe, D. R., Jones, R. L. & Bird, D. K. A lower limit for atmospheric carbon dioxide levels 3.2 billion years ago. *Nature* **428,** 736–738 (2004).

28. Simpson, E. L., Eriksson, K. A. & Mueller, W. U. 3.2 Ga eolian deposits from the Moodies Group, Barberton Greenstone Belt, South Africa: Implications for the origin of first-cycle quartz sandstones. *Precambrian Res.* **214-215,** 185–191 (2012).

29. Homann, M., Heubeck, C., Airo, A. & Tice, M. M. Morphological adaptations of 3.22 Ga-old tufted microbial mats to Archean coastal habitats (Moodies Group, Barberton Greenstone Belt, South Africa). *Precambrian Res.* **266,** 47–64 (2015).

30. Altermann, W., Robinson, T., Homann, M., Lalonde, S. V. & Heubeck, C. First find of fossilized raindrop imprints in the Moodies Group (3.2 Ga), Barberton Greenstone Belt, South Africa. *Geol. Soc. S. Afr. Geobull.* **60,** 46–47 (2017).

31. Heubeck, C. & Lowe, D. R. Depositional and tectonic setting of the Archean Moodies Group, Barberton Greenstone Belt, South Africa. *Precambrian Res.* **68,** 257–290 (1994).

32. Kamber, B. S. Archean mafic–ultramafic volcanic landmasses and their effect on ocean–atmosphere chemistry. *Chem. Geol.* **274,** 19–28 (2010).

33. van de Flierdt, T. *et al.* Global neodymium–hafnium isotope systematics — revisited. *Earth Planet. Sci. Lett.* **259,** 432–441 (2007).

34. Jones, C., Nomosatryo, S., Crowe, S. A., Bjerrum, C. J. & Canfield, D. E. Iron oxides, divalent cations, silica, and the early earth phosphorus crisis. *Geology* **43,** 135–138 (2015).

35. Reinhard, C. T. *et al.* Evolution of the global phosphorus cycle. *Nature* **541,** 386–389 (2017).

37. J. Blichert-Toft, C. Chauvel, and F. Albarède, Separation of Hf and Lu for high-precision isotopic analysis of rock samples by magnetic sector-multiple collector ICP-MS. *Contrib. Mineral. Petrol.*, **127**, 248-260 (1997).

38. P. Richard, N. Shimizu, and C. J. Allègre, $^{143}Nd/^{146}Nd$, a natural tracer: An application to oceanic basalts. *Earth Planet. Sci. Lett*., **31**, 269-278 (1976).

39. J. Blichert-Toft, and I. S. Puchtel, Depleated mantle sources through time: Evidence from Lu-Hf and Sm-Nd isotope systematics of Archean komatiites. *Earth Planet. Sci. Lett*., **297**, 598-606 (2010).

40. K. H.Wedepohl, The Composition of the continental crust*. *Geochim. Cosmochim. Acta,* **59**, 1217-1232 (1995).

41. A. Bouvier, J. D. Vervoort, and P. J. Patchett, The Lu-Hf and Sm-Nd isotopic composition of CHUR: Constraints from unequilibrated chondrites and implications for the bulk composition of terrestrial planets. *Earth Planet. Sci. Lett*., **273**, 48-57 (2008).

Chapter 4: Neoproterozoic BIF records riverine input and supports periods of a Slushball-Earth during the Sturtian Glaciation

4.1 Abstract

The concept of global glacial events, so-called “Snowball Earths”, first proposed by Hoffman et al. (1998), was initially a highly contested hypothesis, but has since gained nearly global acceptance in the scientific community. However, much still remains to be determined about the intensity and longevity of these proposed glacial events, and whether they were truly global in extent. Our study sheds light on whether or not these Snowball Earth events represented periods of complete global ice coverage, or if there were potential oases were regional conditions permitted intermittent ice-thaw and conditions that are more consistent with recently proposed ‘slushball’ Earth interpretations. Here we present εHf-εNd data for the Braemar iron formation located in south-central Australia, which seems to suggest periods of glacial retreat and the weathering of exposed continental surfaces prior to the deposition of the global cap-carbonates that indicate the end of the Sturtian glaciation ~720 Ma ago. Our εHf data range in value from + 19.1 to – 8.7, and are clustered into three groups, remarkably similar to recently measured εHf values observed by Rickli et al. (2017) in modern glacial and non-glacial rivers and lakes located in Greenland. Our results lend further evidence to previous sedimentological studies of this region by Le Heron et al. (2011) that suggest open ocean conditions existed prior to the end of the Sturtian glaciation, and intriguingly, may also indicate that the presence of possible oases where life had ample access to light and nutrients, potentially contributing to the astounding diversification of multicellular life recorded during and after the Cryogenian period of Earth’s history.

4.2 INTRODUCTION

Modern day weathering of the Earth's emerged continental land mass is known to produce a distinct pattern in the εHf vs εNd signature of modern oceanic sediments. Specifically, detrital materials have been found to produce a coeval trend in both εHf and εNd known as the terrestrial array (Vervoort et al, 2011; Zhao et al. 2014, Bayon et al. 2009; Bayon et al., 2016), while chemically precipitated sediments capture a distinctly different trend, with more radiogenic εHf values for any given εNd value, producing the so-called seawater array (Albarède et al., 1998). The differences in these two trends are now known to be the result of differential weathering under subaerial conditions where vulnerable minerals such as apatite and sphene are preferentially weathered over highly resistant minerals such as zircon. This differential weathering ultimately leads to a decoupling of εHf from εNd values in river waters and seawater due to the preferential release of radiogenic Hf from these easily weathered minerals, and the retention of non-radiogenic Hf in highly resistant phases (zircons), a signal which can then be captured by chemical sediments (for a full review of εHf systematics see Viehmann et al., 2018). To date the differences in these two systems has been used to track the type and intensity of subaerial weathering of continents in local and regional settings (Rickli et al. 2009; Godfrey et al. 2009; Zimmermann et al. 2009) due to the moderate residence time of Hf and Nd in ocean waters (approximately 500 - 1500 yrs., (Godfrey et al. 2009; Van de Flierdt et al. 2007). This has allowed authors to trace continental weathering inputs from modern terrestrial sources, as well as infer the existence of emerged continents in the Meso- and Paleoarchean (Viehmann et al. 2014; Viehmann et al. 2015, Foster et al., in review).

The ability to track continental weathering via deposition of chemical precipitates in the ocean offers a unique opportunity to investigate some of the more unusual periods in Earth's history when global and local environmental conditions are poorly constrained at best. One such example are the Earth surface conditions characterizing the Sturtian Glaciation ~720-630 Ma ago, also known as one of the "Snowball Earth" events. To date, multiple studies attest to the presence of glacial depositions in oceanic settings adjacent to continental land masses that were in paleo-tropical zones, i.e. between 30˚ North and South, including positions at or near the equator (Hoffman et al. 1998; Hoffman et al. 2002). At least two Snowball Earth events occurred during the Cryogenian period of the Ediacaran, and while their chronology is well known (e.g. Rooney et al., 2015), however there is still no consensus on the magnitude of these glaciations, specifically if they were total snowball events (Goddéris et al. 2003; Donnadieu et al. 2004) or something more akin to "Slushball" conditions where at least some areas of non-glaciated land and/or ocean remain (Le Heron et al. 2011).

Our study aims to help shed light on surface conditions at this time by examining the Neoproterozoic Iron Formations (IFs) of the Braemar Formation, located in South-Central Australia (Supplementary Information Figure 4.2). The Braemar formation is the lower-most unit of the Umberatana group on the eastern edge of the Adelaide geosyncline, and has experienced at least greenschist-facies metamorphism. The formation itself represents a number of horizons that appear within both the underlying Pualco Tillite, and the overlying Benda Sandstone. Outcrops of the Braemar Formation are typically lenticular or podiform, often only meter-scale to several meters thick, and can be separated by 10's to hundreds of meters of other strata (Lottermoser et al. 2000). The Formation itself is extremely variable and

can be locally found to be represented by anything from an iron-rich-matrix with diamictic clasts and dropstones, to other localities where varying laminated iron-siltstone/iron-carbonates facies exist and the iron-content of the deposit can vary greatly from less than 30% to greater than 80% (Supplementary Information Figure 4.3). The overall paleoenvironment interpreted for these deposits is suggested to be that of iron deposition on a relatively near-shore continental margin (Lottermoser et al. 2000), however recent geological evidence presented by Lechte and Wallace (2015) has suggested that coeval iron formations from the Holowilena locality represent iron-rich debris flows that were deposited into local rifting grabens, suggesting the overall environment of deposition may be that of a passive to newly-opening rift margin. Detailed descriptions of the Braemar Iron Formation and samples used in this study can be found in the Supplementary Information.

4.3 METHODOLOGY

Powdered samples from the Braemar Iron Formation were analyzed for their major element and trace element concentrations after digesting them with $HClO_4$ + HF mixtures and resuspending them in 5% HNO_3 with trace HF and a Tm-spike. Concentrations were measured on an HR-ICP-MS Thermo Element 2 operating in low, medium, and high-resolution mode at the *Pôle Spectrométrie Océan* (PSO), Institut Universitaire Européen de la Mer, Plouzané. These data (found in the supplementary information Tables 4.3, 4.4 and 4.5) were then used to select 10 sub-samples with the highest FeO and lowest Zr concentrations, intended to represent the least detritally contaminated samples, and therefore most “oceanic” endmembers, for further analysis. Nd isotopes were determined from 70–90 mg of sample powder digested in concentrated HF + HNO_3, purified through a two-column procedure modified after Richard et

al. (1976), and analyzed on the MC-ICP-MS Neptune and TIMS Triton at the PSO against the JNdi-1 standard.

Hf isotopes were analyzed by digesting ~ 0.5 g of BIF sample in concentrated HF + HNO_3, followed by a modified 2-column Hf and Zr purification, as outlined by Blichert-Toft et al. (1997), followed by a two-column separation for Nd, Sm, Yb and Lu, and analysis on a Neptune MC-ICP-MS at Pôle Spectrométry Océan (PSO), Plouzané, France. $^{176}Hf/^{177}Hf$ was corrected for Yb and Lu interferences on mass-176, and mass-bias was corrected using multiple bracketing standards: BHVO-2, BCR2 and JMC (for Hafnium), and a P-CAL elemental solution for Lutetium.

Precise determination of Hf and Lu concentrations was achieved after purification (same method as described above) by isotope dilution using ^{179}Hf and ^{176}Lu spiked samples, subsequently measured on the MC-ICP-MS Thermo Neptune at the PSO. $\varepsilon Hf_{(i)}$ and $\varepsilon Nd_{(i)}$ values at the time of BIF deposition were calculated using the following values: $(^{176/177}Hf)_{CHUR}$ = 0.28286, $(^{176}Lu/^{177}Hf)_{CHUR}$ = 0.0334, ^{176}Lu-decay constant $\lambda_{176Lu} = 1.856*10^{-11}$, $(^{143}Nd/^{144}Nd)_{CHUR}$ = 0.512638, $(^{147}Sm/^{144}Nd)_{CHUR}$ = 0.1967, and ^{147}Sm-decay constant $\lambda_{147Sm} = 6.54*10^{-12}$ (Bouvier et al. 2008).

4.4 RESULTS

Similar to previous studies of Archean BIF, our results show $\varepsilon Nd_{(i)}$ values at the time of IF deposition characterized by relatively very little variation, with a range of values from -4.43 to -2.07 and a mean of -4.01 (Table 4.1, sample BR 13 is not included due to inferred resetting of the sample). The large 2σ errors +/- 5.0 to 1 strongly suggest the need for spiked

Nd and Sm to be analyzed prior to publication, which will also allow the determination of an Sm/Nd isochron age for these samples. Contrary to the $\varepsilon Nd_{(i)}$ values, $\varepsilon Hf_{(i)}$ values display a much wider range in initial values, varying from -4.22 to 19.28, with an average value of 2.7 and an average error of 0.15 (Table 4.2). Intriguingly, compared to other Archean BIF deposits these samples contain a wide range of Hf concentrations from ~ 600 to 2600 ppb, and Lu concentrations from 130 to ~ 470 ppb, making them 10-100 times more enriched in Hf and Lu compared to previously studied BIFs. Major and trace elements were also analyzed, the data for which can be found in the Supplementary Materials (Tables 4.3 and 4.4A-D respectively).

Sample ID	Sample Locality Braemer NIF 720 Myr	Nd Concentration (ppm)	± 2σ	Sm Concentration (ppm)	± 2σ	Modern $^{147}Sm/^{144}Nd$	± 2σ	Modern $^{143}Nd/^{144}Nd$	± 2σ	εNd at 720 Myr	± 2σ
BR 8	Iron Peak	10.80	1.11	2.02	0.23	0.118013	0.01217	0.51213	0.00001	-2.59	1.59
BR 13	Razorback Ridge	6.41	1.11	1.45	0.23	0.142205	0.02173	0.51266	0.00001	5.40	7.25
BR 25	Razorback Ridge	19.91	1.11	4.02	0.23	0.127014	0.00697	0.51203	0.00001	-5.41	4.97
BR 35	Bimbowrie Hill	25.93	1.11	5.10	0.23	0.124000	0.00532	0.51209	0.00001	-4.02	3.73
BR 36	Bimbowrie Hill	22.90	1.11	4.80	0.23	0.131875	0.00620	0.51207	0.00001	-5.12	4.71
BR 40	Oultalpa	6.76	1.11	1.43	0.23	0.133025	0.02005	0.51208	0.00001	-5.05	3.40
BR 44	Mt. Mulga	23.01	1.11	4.66	0.23	0.127686	0.00607	0.51210	0.00001	-4.21	3.76
BR 48I	Razorback Ridge	12.29	1.11	2.36	0.23	0.120808	0.01087	0.51205	0.00001	-4.43	3.59
BR 52	Braemar	17.83	1.11	4.08	0.23	0.123921	0.00884	0.51213	0.00001	-3.20	2.54
BR 53	Braemar	17.37	1.11	3.85	0.23	0.139695	0.00835	0.51226	0.00001	-2.07	1.46

Table 4.1 Neodymium/Samarium concentrations and epsilon values (calculated for 720 My) for the Neoproterozoic Braemar Iron Formation.

Sample ID	Sample Locality Braemer BIF 720 Myr	Hf Concentration (ppb)	± 2σ	Lu Concentration (ppb)	± 2σ	Modern $^{176}Lu/^{177}Hf$	± 2σ	Modern $^{176}Hf/^{177}Hf$	± 2σ	εHf at 720 Myr	± 2σ
BR 8	Iron Peak	1430.52	0.17	150.26	0.05	0.01	0.00000	0.28275	0.00001	7.84	0.25
BR 13	Razorback Ridge	1958.77	0.35	93.30	0.38	0.01	0.00003	0.28267	0.00001	8.71	0.22
BR 25	Razorback Ridge	1648.16	0.25	191.50	1.17	0.02	0.00010	0.28260	0.00001	1.74	0.20
BR 35	Bimbowrie Hill	1255.74	0.17	236.95	0.12	0.03	0.00001	0.28273	0.00000	1.71	0.13
BR 36	Bimbowrie Hill	2621.43	0.72	467.78	0.22	0.02	0.00001	0.28244	0.00000	-8.11	0.10
BR 40	Oultalpa	605.90	0.05	130.91	0.05	0.03	0.00001	0.28273	0.00001	-0.31	0.18
BR 44	Mt. Mulga	2475.42	0.28	276.47	6.12	0.02	0.00034	0.28258	0.00000	1.54	0.06
BR 48I	Razorback Ridge	1946.71	0.26	335.94	0.13	0.02	0.00001	0.28253	0.00000	-4.41	0.08
BR 52	Braemar	1814.06	1.39	218.84	1.47	0.02	0.00010	0.28264	0.00001	2.98	0.21
BR 53	Braemar	1118.03	0.06	197.11	0.84	0.02	0.00010	0.28320	0.00000	19.10	0.10

Table 4.2 Hafnium/Lutetium concentrations and epsilon values (calculated for 720 My) for the Neoproterozoic Braemar Iron Formation.

4.5 Discussion

Samarium-Neodymium isotope data for the Braemar Iron Formation show near mantle values, however this is difficult to determine given the uncertainties, as they may also be interpreted as having some influence from continental sources, given that all values are negative, but only slightly. Preliminary errorchrons produced using this Sm-Nd data yields an age of ~724 Ma +/- 25, while Lu-Hf data values are far too disparate to produce any coherent errorchron at all. We suggest that this may be a result of deposition in the passive-to-active margin setting of the Braemar formation, and that these two findings can both be reconciled by depositional processes.

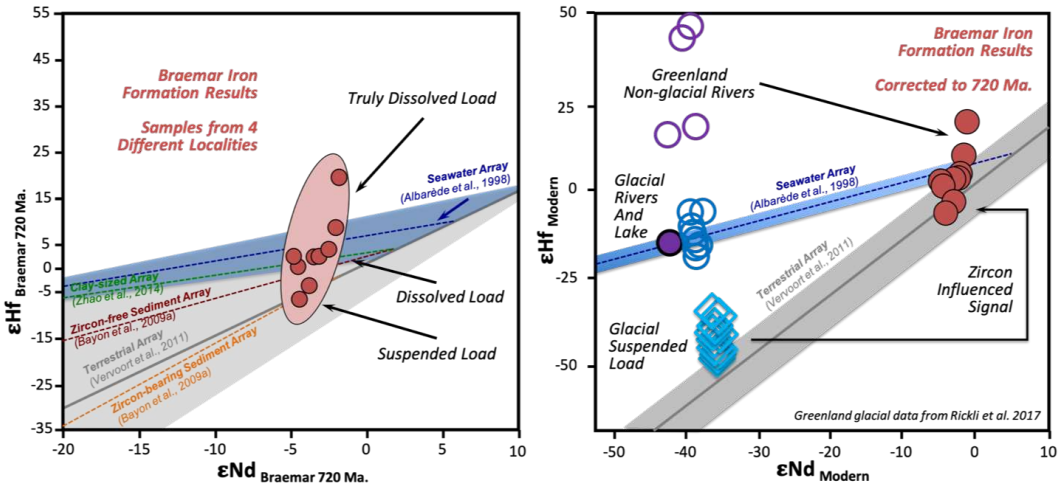

Figure 4.1: (Left Panel) εNd and εHf values calculated for the known age of deposition, compared to the modern seawater array. Results show a spread of values from the terrestrial array to well above the seawater array, suggesting a mixing from glacial to non-glacial riverine input in these Iron formations. (Right Panel) Modern εNd and εHf values taken from Greenland continental rivers (open purple circles), a glacial lake (closed purple circle), glacial-rivers (open blue circles) and glacial suspended load (open blue diamonds), compared with the values observed in the Braemar Formation (closed red circles).

In the case of Nd, both Sm/Nd and $\varepsilon Nd_{720\ Ma}$ are relatively restricted in this sample set (within uncertainty), despite clear source effects as revealed by the εHf data (see below). This might be explained by the congruent weathering of Sm- and Nd- bearing minerals, the source averaging effect of glaciation over significant areas of landmass, and the possibility that the Nd isotope composition of local seawater during the deposition of iron formations was largely a reflection of detrital inputs of similar Nd isotope composition. The narrow range in Sm/Nd and $^{143}Nd/^{144}Nd$ ratios, combined with higher-than-desired error on Sm/Nd as isotope dilution was not performed, both might explain the significant uncertainty (+/- 25) on the 726 Ma Nd errorchron age, which in itself is otherwise consistent with the known depositional age of 720 Ma (Lottmoser et al. 2000).

With regard to the Lu-Hf isotope data, a much simpler explanation can be invoked. Given that these samples are not pure iron-formations, but rather iron-formations combined with either glacial diamictites, or glacial varve-like pulses of terrestrial sediments (Lottmoser et al. 2000), they contain a variety of signals from both predominantly marine sources, as well as varying degrees of contamination from terrestrial sources, namely suspended zircons and the truly dissolved components of riverine runoff (Merchel et al. 2017). The combination of both Lu-Hf derived from continental weathering, as well as the truly dissolved fraction of Hf imparted onto oceanic waters, supplemented with the addition of Hf derived from zircons, can easily explain the highly variable εHf values and impossibility of producing a coherent isochron for these samples.

Sedimentary and Fe-isotope data (Lottmoser et al. 2000) clearly indicate a marine origin for our samples, while the εHf compositions reported here reveal a distinctly continental signature. Our data, uncertain in εNd space, carry a continental weathering signature that is similar to those reported from studies of continental and riverine deposits in recent years (Rickli et al., 2013; Merchel et al., 2017), specifically with regards to the generation of both very positive εHf vales and very negative εHf values during transport in riverine environments.

Given that our samples come from a period in Earth's history where mass glaciation predominated the surface climatic conditions on our planet, the results of Rickli et al. (2017) are perhaps the most relevant. These authors observed a three-fold separation of εHf values based on water samples taken from rivers originating at glacial-fed sources, compared to rivers that did not have glacial headwaters, but merely flowed through glacial deposits. Specifically, waters that had a glacial origin (i.e. those discharging from glacial ice) fell into two categories: those that had εHf values that were moderately positive to moderately negative, and those that had extremely negative εHf values, directly correlated to the dissolved and suspended load of these rivers, respectively. In turn, both are thought to be related to the extended duration of water-rock interaction under the glacier, where more resistant phases carrying non-radiogenic Hf would have time to interact with the water before the short discharge period in the spring/summer. Conversely, rivers that did not have an obvious glacial source were observed to have extremely positive εHf values. This stark difference in εHf values from the surrounding glacially derived rivers has been interpreted to represent the very short water-rock interaction times combined with fine-grain sizes where only the most vulnerable mineral phases (i.e. those

with high initial Lu values, typically those most susceptible to physical and chemical weathering) have a chance to interact with concurrent weathering mechanisms on short time scales (days to weeks per year). This mechanism is an attractive explanation for the origin of divergent riverine signals that carry both εHf values derived from both the most weathering-resistant and weathering-vulnerable minerals (Rickli et al. 2017).

Our new data from the Braemar formation mirror these observations very closely, in that they display all three of these glacial runoff traits, albeit in a potentially more condensed εNd space. Our data suggest that at the time of formation, the various localities of the Braemar iron formation sampled several different sources of glacial-riverine εHf derived from the erosion of different Hf-bearing minerals. Sites where the Braemar εHf values are low (-9 to -4) thus represent areas where subglacial melt waters were entering the ocean directly while carrying a suspended load of sediment, including very fine particles of zircon. Locations where εHf values range from +1.5 to +3 appear to represent coastal areas where glacial streams had some degree of sedimentary sorting occurring, resulting in only the adsorbed-dissolved Hf load reaching areas of iron formation deposition, while finally, samples with the highest εHf (+7.5 to +19) represent areas where totally deglaciated regions of continental material were rapidly weathering and imparting a very positive εHf value directly into adjacent ocean waters with little or no interaction with glacially-derived melt waters.

These data place a constraint on local climate parameters present during the deposition of these iron deposits. Specifically, the fact that the Braemar formation lies below the Sturtian cap-carbonate, a carbonate formation thought to indicate the onset of a terminal global

deglaciation event, suggests that the Sturtian glaciation was not at all times a "Hard" glacial event, where every meter of the Earth was covered in solid ice and snow. Rather, our results suggest that the glaciation was a "softer" one, at least at the time when the Braemar Iron Formation was deposited, and suggests that at least regional conditions, if not global conditions, were more representative of a "Slushball-Earth" then a "Snowball-Earth". In fact, these observation support recent models that suggest the Neoproterozoic glaciations were influenced by, and subject to, alterations in Earth's orbital parameters which may have induced periods of glacial retreat and advance, even during a global glacial event (Le Heron et al. 2015). These results further suggest that Snowball Earth events may not necessarily isolate the land surface from the terrestrial biosphere nor the ocean surface from sunlight, but rather, that important extents of deglaciated niches existed for biological colonization. That Snowball Events were not entirely detrimental to Earth's evolving biosphere makes sense in the context of recent biomarker evidence showing rapid proliferation of eukaryotic life between the Sturtian and Marinoan Snowball Earth events (Brocks et al., 2017).

4.6 Conclusion

The Braemar Iron Formation from South-central Australia is ideally placed to shed light on an enigmatic potion of Earth's history ~720 Ma ago, when the entire planet appears to have been in a state of global glaciation. Our new εHf data, the result of which can only be explained by differential weathering on a subaerial continental land mass, combined with the stratigraphic location of the Braemar deposits below the global cap-carbonate, suggest that the Earth's surface was not completely frozen when these iron deposits formed, and that at least regional areas of respite remained. Given that the Neoproterozoic glaciations were a period of extreme

climate change, seemingly accompanied with the flourishing of eukaryotic organisms, the presence of thin-ice, and possibly even temperate oases during this period, presents an intriguing insight into how life may have survived and diversified during this period of near-global glaciation.

4.7 Supplementary information

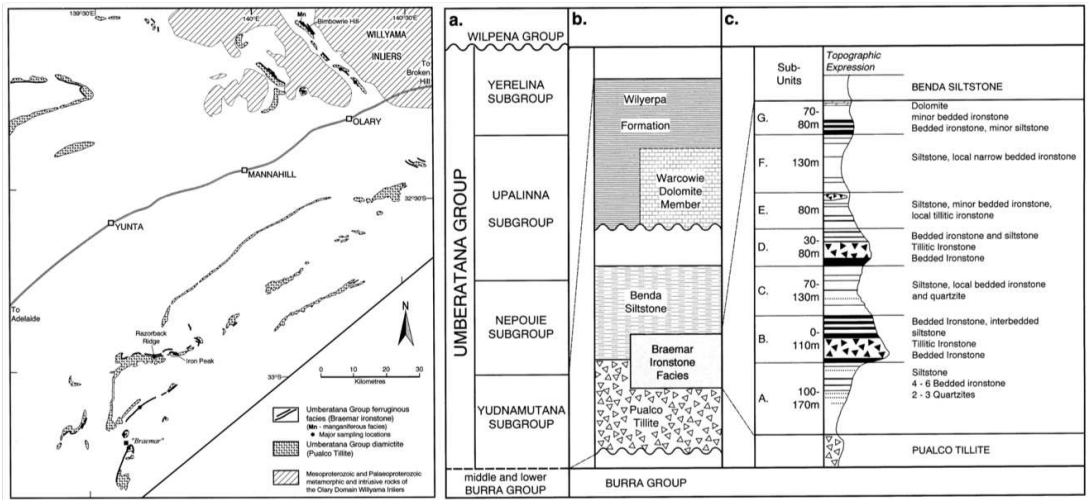

Figure 4.2 (Left panel) Geographical location of outcrops and sampling sites of the Braemar Formation in South-central Australia. (Right panel) Stratigraphic column of the Neoproterozoic Braemar Ironstones. The column highlights the paucity in the IF formation as well as its close association with glacially derived sediments. *From Lottermoser and Ashley (2000).*

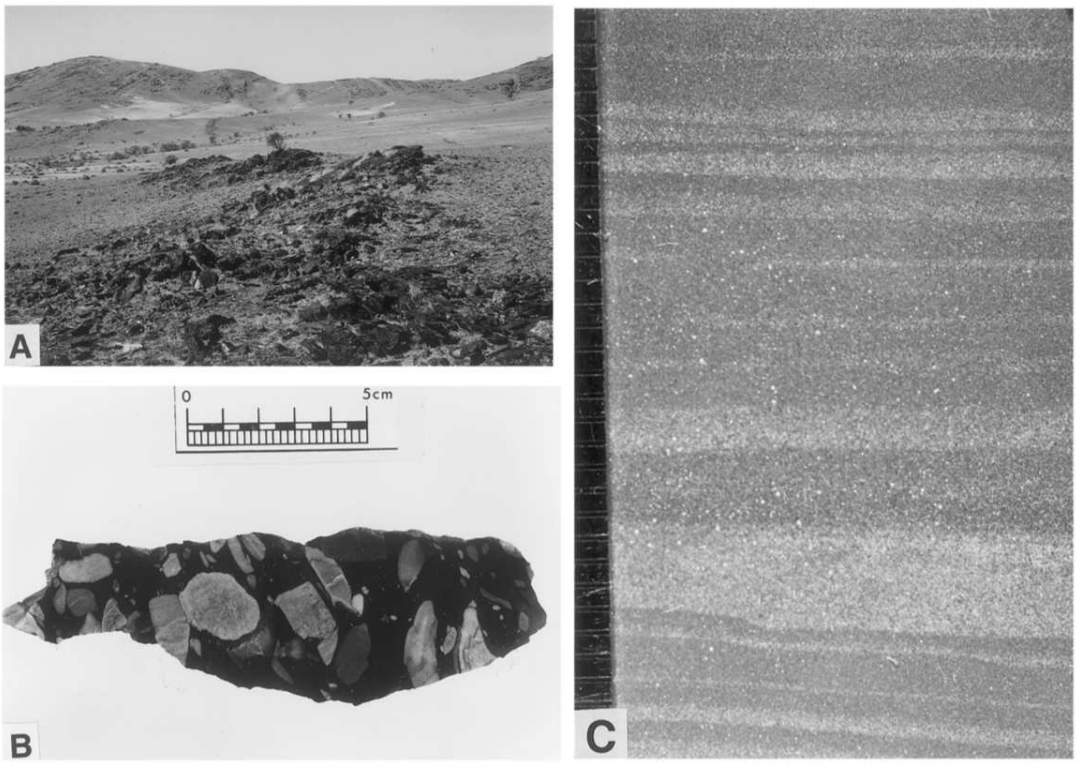

Figure 4.3 (A) Typical outcrops of the Braemar Ironstone formation, highlighting its irregular shape/thickness, podiform nature and rapid transition from and to other glacial sedimentary facies. (B) A dramatic example of a Braemar Ironstone with large diamictic clasts suspended in a primally iron-oxide matrix. (C) Example of finely laminated iron-oxide and fine-grained detrital sedimentary materials in the Braemar Iron Formations illustrating the range of lithologies possible. *From Lottermoser and Ashley (2000).*

4.7.1 Detailed Description of the Braemar Iron Formation

The Braemar iron formation is located in the south Australian Adelaide Geosyncline, a Neoproterozoic to Cambrian age sedimentary basin comprising one of the most complete and well-preserved Neoproterozoic successions, including evidence for two major glacial successions (Lottermoser and Ashley, 2000). The ironstones, part of the Umberatana group, are found in two stratigraphically continuous units of the Yudnamutana subgroup, the lower Pualco Tillite, and the overlying Benda Siltstone. In the Yunta area, 4 to 6 lenticular ironstone

units are observed to grade into both the diamictites and siltstones, and prominent ironstone outcrops are interbedded with diamictites, carbonate-rich rocks, quartzites, siltstones and manganiferous siltstones. Generally, the Braemar iron formations consist of lenticular, laminated, and diamictic ironstones interbedded with calcareous or dolomitic siltstones and thin quartzite units, and can be subdivided into two facies, the diamictic and the laminated ironstones, which are macroscopically different but compositionally identical (Lottermoser and Ashley, 2000). Laminated ironstones and the matrix of the diamictic ironstones are fine-grained and composed of primarily of magnetite, hematite and quartz, with minor muscovite, chlorite, biotite, carbonate, apatite, plagioclase and tourmaline. The lamination is generally well developed, with laminae defined by the relative abundance of magnetite and hematite, ranging from ~80 to 20 wt.%. Detrital mineral grains and lithic clasts occurring in both units are angular to sub-rounded and are composed of quartz, carbonate, plagioclase, K-feldspar, muscovite, tourmaline, foliated sediments, siltstones, quartzites and quartzofeldspathic rocks. In contrast, diamictic ironstones are massive and contain clasts ranging in size from 10 mm to 1.2 m, with similar angularity and rounding to the lithic clasts found in laminated ironstones.

Laminated ironstones can exhibit large variations in modal proportions of rock-forming minerals and Fe-oxides, with lamina displaying both sharp and gradational transitions to siltstone layers, in the latter case magnetite is observed to decrease while quartz and silicate content increase. Sedimentary structures are also present locally and include cross-laminations, microfaulting, piercement of laminae and micro- to meso-scale folding suggesting soft sediment deformation may have occurred. Since deposition the Braemar ironstones have undergone greenschist facies regional metamorphism and deformation, experiencing temperatures of ~360-400˚C, as indicated by chlorite composition (Lottermoser and Ashley, 2000).

The major oxide components of the laminated ironstones are SiO_2 and Fe_2O_3, comprising >70 wt.% of the rock. Minor constituents (expressed as oxides) include Al_2O_3, ranging from 0.28 to 10.64 wt.%, as well as CaO, K_2O, MgO, and Na_2O, variations in which tend to be correlated with Si content, and suggest the addition of plagioclase, carbonate, biotite, chlorite and muscovite. Trace element constituents of the ironstones show large-scale variations dependent on type and quantity of minerals present. They are depleted in most transition metals (Sc, V), high field strength elements (Nb, U, Th, Zr, Hf, Pb, LREE), and large ion lithophile elements (Ba, Sr, Rb) compared to upper continental crust. Weak correlations of Fe with several elements including As, Cu, Sb, V and Zn suggest a hydrothermal or seawater scavenging source of these elements. In short, many of the the Braemar ironstones represent chemical sediments with a minimal to significant contribution from detrital materials (Lottermoser and Ashley, 2000).

All ironstones were found to display REE patterns with variable LREE depletions, negative Ce anomalies and no Eu anomalies, with the exception of one sample which exhibited a distinct positive Eu anomaly. From these data the Braemar ironstones have been subdivided into two different suites, siliceous-aluminous ironstones if SiO_2 >40 wt.% and Al_2O_3 > 6 wt.% and silica-alumina-poor if SiO_2 <40 wt.% and Al_2O_3 <6 wt.%. Silica-alumina-poor samples were found to have low concentrations of REE with moderate depletion of LREE and either depletion or enrichment of HREE. Siliceous-aluminous ironstones display REE patterns only slightly depleted in LREE. The similarity of the REE patterns of Braemar siltstones and siliceous-aluminous ironstones suggests that these sediments gained their REE patterns from detrital sources, however, a different REE source is implicated for the silica-alumina-poor

samples where REE was gained during chemical precipitation from seawater (Lottermoser and Ashley, 2000).

Braemar ironstone facies show positive correlations of Al and Si with Ti, Ca, Mg, K, Ga, Hf, Rb, Sc, Sr, Ta, Th, Zr, La, and Ce, indicating that these elements were all or partially derived from detrital sources. When plotted on a detrital-chemical sediment mixing curve, the ironstones cluster toward the chemical sediment endmember. REE's in the silica-alumina-poor samples (closest to the chemical sediment end member) differ enough from detrital sediment values that they are considered to be consistent with oceanic values, similar to those obtained for modern coastal seawaters.

Associated dolostones capping the Braemar facies (interpreted as inorganic cold-water deposits), as well as from ferroan dolomite and ferroan calcite within siltstones and ironstones, have been analyzed and are considered to provide paleoenvironmental information on the postglacial marine transgressional environment. Carbon and oxygen isotope information from 15 samples selected from material displaying no petrographic evidence of carbonate mobilization or veining from within the Braemar facies display widely variable carbon isotope values ($\partial^{13}C_{PDB}$ -5.5 to +0.9‰, however most are negative), and oxygen values ranging from $\partial^{18}O_{SMOW}$ +10.6 to +29.5‰, which coincide with other values interpreted as support for major Neoproterozoic glaciations.

As indicated by stratigraphic, sedimentological, and carbon/oxygen isotope data, glaciation played an important role in the formation of the Braemar ironstones. The occurrence of detrital fragments in laminated ironstones and the formation of diamictic-ironstones suggests the Braemar ironstones accumulated in a basin along the border of a glaciated continental

landmass. During glacial episodes the coastal waters were covered in a thick ice-cap, effectively cutting them off from atmospheric oxygen, allowing the underlying ocean to become anoxic (due to decay of organic matter) and allowing hydrothermal iron to accumulate in solution. During the transgressive interglacial periods of the Pualco glacial event, when ice cover retreated, the Fr-rich waters were exposed to oxygen, creating the ironstone deposits as the result of direct chemical oxidation of Fe in seawater, allowing the contemporaneous deposition of dropstones and clastic debris filled laminated ironstones on the seafloor. As underlined by the marine-like REE signatures of silica-alumina-poor samples, and the hydrothermal signature of Fe, the Braemar ironstones were deposited in an oceanic environment rather than a lacustrine environment, as had been suggested by previous authors (Lottermoser and Ashley, 2000).

Table 4.3: Major Elements for the Braemar Iron Formation

Braemar Iron Formation											
Major Elements (Wt%)											
Sample Locality	Sample ID	SiO_2	TiO_2	Al_2O_3	Fe_2O_3	MnO	MgO	CaO	Na_2O	K_2O	P_2O_5
Iron Peak	BR 8	28.20	0.22	3.08	65.02	0.01	0.87	0.24	N/D	0.77	0.33
Razorback Ridge	BR 13	29.24	0.33	4.17	61.82	0.04	1.41	0.62	1.00	0.28	0.33
Razorback Ridge	BR 25	34.33	0.42	4.46	55.99	0.02	2.02	0.56	0.41	0.54	0.31
Bimbowrie Hill	BR 35	26.99	0.22	3.06	64.56	0.58	0.35	0.55	0.17	0.73	0.42
Bimbowrie Hill	BR 36	41.42	0.49	6.12	37.87	0.33	3.21	3.36	1.05	1.80	0.75
Oultalpa	BR 40	15.54	0.19	2.98	77.65	0.09	2.11	0.31	N/D	1.43	0.27
Mt. Mulga	BR 44	36.54	0.39	5.55	46.76	0.05	2.25	3.52	1.19	1.67	0.90
Razorback Ridge	BR 48I	16.68	0.31	3.86	74.58	0.01	1.77	0.79	0.42	0.36	0.46
Braemar	BR 52	34.81	0.37	3.34	51.81	0.18	2.28	3.90	1.16	0.14	0.73
Braemar	BR 53	24.32	0.26	2.96	66.12	0.24	1.61	1.99	0.28	0.21	1.04

Table 4.4 A-D: Trace Element Compositions of the Braemar Iron Formation

A (Top) and B (Bottom)

Braemar Iron Formation											
Trace Elements (ppm)											
Sample Locality	Sample ID	Li	Be	Sr	Y	Zr	Nb	Mo	Cs	Ba	La
Iron Peak	BR 8	11.95	0.84	24.67	8.84	51.29	4.12	0.86	1.37	130.92	10.32
Razorback Ridge	BR 13	11.14	0.55	33.85	12.42	75.97	5.74	0.55	0.71	54.68	5.81
Bimbowrie Hill	BR 35	9.69	1.97	87.42	16.48	52.11	5.92	2.47	1.26	282.53	23.82
Bimbowrie Hill	BR 36	32.66	2.66	163.93	23.71	94.06	9.66	1.06	6.27	262.41	22.77
Oultalpa	BR 40	36.11	0.35	7.52	8.76	26.99	3.76	0.84	3.90	158.56	6.02
Mt. Mulga	BR 44	23.63	1.81	63.55	31.61	88.34	7.79	0.71	6.67	227.58	22.65
Razorback Ridge	BR 48I	18.58	0.66	42.13	12.06	83.46	7.01	0.62	0.81	82.79	13.12
Braemar	BR 52	16.94	0.74	84.74	32.40	42.29	4.01	0.86	0.60	176.12	14.38
Braemar	BR 53	17.18	0.76	88.26	33.99	40.03	4.20	0.88	0.63	183.43	15.03

Braemar Iron Formation											
Trace Elements (ppm)											
Sample Locality	Sample ID	Ce	Pr	Nd	Sm	Eu	Gd	Tb	Dy	Ho	Er
Iron Peak	BR 8	22.34	2.69	10.80	2.02	0.52	1.75	0.23	1.32	0.27	0.83
Razorback Ridge	BR 13	12.73	1.58	6.41	1.45	0.33	1.61	0.26	1.66	0.36	1.12
Bimbowrie Hill	BR 35	47.99	6.38	25.93	5.10	1.13	4.80	0.64	2.95	0.53	1.44
Bimbowrie Hill	BR 36	49.21	5.93	22.90	4.80	1.00	4.65	0.70	3.96	0.77	2.16
Oultalpa	BR 40	12.76	1.63	6.76	1.43	0.35	1.50	0.22	1.24	0.25	0.70
Mt. Mulga	BR 44	49.13	5.92	23.01	4.66	1.03	4.67	0.75	4.66	0.97	2.80
Razorback Ridge	BR 48I	27.99	3.36	12.29	2.36	0.45	1.90	0.28	2.13	0.37	1.15
Braemar	BR 52	34.06	4.15	17.37	3.85	0.89	4.76	0.69	4.22	0.92	2.71
Braemar	BR 53	35.69	4.36	18.47	3.97	0.95	5.00	0.71	4.44	0.96	2.77

C (Top) and D (Bottom)

Braemar Iron Formation											
Trace Elements (ppm)											
Sample Locality	Sample ID	Tm	Yb	Lu	Hf	Ta	W	Pb	Th	U	Sc
Iron Peak	BR 8	2.20	1.08	0.19	1.21	0.31	0.95	1.41	3.64	0.28	4.70
Razorback Ridge	BR 13	2.47	1.42	0.24	1.74	0.50	0.99	1.85	5.76	0.63	5.46
Bimbowrie Hill	BR 35	2.41	1.46	0.24	1.17	0.33	1.83	9.72	5.46	0.96	7.59
Bimbowrie Hill	BR 36	2.56	2.12	0.32	2.33	0.75	1.39	12.46	7.61	1.17	10.58
Oultalpa	BR 40	2.40	0.71	0.11	0.56	0.22	0.14	0.74	2.06	0.50	5.22
Mt. Mulga	BR 44	2.65	2.90	0.44	2.12	0.58	0.68	3.91	6.94	0.94	10.37
Razorback Ridge	BR 48I	2.25	1.34	0.22	1.80	0.51	1.11	3.14	4.75	1.01	7.35
Braemar	BR 52	2.48	2.67	0.42	0.95	0.26	12.04	5.46	4.14	0.83	9.26
Braemar	BR 53	2.45	2.61	0.41	0.89	0.25	11.52	5.37	4.09	0.83	8.79

Braemar Iron Formation											
Trace Elements (ppm)											
Sample Locality	Sample ID	Ti	V	Cr	Mn	Co	Ni	Cu	Zn	Sr	Ga
Iron Peak	BR 8	0.22	76.52	65.73	117.61	4.84	10.31	2.15	25.88	24.85	6.34
Razorback Ridge	BR 13	0.35	88.05	38.16	371.82	29.67	16.50	0.68	31.83	34.58	7.81
Bimbowrie Hill	BR 35	0.23	83.63	54.66	4734.94	18.48	15.60	1.86	41.74	87.87	5.94
Bimbowrie Hill	BR 36	0.52	83.18	86.97	2621.23	11.43	17.00	28.29	48.78	164.32	9.87
Oultalpa	BR 40	0.20	110.18	44.29	736.13	16.74	9.37	3.50	73.45	7.41	7.45
Mt. Mulga	BR 44	0.40	86.56	72.28	388.10	5.42	13.30	1.23	44.09	63.60	9.17
Razorback Ridge	BR 48I	0.32	90.39	34.38	137.81	15.84	16.10	0.64	52.79	43.09	8.34
Braemar	BR 52	0.26	124.16	57.39	1794.24	10.72	11.12	1.60	33.82	85.47	4.64
Braemar	BR 53	0.27	132.81	60.85	1871.20	11.06	11.17	1.67	36.94	90.07	4.91

4.8 References

Albarède, F., Simonetti, A. Vervoort, J.D., Blichert-Toft, J., Aouchami, W., (1998). A Hf-Nd isotopic correlation in ferromanganese nodules. *Geophysical Research Letters,* 25, 3895-3898.

Bayon, G., Burton, K.W., Soulet, G., Vigier, N., Dennielou, B., Etoubleau, J., Ponzevera, E., German, C.R., Nesbitt, R.W., (2009). Hf and Nd isotopes in marine sediments: Constraintes on global silicate weathering. *Earth and Planetary Science Letters,* 277, 318-326.

Bayon, G., Skonieczny, C., Delvigne, C., Toucanne, S., Bermell, S., Ponzevera, E., André, L., (2016). Environmental decoupling in World river clays. *Earth and Planetary Science Letters,* 438, 25-36.

J. Blichert-Toft, C. Chauvel, and F. Albarède, Separation of Hf and Lu for high-precision isotopic analysis of rock samples by magnetic sector-multiple collector ICP-MS. *Contrib. Mineral. Petrol.*, 127, 248-260 (1997).

Brocks, J.J., Jarrett, A.J.M., Sirantoine, E., Hallmann, C., Hoshino, Y., Liyanage, T., (2017). The rise of algae in Cryogenian oceans and the emergence of animals. *Nature,* 548, 578-581.

A. Bouvier, J. D. Vervoort, and P. J. Patchett, The Lu-Hf and Sm-Nd isotopic composition of CHUR: Constraints from unequilibrated chondrites and implications for the bulk composition of terrestrial planets. *Earth Planet. Sci. Lett.*, 273, 48-57 (2008).

Le Heron, D.P., Cox, G., Trundley, A., Collins, A., (2015). Sea ice-free conditions during the Sturtian glaciation (early Cryogenian), South Australia. *Geology,* 39, 31-34.

Lechte, M.A., and Wallace, M.W., (2015). Sedimentary and tectonic history of the Holowilena Ironstone, a Neoproterozoic iron formation in South Australia. *Sedimentary Geology*, 329, 211-224.

Goddéris, Y., Donnadieu, Y., Nédélec, A., Dupreé, B., Dessert, C., Grard, A., Ramstein, G., François, L.M., (2003). The Sturtian 'snowball' glaciation: fire and ice. *Earth and Planetary Science Letters,* 211, 1-12.

Godfrey, L.V., Zimmermann, B., Lee, D.-C., King, R.L., Vervoort, J.D., Sherrell, R.M., Halliday, A.N., (2009). Hafnium and neodymium isotopic variations in NE Atlantic seawater. *Geochemistry, Geophysics, Geosystems*, 10, 1-13.

Hoffman, P.F., Kaufman, A.J., Halverson, G.P., Schrag, D.P., (1998). A Neoproterozoic Snowball Earth. *Science*, 281, 1342-1346.

Hoffman, P.F., and Schrag, D.P., (2002). The snowball Earth hypothesis: testing the limits of global change. *Terra Nova,* 14, 129-155.

B.G. Lottermoser and P.M. Ashley, Geochemistry, petrology and origin of Neoproterozoic ironstones in the eastern part of the Adelaide Geosyncline,
South Australia. *Precambrian Research,* 101, 49-67 (2000).

Merchel, G., Bau, M., Schmidt, K., Münker, C., Dantas, E.L., (2017). Hafnium and neodymium isotopes and REY distribution in the truly dissolved, nanoparticle/colloidal and suspended

loads of rivers in the Amazon Basin, Brazil. *Geochemica et Cosmochimica Acta*, 213, 383-399.

P. Richard, N. Shimizu, and C. J. Allègre, $^{143}Nd/^{146}Nd$, a natural tracer: An application to oceanic basalts. *Earth Planet. Sci. Lett*., 31, 269-278 (1976).

Rickli, J., Frank, M. and Halliday, A.N., (2009). The hafnium-neodymium isotopic composition of Atlantic Seawater. *Earth and Planetary Science Letters*, 280, 118-127.

Rickli, J., Frank, M., Stichel, T., Georg, R.B., Vance, D., Halliday, A.N., (2013). Controls on the incongruent release of hafnium during weathering of metamorphic and sedimentary catchments. *Geochimica et Cosmochimica Acta,* 101, 263-284.

Rickli, J., Hindshaw, R.S., Leuthold, J., Wadham, J.L., Burton, K.W., Vance, D., (2017). Impact of glacial activity on the weathering of Hf isotopes – obbservations from Southwest Greenland. *Geochemica et Cosmochimica Acta,* 15, 295-316.

Rooney, A.D., Strauss, J.V., Brandon, A.D., Macdonald, F.A., (2015). A Cryogenian chronology: Two long-lasting synchronous Neoproterozoic glaciations. *Geology,* 43, 459-462.

Van de Flierdt, T., Goldstein, S.L., Hemming S.R., Roy, M., Frank, M., Halliday, (2007). Global neodymium-hafnium isotope systematics – revisited. *Earth and Planetary Science Letters,* 259, 432-441

Vervoort, J.D., Plank, T., Prytulak, J., (2011). The Hf-Nd isotopic composition of marine sediments. *Geochemica et Cosmochimica Acta,* 75, 5903-5926.

Viehmann, S., Hoffmann, J.E., Münker, C., and Bau, M., (2014). Decoupled Hf-Nd isotopes in Neoarchean seawater reveal weathering of emerged continents. *Geology*, 42, 115-118.

Viehmann, S., Bau, M., Hoffmann, J.E., Münker, C., (2015). Geochemistry of the Krivoy Rog Banded Iron Formation, Ukraine, and the impact of peak episodes of increased global magmatic activity on the trace element composition of Precambrian seawater. *Precambrian Research,* 270, 165-180.

Viehmann, S., Bau, M., Hoffmann, J.E., Münker, C., (2018). Decoupled Hf and Nd isotopes in suspended particles and in the dissolved load of Late Archean seatater. *Chemical Geology*, 483, 111-118.

Zhao, W., Sun, Y., Balsam, W., Lu, H., Liu, L., Chen, J., Ji, J., (2014). Hf-Nd isotopic variability in mineral dust from Chinese and Mongolian deserts: implications for sources and dispersal. *Scientific Reports*, 4, 1-6.

Zimmermann, B., Porcelli, D., Frank, M., Rickli, J., Lee, D.-C., Halliday, A.N., (2009). The Hafnium isotope composition of Pacific Ocean water. *Geochemica et Cosmochemica Acta,* 73, 91-101.

Chapter 5: Results from the Isua, Nuvvuagittuq and Nulliak Iron Formations:

Work in progress…

5.0 Abstract

The earliest records of our planet's history have largely been lost due to the relentless recycling of Earth's crust. Of the sites remaining that preserve Earth's earliest crustal materials, here we focus on three localities that preserve sedimentary deposits, which in turn may record evidence of the environmental and chemical conditions present during one of the most enigmatic periods in Earth history. In this study we investigated the εHf and εNd values of the ~3.8–3.7 Ga Isua banded iron formation, as well as several samples from the ~3.8 Ga Nuvvuagittuq iron formation and ~3.7 Ga Nulliak iron formation, to try and resolve questions regarding the presence or absence of emerged continental crust during the Eoarchean. Metamorphic overprinting appears to have played a considerable role in the evolution of εHf values since the initial deposition of these samples. Our study reveals εHf values from both the Isua and Nuvvuagittuq sites that range from -2130 to +1369, which are difficult to explain without evoking metamorphic overprinting post-deposition. Indeed, these formations have experienced at least one post-depositional metamorphic event that reached amphibolite-facies, capable of generating garnets and zircons. These results lead us to suspect our values represent the result of metamorphic alteration, likely related to the intrusion of granitic plutons early in the history of these deposits. We suggest several possible alterations to our methods that may allow us to discern a more accurate initial εHf and εNd value for these samples that may in turn warrant additional investigation of these samples.

5.1 Introduction

The Isua, Nuvvuagittuq and Nulliak Iron Formations (IF) represent a compelling and intriguing insight into our planet's earliest crustal history. The Isua and Nuvvuagittuq chemical sedimentary deposits are not only considered to be some of the oldest known rocks on our planet, but they are also amongst the oldest known sedimentary deposits found to date. As such, they represent a window into the earliest surface environments found on Earth, specifically during a time when the climatic, oceanic, geologic and atmospheric conditions are highly uncertain due to a lack of preserved material from this time period. Unfortunately, not only is this period of Earth's history masked by the rarity of material dating back to the Eoarchean, much of the material, including the Isua sediments, have been exposed to varying degrees of post-depositional metamorphism, where conditions reached amphibolite-grade conditions of at least 600˚C and moderate to high pressure conducive to the formation of garnets (Rollinson 2003; Polat et al. 2005).

The Isua banded iron formation, part of the Itsaq Gneiss Complex (located approximately 150 km northeast of Godthåb on the western coast of Greenland, Figure 5.1) was initially dated to be 3.70 ± 0.7 Ga (Moorbath et al. 1973), and represents one of the most well-studied chemical sediments deposited in the Earth's Eoarchean ocean.

The regional greenstone belt geology was assembled at about 2750 Ma. ago, combining several different sedimentary and volcanic terrains and resulting in regional metamorphic overprints that range from upper greenschist to amphibolite facies

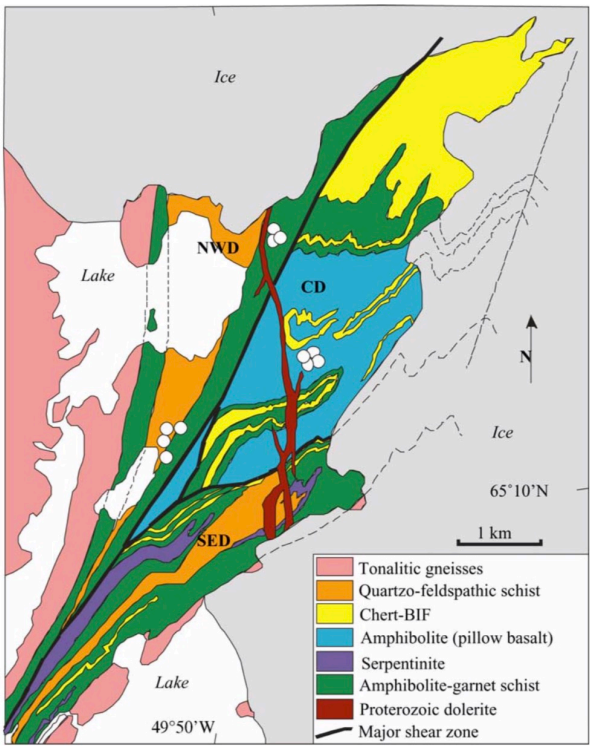

Figure 5.1 : Geological map of the eastern part of the Isua greenstone belt. NWD: northwest tectonic domain; CD: central tectonic domain; SED: southeast tectonic domain, modified from Appel et al. (1998). Open circles show sample locations. *Figure and caption from Polat et al. 2005.*

---

metamorphism (Polat et al. 2005). Initial depositional dates for the BIF are approximately >3.7 Ga ago based on zircon analysis of intrusive tonalites and granitic pegmatite dikes and sheets (Nutman et al. 2007).

The Nuvvuagittuq occurrences of banded iron formation (BIF) and banded silica formation (BSF), located in the northeastern Superior Province of Québec, Canada, on the east coast of the Hudson Bay, are the oldest currently known examples of banded iron chemical precipitates in North America, dating to the Eoarchean (≥ 3.75 Ga), as determined by zircons

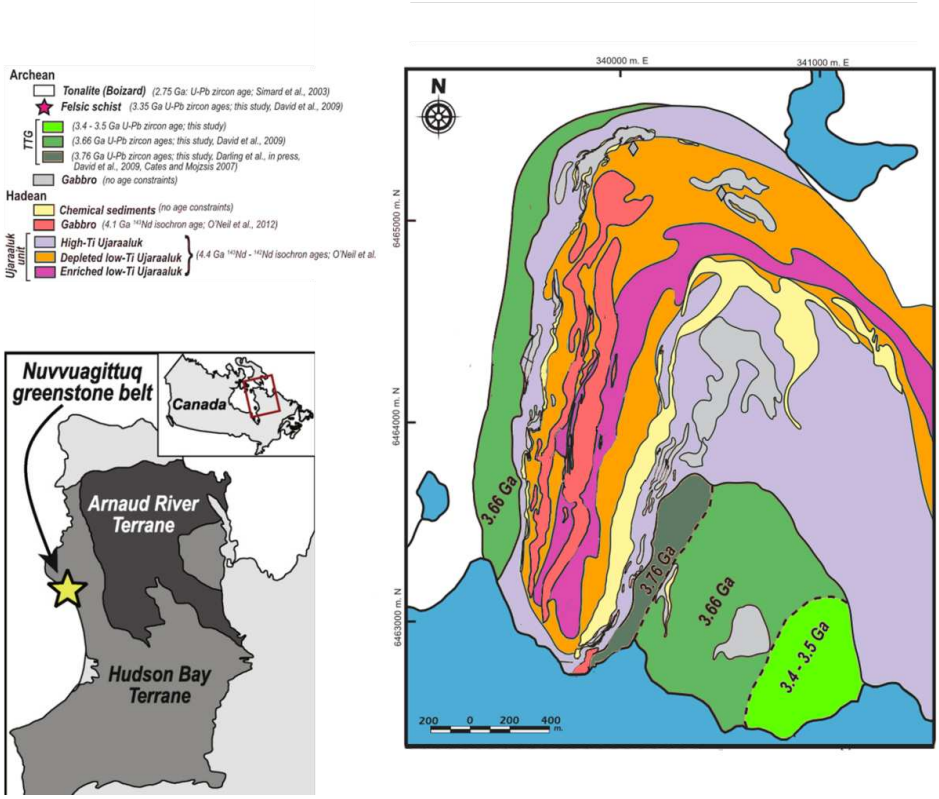

Figure 5.2: Geological map of the Nuvvuagittuq greenstone belt (modified from O'Neil et al. 2011). Yellow regions represent areas where BIF and BSF are found. *Figure and caption from Mloszewska et al., 2012.*

from trondhjemitic gneisses in the Nuvvuagittuq succession (Mloszewska et al., 2012). The Nuvvuagittuq greenstone belt is comprised of an area ~10 km^2, and consists of volcano-sedimentary sequences interspersed with BIF and BSF, located in an isoclinal, north-plunging synform, that has been refolded into an open south-facing synform (Figure 5.2) and experienced extensive retrograde metamorphism from upper amphibolite/lower granulite facies in the east down to greenschist facies in the west, corresponding to maximum temperatures as high as ~640˚C for the eastern sections of this succession (O'Neil et al. 2011, Mloszewska et al., 2012). The BIF are composed of 5-30 meter-wide units of alternating magnetite and grunerite bands with variable amounts of finely layered quartz, which outcrop continuously in the west and discontinuously in the east. BSF are located 50 m up section from

the BIFs and outcrop continuously in the western limb of the fold, consisting of Fe-Ca-Mg silicates with quartz bands, which grade into a 100 m wide cherty unit of recrystallized quartz and disseminated pyrite (Mloszewska et al., 2012).

Finally, the Nulliak banded iron formation is part of the Eoarchean-age Saglek Block of northeastern Labrador, Canada, occurring predominantly on the island of Nulliak and its near-shore counterpart. This formation is separated into two suites of rocks based on their crosscutting relationship with Mesoarchean dykes. Of interest here are those units designated as Eoarchean supracrustal rocks which are comprised of chemical and clastic sediments, amphibolites and ultramafic rocks. Though initially controversial, dating of zircons found in the underlying units of the Uivak Gneisses have now been examined by cathodoluminescence, and determined to have formational ages of >3.95 Ga, after which, this region underwent at least one episode of granulite to amphibolite facies metamorphism at approximately 2.7 – 2.8 Ga. The banded iron formations are regarded as the oldest chemical sedimentary rocks of this sequence and sporadically outcrop across the entire Saglek Block, occurring as thin layers < 5m to up to 32 meters in height, that fade out over 10's to 100's of meters (Komiya et al. 2015).

The rarity of these locales, and previous research that suggests that these primordial samples still retain primary Rare Earth Element compositions (REE) typical for seawater throughout the Archean (Moorbath et al. 1973), make their study an important avenue for investigation into surface conditions on the early Earth. In this study we examined the Sm-Nd and Lu-Hf isotope compositions of samples primarily from the Isua Greenstone Belt, contributed by Stephen Mojzsis via Kurt Konhauser, and supplement this dataset with additional data from samples from the Nuvvuagittuq and Nulliak localities (samples also

courtesy of Kurt Konhauser), in order to see what information, if any, can be gleaned about surface conditions, specifically weathering and continental emergence, ca. 3.7 to 3.8 Ga.

5.2 Methods

Sample of the Isua BIF were prepared at IUEM using a water-saw to cut off obviously weathered pieces of each sample before further processing. Samples of the Nuvvuagittuq and Nulliak Iron Formations were also considered for this study and were received from other laboratories in a powdered form. In the case of the Nuvvuagittuq samples, the powders are from the same sample set prepared by Mloszewska et al. (2012) at the University of Alberta; Nulliak samples were prepared under identical conditions.

For the Isua BIF samples, hand-cut slabs were crushed in a tungsten-carbide piston. The fragments where then taken and powdered in an agate ring mill, after which the chamber was cleaned twice, first by a physical washing with water and ethanol, then by a second cleansing of the chamber with pure silica for ten minutes. The vessel was then washed and rinsed a second time with water, soap, and ethanol. This process was repeated for each Isua sample and repeated for each of the 11 Isua samples we received. For the Isua samples, The most prohibitive aspect of the Nuvvuagittuq and Nulliak samples was that we received ~1 g of material per sample, thus we were severely limited in the number of analysis we could perform on these materials, therefore, we focused on determining εHf values for all samples, as well as their total Lu and Hf concentrations by isotope dilution, to allow for the correction from modern day values to those at ~3.8 Ga (see Chapter 2, Methods). Accordingly, while Sm/Nd and $^{143/144}$Nd ratios were determined for Isua samples using HR-ICP-MS (unspiked) and TIMS after column purification (see Chapter 2, Methods), these were not determined for Nuvvuagittuq and Nulliak samples due to limited sample material.

5.3 Results and Discussion

During the early stages of this study, the initial chemistry performed, and the εHf results obtained for the Isua BIF, were among the first analyses that were made, specifically due to their ancient heritage, and the prospect that they represented the oldest intact sedimentary chemical sequences known to date. Due to the fact that they were the first set of samples we processed through the traditional two column digestions outlined described by Blichert-Toft et al. (1997) not initially adapted for use on banded iron samples, we were not entirely sure of the outcome. From our experience with this first set of iron-rich samples we determined that the geochemical separation of Hf from other REE elements worked well based on the techniques described.

Our initial analysis of the Isua samples revealed extreme initial values for $^{176}Hf/^{177}Hf$; these values were so extreme that we considered the initial analyses potentially inaccurate, possibly due a failure to measure ^{173}Yb in the first analytical sessions and thus an inability to accurately correct for potential ^{176}Lu interferences using $^{173/176}Yb$. Also, for these first analyses, the concentrations of the Lu and Hf were initially determined by HR-ICP-MS analysis without isotope dilution, and were thus considered error prone, especially in light of the low concentrations of these elements in the samples (0.044 - 0.08 ppm Lu and 0.0020 – 0.0540 ppm Hf; Table 5.1).

Isua Iron Formation Preliminary Neptune Results										
Sample ID	Sample Name	Hf Concentration (ppb)	± 5%	Lu Concentration (ppb)	± 5%	Modern 176Lu/177Hf	± 5%	Modern 176Hf/177Hf	± 2σ	εHf at 3.8 Ga
G1	M30	0.0540	0.06	0.044	0.05	0.11570	0.00579	0.28759	0.000007	-46.44
G2	M33	0.0453	0.05	0.06	0.06	0.17335	0.00867	0.29319	0.000013	1.94
G3	GR/98/IM/18	0.0103	0.01	0.12	0.12	1.59922	0.07996	0.39006	0.000061	-282.24
G4	IM/Fe/7t	0.0031	0.00	0.05	0.05	2.27200	0.11360	0.37391	0.000051	-2622.22
G5	IM9	0.0141	0.01	0.11	0.12	1.10780	0.05539	0.35242	0.000033	-336.00
G6	IM22	0.0111	0.01	0.08	0.09	1.07076	0.05354	0.35227	0.000021	-244.25
G7	IM31	0.0020	0.00	0.09	0.09	6.25510	0.31276	0.57555	0.000060	-5875.32
G8	GR/97/IM/Fe/4	0.0079	0.01	0.05	0.06	0.96524	0.04826	0.35859	0.000027	257.85
G9	GR/97/IM/7 top	0.0063	0.01	0.08	0.08	1.79190	0.08960	0.31147	0.000049	-3590.32
G10	GR/98/IM/Fe/1	0.0041	0.00	0.08	0.08	2.79498	0.13975	0.39577	0.000043	-3213.89
G11	GR/98/IM/Fe/6	0.0027	0.00	0.08	0.09	4.27052	0.21353	0.38656	0.000033	-7411.40

Table 5.1: Initial values of εHf initially obtained and corrections interpolated for the Isua iron formation, lacking ^{173}Yb data due to a misalignment in the Neptune collection cups in the first analytical session, resulting in uncertain corrections for ^{176}Lu decay over 3.8 Ga.

After a second analysis (Table 5.2), this time using Hf and Lu spikes incorporated into the initial digestions, the values determined for samples from all three formations still represented some of the most extreme ^{176}Hf/^{177}Hf values ever recorded for chemical sedimentary precipitates.

Sample ID	Sample Name	Hf Concentration (ppb)	± 2σ	Lu Concentration (ppb)	± 2σ	Modern ^{176}Lu/^{177}Hf	± 2σ	Modern ^{176}Hf/^{177}Hf	± 2σ	εHf at 3.8 Ga	± 2σ
G1	M30	70.84	0.0029	47.26	0.03	0.09	0.00005	0.28738	0.000004	8.40	0.01
G2	M33	52.73	0.0029	51.40	0.13	0.14	0.00032	0.29316	0.000008	102.16	0.56
G3	GR/98/IM/18	11.47	0.0012	153.39	0.26	1.86	0.00301	0.35775	0.000019	-2123.79	7.24
G4	IM/Fe/7t	8.96	0.0061	99.35	0.43	1.54	0.00558	0.36597	0.000051	-993.53	12.81
G5	IM9	13.98	0.0010	90.79	0.02	0.90	0.00017	0.34360	0.000018	-114.32	0.20
G6	IM22	13.95	0.0007	94.42	0.08	0.94	0.00071	0.34120	0.000015	-300.66	1.32
G7	IM31	5.09	0.0008	116.80	0.25	3.20	0.00646	0.55381	0.000051	1369.43	15.12
G8	GR/97/IM/Fe/4	11.18	0.0010	61.63	0.09	0.77	0.00101	0.34929	0.000023	448.08	1.85
G9	GR/97/IM/7 top	7.55	0.0018	87.68	0.11	1.62	0.00168	0.34840	0.000035	-1813.71	3.18
G10	GR/98/IM/Fe/1	6.77	0.0042	94.48	0.03	1.94	0.00067	0.40693	0.000023	-581.69	0.92
G11	GR/98/IM/Fe/6	11.16	0.0005	87.07	0.03	1.09	0.00028	0.36398	0.000027	136.28	0.21

Sample ID	Sample Name	Hf Concentration (ppb)	± 2σ	Lu Concentration (ppb)	± 2σ	Modern ^{176}Lu/^{177}Hf	± 2σ	Modern ^{176}Hf/^{177}Hf	± 2σ	εHf at 3.8 Ga	± 2σ
Q1	090710-2	24.70	0.0019	188.99	0.47	1.07	0.00259	0.34867	0.00	-355.95	3.62462
Q2	090710-4	34.11	0.0008	141.10	0.26	0.58	0.00104	0.35594	0.00	1186.93	1.37354
Q3	090710-12	164.34	0.0058	26.64	0.12	0.02	0.00010	0.29198	0.00	357.07	0.05470
N1	PI-1	155.81	0.0075	39.12	0.01	0.03	0.00000	0.28281	0.00	-2.55	0.24688
N3	DL-82-26B	553.79	0.0128	115.76	0.03	0.03	0.00001	0.28207	0.00	-13.58	0.08968

Table 5.2: Initial values of εHf obtained for Eoarchean iron formations, analyzed a second time using Lu-Hf isotope dilution.

Values of $\varepsilon Hf_{(i)}$ range from –2123 to + 1369 in the Isua and Nuvvuagittuq formations, while the two samples analyzed from the Nulliak formation were much more moderate, providing εHf values between -13.6 and -2.6. At face value, the extreme nature of these results strongly suggest that ancient REE mobilization may have occurred, and that the fidelity of signals in ancient sedimentary deposits that have been subjected to such intense metamorphism should be carefully scrutinized.

To reach such extreme values, two likely scenarios present themselves: (1) the initial Lu/Hf ratios were highly variable, and represent everything from CHUR values to those approaching modern Lu/Hf values for the ocean; or (2) migration of Lu occurred post deposition, depleting some samples in Lu, and increasing Lu content in others. Our current assumption is that lutetium and hafnium mobilization is minimal during low-grade metamorphism, which appears to be true for both chemical sedimentary deposits and primary igneous deposits, as well as diagenetically altered chemical sediments; these assumptions may still hold true. However, it may not remain true for moderate to hi-grade (amphibolite facies and beyond) metamorphism where chemical sedimentary deposits are concerned.

In an attempt to determine the cause of the extreme values observed in these samples the Sm-Nd systematics (Table 5.3) were evaluated, the results of which may provide an explanation for the extreme εHf values observed (Table 5.2).

Sample ID	Sample Locality Isua BIF 3.8 Ga	Nd Concentration (ppm)	± 5%	Sm Concentration (ppm)	± 5%	Modern $^{147}Sm/^{144}Nd$	± 5%	Modern $^{143}Nd/^{144}Nd$	± 2σ	εNd at 3.8 Ga	± 2σ	Modern $^{143}Nd/^{144}Nd$
G1	Greenland	0.898	0.04	0.246	0.01	0.172354	0.00841	0.51183	0.00003	-3.95	0.33	0.51183
G2	Greenland	0.824	0.04	0.199	0.01	0.152445	0.00744	0.51119	0.00001	-6.65	3.23	0.51119
G3	Greenland	2.366	0.12	0.552	0.03	0.147062	0.00718	0.51123	0.00001	-3.23	0.13	0.51123
G4	Greenland	0.799	0.04	0.207	0.01	0.163139	0.00796	N/D	N/D	N/D	N/D	N/D
G5	Greenland	2.206	0.11	0.562	0.03	0.160452	0.00783	0.51113	0.00001	-11.80	8.11	0.51113
G6	Greenland	1.990	0.10	0.483	0.02	0.152950	0.00747	0.51126	0.00001	-5.48	1.94	0.51126
G7	Greenland	0.913	0.05	0.270	0.01	0.186221	0.00909	0.51160	0.00001	-15.23	10.96	0.51160
G8	Greenland	0.859	0.04	0.220	0.01	0.161404	0.00788	0.51161	0.00001	-2.75	0.99	0.51161
G9	Greenland	0.862	0.04	0.238	0.01	0.174092	0.00850	N/D	N/D	N/D	N/D	N/D
G10	Greenland	1.246	0.06	0.323	0.02	0.163208	0.00797	0.51166	0.00001	-2.70	1.05	0.51166
G11	Greenland	1.623	0.08	0.330	0.02	0.127921	0.00624	0.51162	0.00001	13.94	16.80	0.51162

Table 5.3: Initial values of εNd obtained for the Isua Banded Iron Formation.

The Sm-Nd data collected for Isua samples provide critical insight into the potential causes of both the clearly reset primary εNd data, as well the as the εHf values obtained. The εNd data was plotted as an errorchron which clearly shows that the values are most likely linked to metamorphic over-printing that occurred in the Isua region circa ~3.64 Ga ago (Figure 5.3). This was a period of intense granitoid intrusion and metamorphism, thus providing the prerequisite conditions for the transformation of primary sedimentary signals, and the migration of elements from initial sediments and minerals into new metamorphic minerals and mineral phases (Nutman et al. 2002).

Due to the apparent resetting of initial Nd, Sm, Hf, and Lu values a selective major element and minor element compositional analysis was performed on these samples (Table 5.4 and 5.5), and the εHf values obtained for the Isua samples were examined in light of these results in order to investigate potential correlations between elemental composition and εHf values (Figures 5.4-5.6). A full geochemical analysis of all samples was not performed as the samples from all three localities indicated extreme resetting of εHf values.

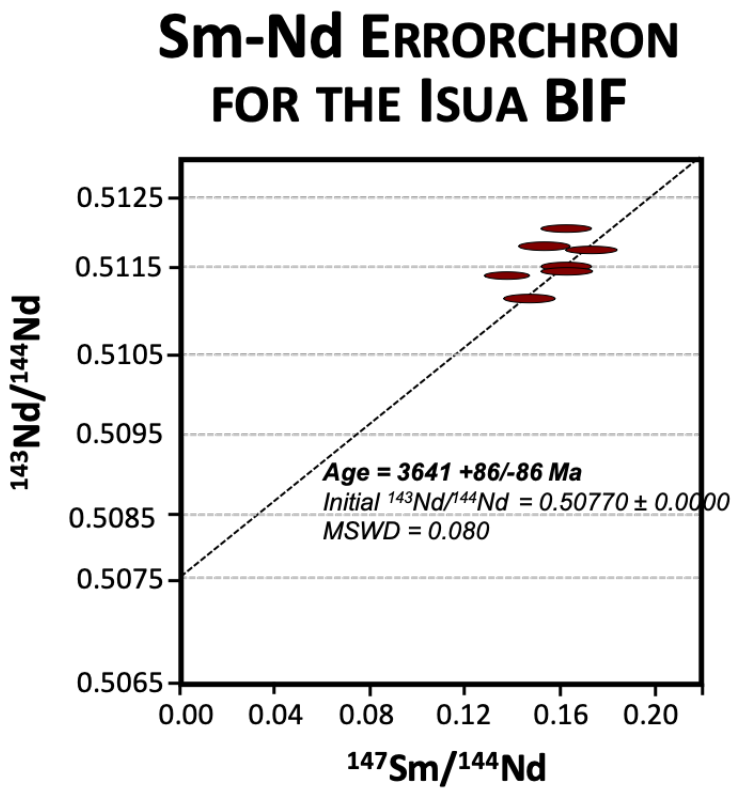

Figure 5.3 The Sm-Nd errorchron constructed from our Isua BIF data showing a clear signature of resetting and suggesting that the resetting took place ~ 3.64 Ga ago during known metamorphic events that occurred in the Isua region at that time (Nutman et al. 2002).

Isua Iron Formation											
Major Elements (Wt%)											
Sample Name	Sample ID	SiO_2	TiO_2	Al_2O_3	Fe_2O_3	MnO	MgO	CaO	Na_2O	K_2O	P_2O_5
M30	G1	47.79	0.03	0.41	48.32	0.07	2.09	1.78	0.05	0.02	0.11
M33	G2	45.44	0.02	0.47	48.83	0.09	2.34	3.44	0.07	0.04	0.11
GR/98/IM/18	G3	41.56	0.02	0.08	55.23	0.13	2.56	1.66	0.01	0.01	0.13
IM/Fe/7t	G4	42.93	0.01	0.02	51.72	0.07	1.81	2.88	N/D	0.02	0.12
IM9	G5	45.54	0.02	0.10	53.09	0.15	2.29	1.31	0.00	0.01	0.14
IM22	G6	56.18	0.02	0.05	43.32	0.12	1.81	1.15	N/D	0.01	0.12
IM31	G7	41.29	0.02	0.10	57.31	0.11	3.02	0.15	N/D	0.01	0.15
GR/97/IM/Fe/4	G8	49.06	0.02	0.04	50.42	0.03	1.64	1.33	N/D	0.01	0.12
GR/97/IM/7Top	G9	34.50	0.01	0.01	58.64	0.06	1.55	2.70	N/D	0.02	0.10
GR/98/IM/Fe/1	G10	58.14	0.01	0.02	42.39	0.02	0.40	0.46	0.02	0.01	0.08
GR/98/IM/Fe/6	G11	43.26	0.02	0.05	54.71	0.05	1.36	1.22	N/D	0.04	0.11

Table 5.4 Major element composition of the Isua Banded Iron Formation.

Isua Iron Formation											
Trace Elements (ppm)											
Sample Name	Sample ID	Sr	Ba	Sc	V	Cr	Co	Ni	Y	Zr	Nb
M30	G1	N/D	N/D	0.52	6.60	14.39	5.46	42.60	5.19	5.89	1.93
M33	G2	0.32	N/D	0.31	5.69	11.80	4.84	42.17	5.48	5.77	0.73
GR/98/IM/18	G3	N/D	N/D	0.25	5.62	3.70	3.65	35.23	12.77	4.24	1.18
IM/Fe/7t	G4	25.04	0.76	0.29	3.75	5.42	2.48	19.03	10.74	4.27	1.43
IM9	G5	N/D	N/D	0.57	4.72	5.25	2.72	28.55	12.09	4.18	1.59
IM22	G6	N/D	N/D	0.38	4.20	5.80	3.50	24.85	11.17	4.12	0.14
IM31	G7	N/D	N/D	0.23	3.48	2.78	8.35	67.19	7.96	3.69	0.52
GR/97/IM/Fe/4	G8	N/D	N/D	0.29	4.42	7.70	3.17	22.15	6.94	4.39	1.21
GR/97/IM/7Top	G9	22.97	0.60	0.07	3.61	3.56	3.23	17.46	8.66	4.35	1.30
GR/98/IM/Fe/1	G10	3.29	9.11	N/D	3.18	3.36	2.79	17.02	9.22	4.65	1.20
GR/98/IM/Fe/6	G11	5.59	6.36	0.18	3.50	2.94	3.55	19.55	9.29	4.32	0.57

Table 5.5 Select trace element compositions of the Isua Banded Iron Formation.

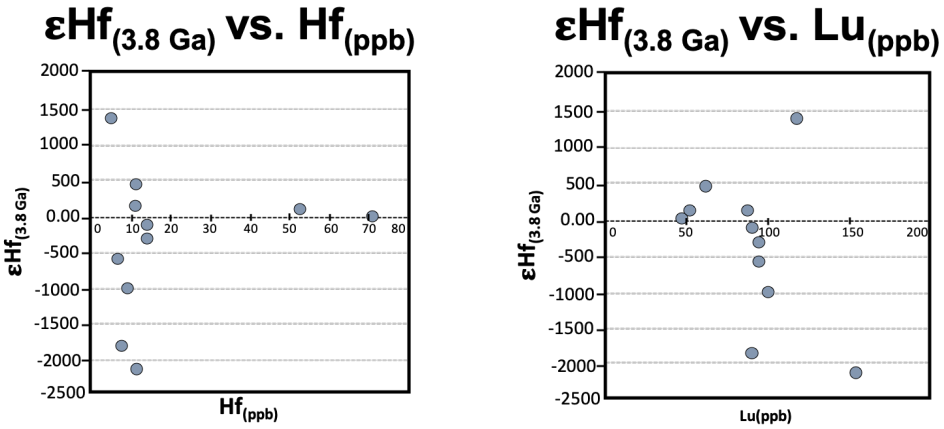

Figure 5.4: $\varepsilon Hf_{(i)}$ values verses total concentrations of Hf and Lu. In the case of Hf concentrations (Left panel) Hf concentrations are generally extremely low, and correlate with improbable $\varepsilon Hf_{(i)}$ values, and while higher concentrations of Hf values become more reasonable , they still represent implausible $\varepsilon Hf_{(i)}$ values. When $\varepsilon Hf_{(i)}$ values are compared to total Lu concentrations the data does not show a discernable correlation.

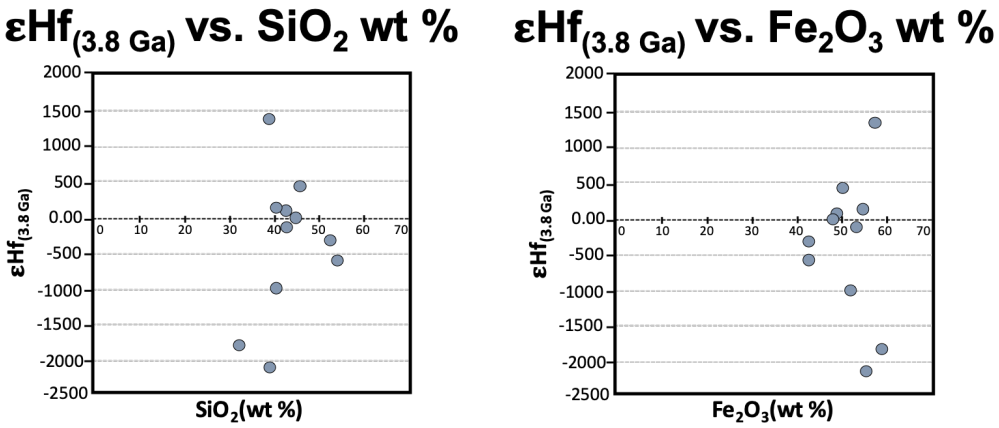

Figure 5.5: $\varepsilon Hf_{(i)}$ values vs. wt.% silica and iron. No correlation in $\varepsilon Hf_{(i)}$ values is observed with either Si or Fe oxides in the Isua samples.

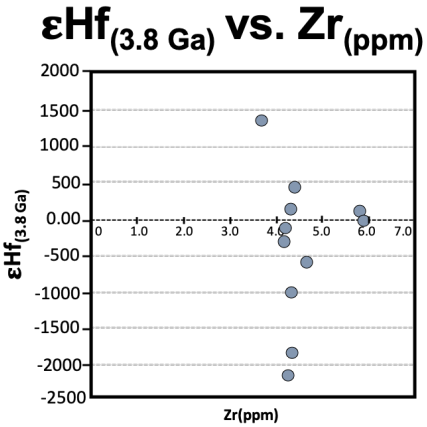

Figure 5.6: $\varepsilon Hf_{(i)}$ values vs. Zr concentrations (ppm), which exhibits virtually the same pattern as the $\varepsilon Hf_{(i)}$ values vs. Hf concentrations as seen in Figure 2, suggesting that increased Zr is correlated to less extreme values of $\varepsilon Hf_{(i)}$.

The extreme $\varepsilon Hf_{(i)}$ values for the Isua Formation, especially in combination with the obviously resent $\varepsilon Nd_{(i)}$ values, clearly indicates that both the Isua and Nuvvuagittuq samples have experienced secondary isotopic alteration since their initial deposition as flocculent iron-sediments ~3.8 Ga ago. Despite evaluating three different geographical sites (Isua, Nuvvuagittuq, and Nulliak), virtually all measured $\varepsilon Hf_{(i)}$ values, specifically the negative

values, are improbable, or even impossible, at 3.8 Ga. Given the extremely negative values exhibited in both the Isua and Nuvvuagittuq metasediments (down to $\varepsilon Hf_{(i)}$ -2123 and $\varepsilon Hf_{(i)}$ -355, respectively), such values exceed the possible $\varepsilon Hf_{(i)}$ value of ~ -12.5 as calculated for the continental crust by the estimates of Taylor & McLennan (1985), and Wedepohl (1995), by several orders of magnitude, where the lowest possible $\varepsilon Hf_{(i)}$ value at 3.8 Ga for crustal material is approximately $\boldsymbol{\varepsilon}Hf_{(i)}$ -12.5, given an initial Lu concentration of 0.0113 ppm. A reasonable interpretation of these results involves some degree of metamorphic resetting, the type, and timeframe of which, is discussed below.

Initial observations of the $\varepsilon Hf_{(i)}$ values for the Isua deposit show no correlation between the $\varepsilon Hf_{(i)}$ values and those of any other element, save that of Zr concentrations. $\varepsilon Hf_{(i)}$ values compared to either Hf or Lu are essentially scatter plots where minor changes in Lu or Hf total concentration is inexplicably tied to extreme differences in the age corrected $\varepsilon Hf_{(i)}$ value (Figure 5.2). Additional scrutiny of the $\varepsilon Hf_{(i)}$ value compared to the total SiO_2 wt% or the Fe_2O_3 wt% was also negative for any correlation between the $\varepsilon Hf_{(i)}$ value recorded and the corollary SiO_2 or Fe_2O_3 wt% (Figure 5.3). The only observably correlation is that between the $\varepsilon Hf_{(i)}$ value and the total amount of Zr (Figure 5.4), where it appears that higher concentrations of Zr are related to lower values of $\varepsilon Hf_{(i)}$, however in this instance the difference between the two sets of values varies by only 30% from a concentration of 3.7 – 6 ppm, suggesting that other factors besides the concentration of Zr are responsible for the extreme $\varepsilon Hf_{(i)}$ values observed.

Though sampling and analysis of Eoarchean sites in addition to Isua (i.e. Nuvvuagittuq and Nulliak) were limited, due to the similarity in data, and more specifically the observation of aberrant $\varepsilon Hf_{(i)}$ values, we consider that the three sites all produced results that are

uncharacteristically extreme both in the maximum and minimum values determined for $\varepsilon Hf_{(i)}$. However, unlike previous studies, our results suggest that the inferred sedimentary packages of these ancient crustal remnants behaved differently from the surrounding igneous units, and that during subsequent tectonic processes that followed the deposition the these sedimentary units, each responded in a fundamentally different way than the igneous units surrounding them, resulting in the obvious difference between the igneous units and their metasedimentary counterparts that are observable at this day.

Considering the modern isotopic compositions for εHf in the BIF are aberrant compared to the surrounding formations, we may still be able to reconstruct possible evolutionary paths of the samples to attempt to determine the reason and timing of this discrepancy. When regressed from their modern Lu/Hf values back to those at 3.8 Ga, most samples still lie far from the bulk silicate Earth line (and even below that line, which is not possible on Earth). There was therefore necessarily a shift in the parent/daughter ratios at some point, perhaps several consecutive events. If we assume that Lu/Hf ratios were homogeneous during BIF deposition, the most probable event causing this fractionation is metamorphism (especially considering that we know that these formations have experienced severe metamorphic events at some point since their deposition), however we cannot pinpoint exactly when. We can however conclude that the event occurred sometime prior to 2.0 Ga, and most likely early on during granitic emplacements, and the earlier this disturbance occurred the more extreme the Lu/Hf fractionation would appear in modern samples (Figure 5.7).

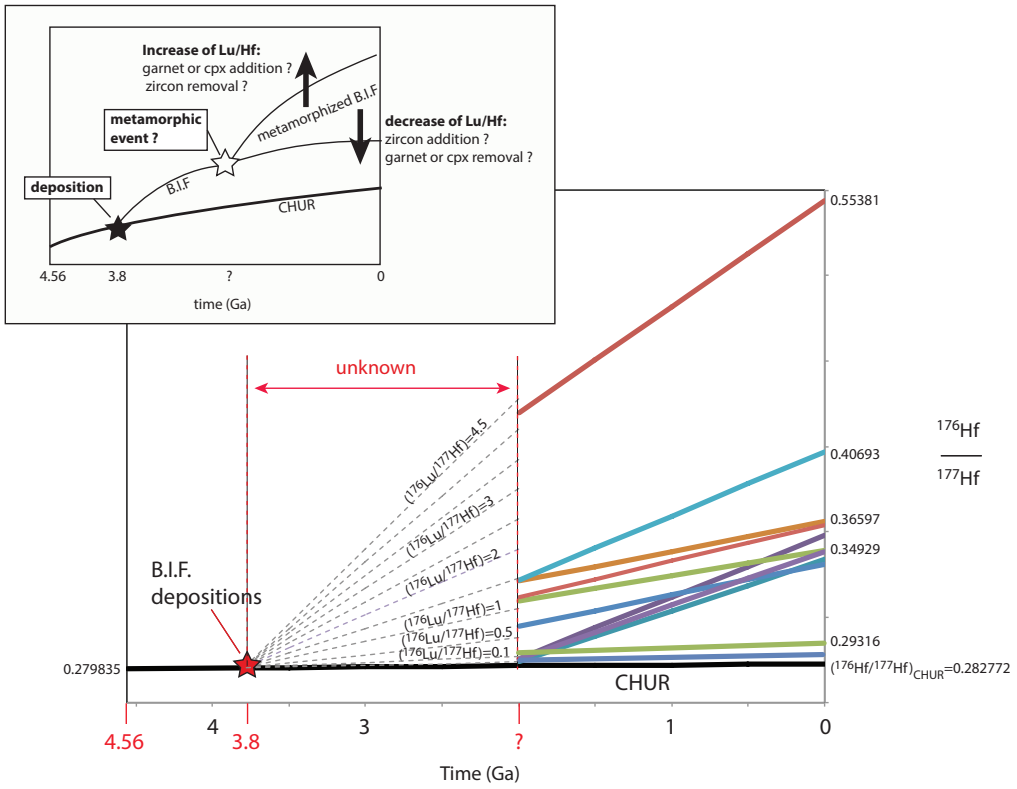

Figure 5.7: Evolution of $^{176}Hf/^{177}Hf$ ratios based on differing initial compositions of $^{176}Lu/^{177}Hf$, illustrating the different trajectories of $^{176}Hf/^{177}Hf$ based on the timing and extent of metamorphic alteration for our BIF samples.

Specifically, our data indicates that during metamorphism of primary chemical sediments, high-field strength elements that are typically considered to be immobile, in our case Sm-Nd and Lu-Hf, can become partially remobilized and incorporated into newly forming mineral phases such as garnets and clinopyroxenes in the case of both Lu and Sm, increasing the $^{176}Hf/^{177}Hf$ ratio. Alternatively, the loss of these minerals and the addition of zircon would lower this ratio. If such a process occurred during the final consolidation of cratonic crust in these three ancient cratons, it could explain the $\varepsilon Hf_{(i)}$ values observed in all three BIF sites.

During the transition from ambient temperatures to amphibolite and gneissic metamorphic grades, elements such as Lu and Sm might have been liberated from their original host phases and mobilized to nearby regions where they ultimately form minerals such as garnets. If this occurred early enough, it would confer extreme $\varepsilon Hf_{(i)}$ values such as those determined for the Isua, Nulliak and Nuvvuagittuq deposits. The calculations in Figure 5.7 show that relatively moderate shifts in Lu/Hf could easily explain the values we observe today within the BIFs.

The migration of Lu from the proto-BIF sediments would have left depletions of Lu in some localities and produced an excess of Lu in others via the formation of garnets. Once metamorphic grades reached their maximum and Lu and Sm were locked in by the formation of new mineral phases, the source regions for the REE elements depleted in Lu and Sm would exhibit exceptionally positive $\varepsilon Hf_{(i)}$ values, as those rock samples would have been under-corrected given their depleted Lu concentrations, while regions that gained Lu via the growth of garnets, or Hf via the growth of zircons, would now exhibit exceptionally negative $\varepsilon Hf_{(i)}$ values, as they are being overcorrected by the loss of Lu or increase in Hf.

Though the results of this preliminary study do not seem immediately encouraging, there are still possible avenues to explore that may allow for additional information to be gleaned from the $\varepsilon Hf_{(i)}$ values of Eoarchean metasediments. Specifically, we would suggest that new samples should be acquired from regions where the geological context is known exceptionally well, and that sampling should not just be surficial, but performed by drill core, and that samples be obtained as far as possible from metamorphosed beds containing garnets or zircons.

Secondly, large amounts of initial material should be collected, as significant amounts of each sample may need to be discarded in the preparatory processes, specifically with the removal of weathered edges and the need to contrast bulk rock signals with those of individual layers of chert vs. iron-oxide. Third, our results suggest that an initial phase of mineral separation to isolate both zircon crystals and garnets should be attempted before powdering of each sample in order to remove as many metamorphic contaminants as possible.

Finally, due to the extremely low concentrations of both Lu and Hf in these samples, it is recommended to dissolve 1-2 g of sample material, then spilt them into several (2 minimum, 4 preferably) rounds of column chemistry. Though tedious, this will help ensure that all iron is removed, and that any aliquot sent for Lu-Hf or Sm-Nd analysis is as pure as possible.

5.4 Conclusions

Investigation of the Isua, Nuvvuagittuq, and Nulliak Iron formations has revealed both a success and a dilemma in the investigation of Earth's early sedimentary and weathering processes. This particular study has shown the shortcomings in our current approach to determining the precise timing and extent of early terrestrial subaerial weathering, but it has also provided us with a series of specific set of geochemical lessons and techniques that we can follow to improve results in the future, as well as where and how new samples could be acquired. Although our results cannot definitively answer the question of continental emergence at or prior to 3.8 Ga, they leave open the possibility that with proper controls, and careful analysis, these questions may yet be answered in the near future, and that the geochemical record of terrestrial habitats might be pushed back to coincide with the Earth's earliest sedimentary deposits.

5.5 References

Blichert-Toft, J., Chauvel, C., & Albarède, F. Separation of Hf and Lu for high-precision isotopic analysis of rock samples by magnetic sector-multiple collector ICP-MS. *Contributions to Mineral Petrology*, 127, (1997).

Dymek, R.F., and Klein, C., (1988). Chemistry, Petrology, and Origin of Banded Iron-Formation Lithologies from the 3800 Ma Isua Supracrustal Belt, West Greenland. *Precambrian Research,* 39, 247-302.

Komiya, T., Yamamoto, S., Aoki, S., Sawaki, Y., Ishikawa, A., Tashiro, T., Keiko, K., Shimojo, M., Aoki, K., Collerson, K.D., (2015). Geology of the Eoarchean, >3.95 Ga, Nulliak supracrustal rocks in the Saglek Block, northern Labrador, Canada: The oldest geologic evidence for plate tectonics. *Tectonophysics,* 662, 40-66.

Mloszewska, A.M., Pecoits, E., Cates, N.L., Mojzsis, S.J., O'Neil, J., Robbins, L.J., Konhauser, K.O., (2012). The composition of Earth's oldest iron formations: The Nuvvuagittus Supracrustal Belt (Québec, Canada). *Earth and Planetary Science Letters*, 317-318, 331-342

Moorbath, S., O'Nions, R.K., and Pankhurst, R.J., (1973). Early Archean Age for the Isua Iron Formation, West Greenland. *Nature*, 245, 138-139.

Nutman, A.P., McGregor, V.R., Shiraishi, K., Friend, C.R.L., Bennett, V.C., Kinny, P.D., (2002). ≥3850 Ma BIF and mafic inclusion in the early Archean Itsaq Gneiss Complex around Akilia, southern West Greenland? The difficulties of precise dating of zircon-free protoliths in migmatites. *Precambrian Research, (117), 185-224.*

Nutman, A.P., Friend, C.R.L., Horie, K., Hidaka, H., (2007). Chapter 3.3 The Itsaq Gneiss complex of South West Greenland and the Construction of Eoarchaean Crust at Convergent Plate Boundaries. *Developments in Precambrian Geology*, 15, 187-218.

O'Neil, J., Francis, D., Carlson, R.W., (2011). Implications of the Nuvvuagittuq Greenstone Belt for the Formation of Earth's Early Crust. *Journal of Petrology*, 52, 985-1009.

Polat, A. and Frei, R. (2005) The origin of early Archean banded iron formations and continental crust, Isua, southern West Greenland. *Precambrian Research*, 138, 151-175.

Rollinson, H., (2003). Metamorphic history suggested by garnet-growth chronologies in the Isua Greenstone Belt, West Greenland. *Precambrian Research,* 126, 181-196.

Taylor, S.R. and McLennan, S.M. (1985). The Continental Crust; Its composition and evolution; an examination of the geochemical record preserved in sedimentary rocks. Blackwell, Oxford. *312*.

Wedepohl, K.H. (1995). The composition of the continental crust. *Geochemica et Cosmochemica Acta,* 59, 1217-1232.

Conclusions and Future Perspectives

The evolution of the Earth, the mantle, crust, and the emerged surfaces of our planet, are of critical importance to our understanding of the why, when, and how diverse environmental and biological evolutionary events shaped our planet's history. Indeed, our planet would be utterly unrecognizable to us 700 million, 2.5 billion, 3.5 billion years ago, or virtually any time in between. Over the almost unfathomable timescale of millions and even billions of years, our world has transformed remarkably in many ways, including the composition of its crust, its oceans, its atmosphere, the flora and fauna present, the configuration of the continents, and importantly the very existence or absence of said continents that were emerged above sea level. This thesis has sought to shed light on the last of these major transformations, and to try to refine our knowledge of exactly when continental land masses were exposed above sea level, and how those masses interacted with the Earth system during extreme climatic events such as the Sturtian Snowball Earth.

Emerged land would have begun an entirely new process on our planet, that of chemical and physical weathering, the direct and indirect results of which are still largely unknown. One obvious consequence would be the generation of a new source of nutrients to the oceans, and indeed two entirely new types of habitats, subaerial and freshwater habitats, for life to colonize. The ultimate result cannot be ignored; virtually the entire biomass humans are familiar with, including ourselves, relies on the presence and renewal of exposed land, and in fact, we are just now beginning to realize how deeply threatened our civilization is if coastal areas begin to submerge back into the sea due to global warming.

Our chosen proxy was the εNd-εHf isotope composition of chemically precipitated banded iron formations (BIF) from several different deposits that vary in location, age, and depositional setting. Each of these deposits also represent an important time in Earth history

where the presence or absence of emerged continents, or their influence on the Earth system, is highly uncertain. At the time the Braemar BIF was deposited, during the Sturtian Snowball Earth event, we are quite certain that nearly the same amount of exposed continental material existed as does today. This was however highly uncertain during the deposition of the Moodies BIF in the Paleoarchean, when models suggest that no continents were emerged, but sedimentary deposits suggest otherwise. Finally, in the case of the Eoarchean Isua, Nulliak, and Nuvvuagittuq BIF, there is near-total uncertainty about the emergence of any landmass above sealevel. Each of these deposits has provided important insight into the story of continental emergence and its interaction with the surrounding environment, or alternatively, revealed limitations in the Nd-Hf isotope approach, and not always in expected ways, as summarized below.

Isua, Nuvvuagittuq, and Nulliak: Revealing limitations in the Nd-Hf isotope approach

Unfortunately, due to what appears to be early metamorphic alteration of these samples, specifically the mobilization of Lu, the majority of results obtained in this thesis produced implausible εHf signatures (values ranging from lower then -2000 to greater than +1300). Indeed, in the case of Isua, the Sm-Nd errorchron also yields a significantly younger age than the accepted age of the deposit, suggesting that bulk analysis of such BIF samples is not a viable means of determining continental emergence using Nd-Hf isotope systematics for such such highly deposits. Encouragingly, not all samples produced unreasonable results, and those that are unreasonable can be artificially corrected by small adjustments to the amount of ^{176}Lu calculated for a sample; for example, the most positive εHf values converge to CHUR by the addition of 88% more Lu, while the most negative values converge to CHUR with the subtraction of 40% of the currently measured Lu. Given the extremely low concentrations of ^{176}Lu calculated for these samples (0.69 to 4.8 ppb), the required additions or subtractions, in

terms of absolute abundances, is in fact minimal. Further scrutiny is warranted as it is unclear if these results are the result of error in bulk analysis, or the inclusion of garnets or zircons, in the determination of the true Lu/Hf value of the samples examined.

The Moodies Group BIF: An early isotope record of continental emergence

The Moodies Group BIF is an extremely atypical BIF, interpreted to be coastline-proximal, as indicated by the inclusion of detrital sediment layers and lenses (silts and occasional sands) into the BIF. That said, there are no observed ripples, and these BIF appear to have been deposited below wavebase, similar to Superior- or Algoma-type BIF that were deposited during highstands and sedimentary hiatuses, or in close association with volcanics in highly hydrothermally-influenced settings, respectively. εNd results for the Moodies BIF ranged between + 2.6 and -1.7, while εHf results for this BIF ranged from -14.7 to +36.6, demonstrating a clear decoupling of the εNd- εHf system, and showing two distinct trends of decreasing εHf with increasing Zr concentrations, and increasing εHf with increasing SiO_2 content. This secondary trend suggests that cherts may also record the εHf value of seawater. In addition, the PO_4 content shows a strong correlation with Fe_2O_3, with the highest values of P corresponding to the highest percentage of Fe, and trailing off towards more detritally contaminated, and more silica rich endmembers. These data suggest that Fe was a likely shuttle for P out of the oceans. Finally, the occurrence of 9 samples with positive εHf values on or above the seawater array provides clear evidence of continental weathering at 3.2 Ga, excluding the existence of a waterword at this time as some models have suggested, and indicating that terrestrial and fresh water environments have existed for most of Earth's history.

The Braemar Iron Formation: isotopic insight into Snowball Earth weathering

The Braemar BIF represents another atypical BIF for which the depositional environment is interpreted to have been along the edges of a passive-to-active margin coastline during a waning period of the Sturtian Snowball Earth glaciation. It is observed in the field as being lenticular and podiform, with high degrees of detrital sedimentary contamination, including occasional occurrences of an iron-matrix diamictite. The least contaminated samples selected for this study (those with Fe_2O_3 from 55-77 wt%) record εNd from -5.4 to -0.2, with εHf -8.1 to + 19.1, showing a clearing decoupling of Nd and Hf isotope compositions that are a hallmark indicator of subaerial continental weathering. In fact, the εHf values show remarkable similarities to glacial lakes, glacial rivers, and non-glacial river waters sampled from modern day Greenland, suggesting that even during the Sturtian Snowball Earth Event, at times there were areas not only where glacial retreat or subglacial melt was occurring, but also areas where glaciers had completely receded and non-glacially-fed rivers flowed.

Perspectives for future application of Nd-Hf isotope systematics to chemical sediments

The results of this study have been encouraging and suggest that further investigation of chemical sedimentary rocks such as Banded Iron Formations, and possibly cherts, may yet yield further insight into the history of continental emergence on our planet. They also suggest a number of potential avenues to improve results, and interpretations, specifically; (i) careful sampling of materials to avoid weathering rinds, and an awareness that whole rock data may not be representative of individual iron-rich or chert rich-layers in a BIF, and that separation of Lu- or Hf-rich phases such as garnet or zircon may be required before analysis; (ii) careful understanding of BIF depositional environments is crucial as BIF that form in settings where detrital sedimentary influx are significant should be interpreted differently than tradition BIF that form far from terrestrial influxes; (iii) due to the extremely high percentage of iron

compared to rare earth elements of interest in these samples, individual samples may need to be subdivided and run through several different columns and then recombined to avoid iron saturation on the resins and loss of REE; (iv) the decoupled positive εHf signal of continental weathering requires the decay of ^{176}Lu into ^{176}Hf, a process with an extremely long half-life, thus, Lu-bearing minerals that are weathered, but have not aged significantly since their formation, will produce a weak or conceivably undetectable signal despite active weathering; (v) the type of rock being weathered will affect the εHf signal observed, especially if more then one type is weathered, and one of the components contains substantial amounts of zircon; (vi) and finally, the length of time, or intensity of weathering a rock experiences, will affect the observable εHf signal, as vulnerable mineral phases most likely to contain Lu will weather first, and quickly, compared to phases containing Hf.

Ultimately this study has tripled the amount of εHf data we have for Precambrian chemical sedimentary rocks and has extended available evidence for continental emergence back an additional 500 Ma. That said, much more data will need to be collected from additional sample locations, formations of different ages, and potentially different sample types (i.e. cherts), before a coherent picture emerges regarding the timing and extent of continental emergence on our planet in deep geological time.

UNIVERSITE SCIENCES BRETAGNE DE LA MER LOIRE ET DU LITTORAL

UBO Université de Bretagne Occidentale

IMT Atlantique
Bretagne-Pays de la Loire
École Mines-Télécom

Titre : Émergence et Altération des Continents sur la Terre primitive : Contraintes à partir des isotopes Hf-Nd dans les Formations de Fer Précambriennes

Mots clés : Émergence continentale, Hafnium, Lutétium, isotopes, formations de fer en bandes

Résumé : L'émergence de la croûte continentale au-dessus du niveau de la mer au début du Précambrien aurait créé les premiers habitats terrestres et amorcé l'altération des continents par l'atmosphère. Cependant, l'histoire de l'émergence continentale demeure largement inconnue. Les sédiments chimiques Précambriens, en particulier les Formations de Fer Rubanés (BIF), semblent avoir échantillonné la composition isotopique en Hf-Nd de l'eau de mer ancienne et pourraient ainsi préserver un enregistrement historique de l'émergence de masses continentales par fractionnement Lu/Hf, induit par une altération différentielle subaérienne. Toutefois, les données appariées sur les isotopes Hf-Nd ne sont disponibles que pour quelques localités à ce jour, et indiquent une masse continentale émergée appréciable d'environ 2,7 Ga. Notre travail vise à confirmer et à étendre ce record du Néoprotérozoïque au Paléo- et Eo-Archéen en utilisant des échantillons de BIF âgés de 750 Ma de la formation Bramer en Australie centrale, de 3,2 Ga du Moodies Group, Afrique du Sud, et de 3,8 Ga de Isua, Groenland, ainsi que plusieurs échantillons du Nuvvuagittuq, Québec, et Nulliak, Labrador, Canada.
Les échantillons Eo-archéen semblent avoir été significativement affectés par le métamorphisme de type amphibolite, mais les échantillons du Moodies Group conservent des signaux environnementaux primaires, ayant connu des types métamorphiques significativement inférieurs. Les échantillons du Moodies Group montrent que les valeurs d'!Hf sont comparables à celles observées dans les dépôts sédimentaires marins détritiques et chimiques modernes, correspondant à une masse terrestre émergée à cette époque. Les résultats de la formation de Braemar sont également interprétés comme conservant les signatures primaires d'!Hf, et ont des valeurs remarquablement similaires à celles récemment rapportées pour les eaux fluviales glaciaires et non glaciaires au Groenland, témoignant d'une altération subaérienne concomitante avec les dépôts Sturtian de BIF durant les premiers stades de la déglaciation.
Ensemble, mes résultats suggèrent que les masses émergées ont été une caractéristique de la Terre depuis au moins le Paléoarchéen, malgré les modèles théoriques qui suggèrent que l'émergence s'est produite quelque temps après 3 Ga, et que l'interprétation des données !Hf et !Nd des BIF n'est pas aussi simple que suggérée précédemment. Une large gamme de valeurs d'!Hf peut être enregistrée dans les BIF, qui peut représenter non seulement un enregistrement des compositions de Hf et Lu de l'eau de mer au moment du dépôt, mais peut aussi enregistrer la présence de contaminants détritiques et/ou l'historique des altérations post-dépôt.

Title: Tracking Continental Emergence and Weathering on the Early Earth: Seawater Hf-Nd Isotope Constraints from Precambrian Iron Formations.

Keywords : Continental Emergence, Hafnium, Lutetium, Isotopes, Banded Iron Formations.

Abstract : The emergence of continental crust abov sea level in the early Precambrian would have created the first terrestrial habitats, and initiated atmosphere driven weathering of the continents, yet the history of continental emergence is largely unknown. Precambrian chemical sediments, specifically Banded Iron Formation (BIF) previously studied, appear to have sampled the Hf-Nd isotope composition of ancient seawater, and may preserve a historical record of the emergence of continental landmasses via Lu/Hf fractionation induced by subaerial differential weathering. However, paired Hf-Nd isotope data are available for only a few localities to date, but indicate appreciable emerged continental landmass ca. 2.7 Ga. Our work seeks to confirm and extend this record from the Neoproterozoic into the Paleo- and Eo-Archean using samples of 750 Ma BIF from the Braemar formation in central Australia, 3.2 Ga BIF from the Moodies Group, S. Africa, and 3.8 Ga BIF from Isua, Greenland, as well as several samples from Nuvvuagittuq Quebec, and Nulliak Labrador, Canada.
Eoarchean samples appear to have been altered by amphibolite-grade metamorphism, however Moodies Group samples appear primary, having experienced significantly lower metamorphic grades. Moodies appear to retain their primary seawater signatures with !Hf values comparable to those observed in modern oceanic detrital and chemical deposits. Results from the Braemar formation are also interpreted as retaining primary !Hf values signatures and are found to have strikingly similar values to those recently reported for glacial and non-glacial river waters in Greenland. Together our studies suggest that emerged land masses have been a feature of the Earth since at least the Paleoarchean, despite theoretical models that suggest emergence occurred sometime after 3 Ga ago, and that the interpretation of !Hf and !Nd data from BIF is not as straightforward as previously suggested. A large range of !Hf values can be recorded in BIF that may represent not only a record of ocean water Hf and Lu compositions at the time of deposition, but also BIF can record the presence of detrital contaminants, and/or the existence of post-depositional alteration.